UNIVERSITÀ DEGLI STUDI DI TRIESTE

UNIVERSITÀ DEGLI STUDI DI TRIESTE

XXXV Ciclo del Dottorato di Ricerca in Fisica

Ultrafast photoelectron spectroscopy of quantum materials with a novel 10.8 eV photon source

Settore scientifico-disciplinare: FIS03/FISICA DELLA MATERIA

Dottorando:
Denny Puntel

Coordinatore:
Prof. Francesco Longo

Supervisore di tesi:
Dott. Federico Cilento

Co-supervisori di tesi:
Prof. Fulvio Parmigiani
Dott. Giancarlo Panaccione

ANNO ACCADEMICO 2021–2022

"[. . .] toutes les fois qu'un être humain accomplit un effort d'attention
avec le seul désir de devenir plus apte à saisir la vérité,
il acquiert cette aptitude plus grande, même si son effort n'a produit aucun fruit visible."

Simone Weil, "Réflexions sur le bon usage des études scolaires
en vue de l'amour de Dieu"

"A che potensa l'è arrivata la scienza! Be', vediamo, vediamo!"

Maestro Spinelloccio il dottore,
in "Gianni Schicchi", Puccini-Forzano

Abstract

This thesis presents the study of three quantum materials conducted by means of a novel photon source for Time- and Angle-Resolved Photoelectron Spectroscopy (TR-ARPES) developed at the T-ReX laboratory at FERMI (Elettra, Trieste). This source provides pulses at a photon energy of 10.8 eV up to the MHz repetition rate, while offering picosecond time resolution and few tens of meV energy resolution. The results from the three science cases studied highlight how the unique capabilities of this setup are beneficial to tackle open scientific questions in different areas of modern condensed matter physics. The three systems pertain to different material classes, namely a topological insulator, a kagome metal and a high-temperature superconductor.

The topological insulator Bi_2Se_3 is studied to address the effect of spin-orbit coupling in shaping the 2D dispersion of the topological surface state. *Ab-initio* calculations of the photoemission with variable spin-orbit coupling strength at the surface are compared with equilibrium and nonequilibrium measurements performed at 10.8 eV. The dispersion is reproduced by spin orbit coupling strength reduced to 70-85 % of its full atomic value.

The study of the kagome metal CoSn focusses on the dynamics of its two flat bands, that arise due to the lattice-induced localization of electrons and the resulting enhancement of the effect of correlations. The flat bands are investigated at large momentum values, where they can be distinguished from each other. The effect of photoexcitation is an ultrafast shift and broadening, both of the order of the meV, suggesting a small electron delocalization induced by the pump pulse.

The study on the copper-based superconductor Bi2212 comprises the use of three sources. The results of TR-ARPES performed with the 10.8 eV source show that this setup allows accessing the antinodal region, located at large k values. However, in the present configuration the setup is not optimized for providing detailed insight on the nonequilibrium response of these states. Improving the time resolution of the setup will allow access also to the antinodal dynamics.

The investigation of the O $2p$ states, performed by means of an HHG source, shows that an infrared pump pulse redistributes charges in the valence band involving also the oxygen states. Time-resolved X-ray photoelectron spectroscopy measurements performed at a free-electron laser facility clarify that the main response to the charge redistribution induced by infrared photoexcitation occurs in the copper-oxygen planes, where the fundamental interactions of cuprates take place.

Contents

Chapter 1

Introduction

The term "quantum materials" designates all those material systems where a rationalization of the macroscopic physical properties needs to take into explicit account the intrinsic quantum nature of the underlying microscopic phenomenology [1]. Also for systems not labelled by this name, the most appropriate microscopic description employs quantum mechanics. What quantum materials in particular realize is the manifestation on larger spatial, energy or time scales of the consequences of interactions occurring at a quantum level. Interactions like the Coulomb repulsion between electrons, the spin-orbit coupling, or the Cooper pairing in superconductors occur at the eV or sub-eV energy scale, but are capable of dramatically influence the macroscopic properties of quantum materials like the electrical conductivity or the specific heat [2]. The class of quantum materials thus includes, among the others, superconductors [3], unconventional magnets [4], topological insulators [5] or transition-metal dichalcogenides [6].

As these examples already suggest, the electronic properties of quantum materials are of great potential for technological applications [7]. On the other side, unconventional macroscopic properties often emerge from microscopic phenomena that are nontrivial in their own respect. For this reason, the fundamental research on quantum materials can find its roots in the quest for more efficient and versatile capabilities for technological applications, but stands also on its own as a playground where the most intriguing phenomena in modern condensed matter physics can be investigated.

The collection of experimental evidences on the physics of quantum materials relies on spectroscopic techniques that allow direct or indirect access to the energy, spatial or temporal scales of the order of the phenomena under scrutiny. Therefore, the research on quantum materials is also fostered by technical advancements that allow experiments with increasingly high resolution. Moreover, controlling and manipulating the microscopic degrees of freedom of quantum materials can offer new pathways to shape their properties as suited for the applications [8].

The electronic properties of ordered materials are largely encoded in the band structure, *i.e.* the dispersion relation of energy *versus* crystal momentum of the valence band electrons. Mapping the electronic dispersion of a system offers a wealth of information on the interactions that govern the electronic behavior of the system. Moreover, in complex systems electrons generally interact with each other, giving rise to changes in the band

structure due to correlations. Electrons also interact with the collective excitations of the system [9], or feel the effect of spin-orbit coupling [10], to name but a few examples.

The most direct experimental access to the band structure is provided by the Angle-Resolved Photoelectron Spectroscopy (ARPES). The technique is based on the photoelectric effect, for which an electron can be emitted from a material by a photon of sufficient energy to overcome its work function. The energy and momentum conservation laws for the photoemission process allow retrieving, from the energy and the emission angle of the photoelectron, the energy and crystal momentum possessed by the electron inside the system. The same conservation laws also prescribe a limit in the energy and momentum ranges that can be probed at a given photon energy. Since it encodes information on the band structure of the system, the ARPES measurement can also unveil the interactions felt by the electron before photoemission [11]. The capability of ARPES of providing valuable insights in the electronic properties of material systems is subject of numerous reviews [3, 12, 13].

Under equilibrium conditions, however, the different interactions governing the microscopic behavior of a system occur simultaneously and their observable effects may superimpose, hence making it challenging to tell them apart by inspection of the equilibrium band structure alone. An approach to disentangle different coexisting interactions is to exploit the typically different time scales that characterize them. The principle is called *pump-probe* and ranges across various techniques, including optical spectroscopy [14], STM [15], photoemission [16]. The basic idea is to impart an impulsive excitation to the system, and to measure it at several time intervals before and after the excitation. In this way, the complete dynamics of the excitation of the system out of its equilibrium conditions and recovery towards equilibrium can be tracked.

Accessing the nonequilibrium dynamics of the band structure is possible by implementing the optical pump-probe scheme in the photoemission experiment, hence realizing the Time- and Angle-resolved Photoelectron Spectroscopy (TR-ARPES) [16]. This implies exciting the system with a first pulse (the pump), and performing the photoemission measurement with a second pulse (the probe) to track the evolution of the dispersion. The wealth of information on the physics of quantum materials offered by TR-ARPES is vast. The direct optical transitions triggered by the pump from below to above the Fermi level allow to probe parts of the unoccupied band structure [17]. More fundamentally, the effect of the pump can be that of inducing a transition to an equilibrium or a purely non-thermal state, which can be inspected by monitoring the corresponding features in the band structure (gaps, kinks,...) [18]. Finally, the relaxation time of the excited electronic population and of the possible pump-induced modifications allows disentangling the interactions that drive them on the basis of their timescales [19].

The possibility of employing a pump-probe scheme in photoemission critically depends on the use of pulsed light for the pump and the probe. Basically, a longer duration of the pulses implies a worse time resolution for the experiment. The pulse duration has thus to be optimized, but in order to address the band structure features with high resolution, also the energy and momentum resolution along with the count rate should be preserved. Moreover, a larger photon energy is in general preferable since it allows accessing larger portions of the band structure.

The development of TR-ARPES was made possible by the advent of ultrafast lasers.

At present date, the major limitations to the capabilities of TR-ARPES setups come from the photon source. Laser-based setups rely on tabletop sources providing short pulses (10-300 fs) typically in the infrared region, narrow bandwidths (tens of meV) and repetition rates in excess of the kHz and in some cases of the MHz [20]. The photon energy is subsequently increased by various techniques of higher harmonic generation. The main focus of the developments in the TR-ARPES field is nowadays devoted to finding generation techniques that allow optimizing the trade off between photon energy, energy-time resolution, and photoemission count rates. As a result, different generation schemes offer operation in complementary intervals of the values of these parameters [21].

Harmonics generation in nonlinear crystals is the simplest and most common among these schemes, largely due to the fact that the photon energy ($<$7 eV) allows simple design of the setups. The low photon energy is also the major limitation of these setups, that on the other hand offer excellent time and energy resolutions (down to the Fourier limit) [20]. These limitations have fostered the search for different generation schemes. Harmonics generation by nonlinear processes, or ionization and recombination in rare gases (HHG) require superior laser source capabilities and were developed only recently, but allow to reach photon energies up to 11 eV in the former case, and up to the soft X-rays in the latter, although applicability to TR-ARPES setups is limited to 70 eV [22]. A particular case is represented by the use of free-electron laser emission, that additionally allows the extension to the time domain of typically core-level synchrotron techniques like x-ray photoelectron spectroscopy and diffraction [23].

This thesis is devoted to the exploration of the advancements in TR-ARPES made possible by a novel photon source at 10.8 eV probe photon energy obtained by a cascade ninth harmonic generation in nonlinear crystals and in Xe gas. The capabilities of the setup are first proven with the direct characterization of the source. The setup is capable of operating at the MHz repetition rate and delivering $\sim$ 1.3 ps and $\sim$ 80 meV time and energy resolutions, with a high number of counts in space-charge free régime, suitable for reaching good statistics in equilibrium and time-resolved measurements. The remaining part of the thesis presents three scientific cases that show how the combination of the source parameters offered by the novel 10.8 eV source allows tackling open scientific questions in quantum materials of present interest. These are the topological insulator Bi_2Se_3, where the spin-orbit coupling is the dominant interaction, the kagome metal CoSn, where the effect of correlations is enhanced by electron localization, and the copper-based high-temperature superconductor Bi2212, where electronic correlations and charge-transfer interactions play a dominant role. On this last system, we performed further complementary measurements with an HHG and an FEL source.

The following chapter introduces the basic concepts of ARPES and TR-ARPES, with particular care towards the aspects that limit the capabilities of the setups for the time-resolved technique. In particular, it is the photon energy of the source that defines the extent of binding energy and parallel momentum that can be probed by photoemission. Moreover, the bandwidth and time duration directly influence the energy and time resolution of the setup. Finally, the repetition rate and the number of photons per pulse are what defines the capability of the source to provide good signal-to-noise statistics.

Chapter 3 reviews the generation schemes presently available for TR-ARPES. These

are divided on the basis of the physical principle they rely on for the generation of pulses of suitable photon energy ($> 5\,\mathrm{eV}$). Frequency doubling and summing in nonlinear crystals are briefly discussed. Most importantly, this chapter presents the working principles and the experimental realization of the 10.8 eV setup based on the generation of third harmonic in Xe gas. A detailed discussion of the most relevant parts of the setup is also provided, along with the characterization of the energy and time resolution of the setup. The main limitations of the scheme and possible improvements are also discussed. The chapter also presents the basics of HHG and FEL-based photoemission, along with a description of the setups used for the measurements of this thesis.

Chapter 4 discusses the application of the 10.8 eV source for the investigation of the topological insulator Bi_2Se_3. Our study focusses on the role of the spin-orbit coupling in shaping the dispersion of the topological surface state of this system, which deviates from the expected linear dispersion. Our measurements are used to validate a series of *ab-initio* calculations performed varying the SOC strength down to 50 % of its full atomic value for the first 20 layers of the crystal. The comparison of the calculations with the measured dispersion below and above the Fermi level indicates that the effective strength of the SOC is reduced at the surface to 70-85 % of its full value.

Chapter 5 presents the results obtained in the investigation of the kagome metal CoSn. In this case the photoexcitation is used to determine the response of flat bands that originate from a localization of electrons in real space due to geometrical confinement. The effect of the pump is to delocalize the electrons, an which we monitored by tracking the time-dependent dispersion of the flat bands. These undergo a shift in energy and a broadening, both of few meV, hence indicating that photoexcitation delocalizes a fraction of electrons but that the localization mechanism is robust against ultrafast optical excitation.

Chapter 6 comprises time-resolved photoemission measurements performed with three different photon sources on the cuprate superconductor Bi2212. The 10.8 eV photon energy was employed to study the dynamics in the valence band at large momentum values (antinodes). While the equilibrium measurements prove the capability of reaching the antinode, spurious effects hinder a detailed resolution of the dynamics. Charge transfer interactions, that are believed to be intertwined with lower energy scale phenomena like superconductivity, were instead studied by addressing the O $2p$ levelsstates in the valence band with an HHG source. A depopulation and small broadening were found, in agreement with literature. Finally, the free-electron laser FLASH was employed to add to this investigation the site sensitivity to distinguish the dynamics of different oxygen atoms in the unit cell. The largest changes are observed in the oxygen lying in the Cu-O plane, which is the one involved in the charge-transfer, hence confirming that this interaction plays a dominant role in shaping the nonequilibrium properties of cuprates.

Chapter 2

Time- and Angle-Resolved Photoelectron Spectroscopy

In this chapter the basic concepts of ARPES and TR-ARPES are introduced. The physical quantities that can be extracted from an angle-resolved photoemission experiment are discussed, along with the experimental means employed nowadays to perform such experiments. Particular attention is drawn to those aspects that turn out to be critical in the extension of the technique to the time domain. The information that can be retrieved with nonequilibrium photoemission is then discussed, along with the fundamental aspects that presently limit the application of this technique to relevant scientific cases. A detailed discussion of the light sources for TR-ARPES is instead subject of the next chapter.

2.1 Basic principles of ARPES

2.1.1 The photoemission process

Photoemission is a photon-in electron-out technique that relies on the photoelectric effect, *i.e.* the capability of photons of suitable energy to emit an electron from the bound states of a material into the vacuum [24, 25]. The kinetic energy of the photoemitted electron depends on the energy of the incident photon, following the relation dictated by the energy conservation:

$$E_{kin} = h\nu - E_B - \Phi. \tag{2.1}$$

Here $h\nu$ is the energy of the incoming photon, E_B is the binding energy of the electron in the initial state, and Φ the work function of the material, *i.e.* the difference between the Fermi level E_F of the system and the vacuum level. The process is schematized in Fig. 2.1(a) [26]. Since the kinetic energy is a positive quantity, the photon energy must thus be sufficient to overcome the binding energy of the electron and the work function of the material. The possibility to retrieve the binding energy of the electrons inside the sample by measuring their kinetic energy after photoemission is at the basis of the photoelectron spectroscopies [26]. The distribution of the number of photoelectrons as a function of energy hence provides direct information on the density of states (DOS) of

the material. However, the shape of the count rates *vs.* kinetic energy in the upper part of Fig. 2.1(a) is not identical to the DOS profile in the lower part due to the broadening induced by the experimental resolution.

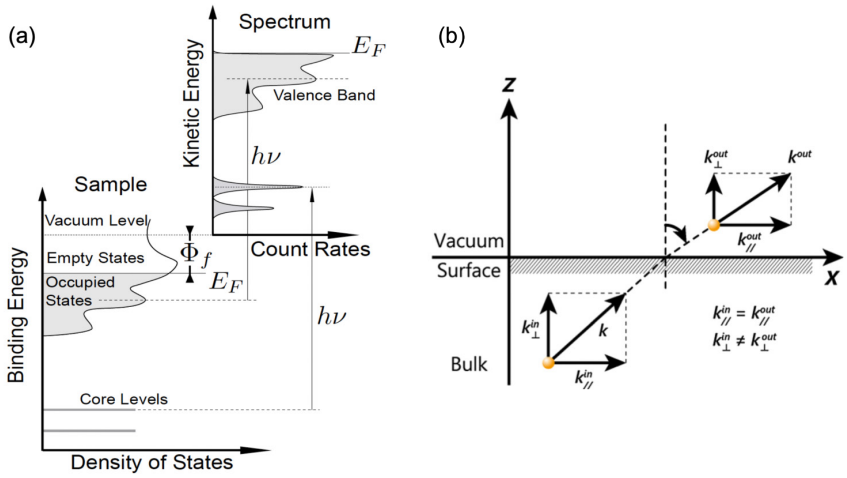

Figure 2.1: (a) Energy diagram of the photoemission process. The lower part shows the density of states inside the sample, which is translated by the photoemission process into the spectrum measured outside the sample. From [27], adapted after [26]. (b) Vectorial representation of the momentum conservation relations. Adapted from [28].

The conservation of momentum ($\mathbf{k}$) for the photoemission process must be considered separately for the parallel ($k_{\|}$) and perpendicular (k_z) components to the sample surface (Fig. 2.1(b)). This is due to the breaking of translational symmetry induced by the surface itself, which can be taken into account with a nearly free-electron model in the conservation relation for the perpendicular momentum as an additional term V_0 called *inner potential* [29]. For photon energies below ∼100 eV, which is the case of all the momentum-resolved measurements of this thesis, the momentum transferred from the photon to the electron is negligible. Being ϑ the polar angle between the perpendicular to the sample surface and the direction of the outgoing electron, as indicated in Fig. 2.1(c), the conservation law for the two momentum components reads:

$$\begin{cases} k_{\|} = \frac{1}{\hbar}\sqrt{2mE_{kin}} \cdot \sin(\vartheta) \\ k_z = \frac{1}{\hbar}\sqrt{2m(E_{kin} \cdot \cos^2(\vartheta) + V_0)}. \end{cases} \tag{2.2}$$

Since $E_{kin} = h\nu - E_B - \Phi$ (Eq. 2.1) is a positive quantity, these relations also set a limit for the values of momentum that can be probed at a given photon energy $h\nu$ and binding energy E_B.

The value of V_0 is challenging to obtain from calculations, and is most commonly deduced from the periodicity of the dispersion along k_z with E_{kin}. It is typically determined by continuously tuning the photon energy $h\nu$ on a suitably extended range [30]. This issue is absent for two-dimensional systems, and in general for surface states, since they lack dispersion along k_z.

Eq. 2.2 reveals that, upon measuring the angle ϑ at which the photoelectron with kinetic energy E_k is emitted, it is possible to deduce the crystal momentum of the electron itself. The angle-resolved photoelectron spectroscopy (ARPES) measurement hence allows a mapping of the E *vs.* k relation inside the crystal, which encodes information on the band structure of the system. It is understood that ARPES is a meaningful technique only for samples exhibiting a long-range order, where the periodicity of the potential allows describing the electrons in the valence band in terms of Bloch states [31].

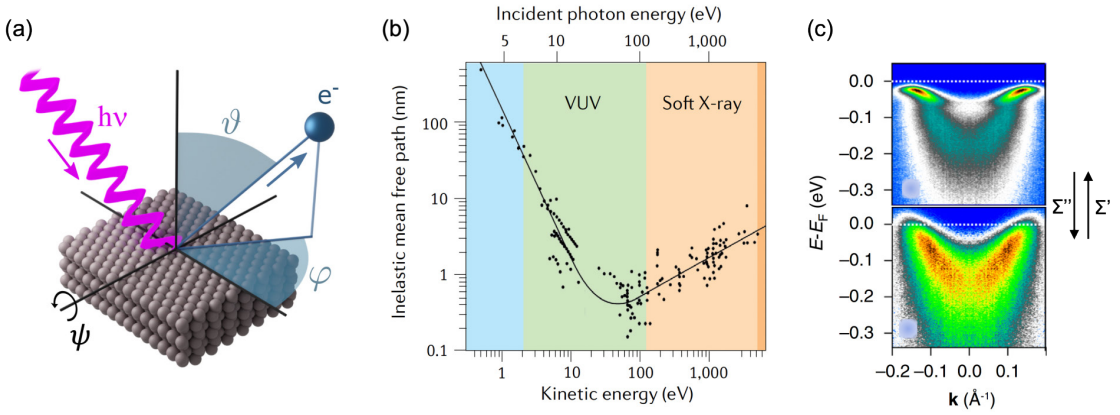

Figure 2.2: (a) Experimental geometry for an angle-resolved photoemission measurement, indicating the polar (ϑ), azimuth (φ) and tilt (ψ) angles [12]. (b) Universal curve of the inelastic mean free path as a function of the photoelectron kinetic energy (bottom axis) and incident photon energy (top axis) assuming $\Phi + E_B \simeq 4\,eV$ [13]. (c) Effect of the real and imaginary parts of the self energy. A larger imaginary part broadens the dispersion (from upper to lower panel), while a larger real part modifies the dispersion (from lower to upper panel), causing in this case a kink close to E_F. Adapted from [32].

An ARPES experiment consists in the detection of the number of electrons emitted in a range of E_{kin} and ϑ values, which can be mapped into binding energy and crystal momentum using the conservation relations 2.1 and 2.2. To elucidate the relation between $I(\mathbf{k}, E_B)$, commonly referred to as photoemission intensity, and the band structure that is being probed, we must inspect the physical and experimental effects that contribute to determine the photoemission intensity under the given conditions of sample band structure and incident light. The most common framework in which the photoemission process is interpreted is the semiclassical *three step* model [3]. Dividing the process into three independent steps is purely phenomenological, although it has proven often successful in reproducing the photoemission data [26]. A more rigorous treatment of the problem requires modeling the process as a single coherent transition [33], as for example done for the calculations reported in Ch. 4. The three-step model is however of simpler use to qualitatively describe the photoemission of an electron from a solid sample.

In the first step, the incoming photon drives a direct transition of an electron inside the sample. It is in this step that the information about the band structure and the excitation probabilities is encoded. The electron traverses the sample thickness up to the surface (second step). In the third step, the photoelectron traverses the surface and is emitted

into the vacuum: it is in this step that the translational symmetry breaking disrupts the conservation of the perpendicular momentum component.

It is worth emphasizing that the energy and momentum conservation relations of Eq. 2.1 and 2.2 are valid only if the photoelectron does not undergo any scattering event while traversing the sample thickness in the second step of the photoemission process. Such electrons are called *primary* electrons, in contrast to the secondary electrons that undergo scattering and contribute to the background of the measurement [34]. The average distance that an electron can traverse in a solid without undergoing scattering events is called *mean free path* and its dependence on the photoelectron kinetic energy typically follows the so called *universal curve* (Fig. 2.3(b)). The curve has a minimum at kinetic energies of few tens of eV that amounts to less than 10 Å. Since typical lattice parameters vary from few Å (∼3.6 Å for Cu) to several tens (∼31 Å for Bi2212), this means that the largest contribution to the photoemission intensity comes from electrons photoemitted from the first layers close to the surface. This renders ARPES a surface-sensitive technique. However at photoelectron kinetic energies of less than 10 eV the surface sensitivity is gradually lost in favor of a more pronounced bulk contribution to the primary electrons, which can be recovered on the higher side of photon energies only approaching the soft- or hard-X rays.

The photoemission intensity coming from the primary electrons comprises three terms [35]:

$$I(\mathbf{k}, E_B) = I_0(\mathbf{k}, E_B, h\nu,)A(\mathbf{k}, E_B)f(E_B, T). \tag{2.3}$$

This expression does not account for the contribution of secondary electrons to the detected photoemission intensity. The secondary electrons contribute by adding a background to the raw data that is subtracted in the post processing or ARPES data. The next paragraphs discuss the relevance of the three terms of Eq. 2.4 to the aim of the interpretation of the ARPES measurement.

Matrix element effects: $\mathbf{I_0(k, E_B, h\nu,)}$ The term accounts for the probability of the transition from the initial Bloch state $|\varphi^i_{\mathbf{k}}\rangle$ to the final free-electron state $\left|\varphi^f_{\mathbf{k}}\right\rangle$ due to the interaction with the photon. Within a semiclassical picture, where the electric field of the incident radiation is treated as a classical field with vector potential $\mathbf{A}$, the interaction hamiltonian between the field and the electron of momentum $\mathbf{p}$ is treated as a perturbation of the form $H_{int} \propto \mathbf{p} \cdot \mathbf{A}$. The Fermi golden rule [3] prescribes the probability of this transition to be proportional to the matrix element

$$|M^{i,f}_{\mathbf{k}}| = \left\langle \varphi^f_{\mathbf{k}} \middle| \mathbf{p} \cdot \mathbf{A} \middle| \varphi^i_{\mathbf{k}} \right\rangle. \tag{2.4}$$

The matrix element thus modulates the photoemission intensity depending on the relative orientation between the polarization of the incident light and the electron momentum. Therefore, suitable combinations of photon energy and polarization can selectively enhance or suppress photoemission from specific electronic states, and can be used to reconstruct the orbital character of the bands or to enhance specific features in the band structure [32, 36].

This also tells that a photoemission measurements is not an absolute measurement of the system band structure, but that strong variations can appear upon varying the photon-energy. Matrix-element effects (as well as k_z dispersion) have to be taken into account when comparing photoemission measurements performed at different photon energies. The comparison with structure calculations is affected by the same issue, unless the full photoemission process is taken into account, and hence also the interaction of the electrons with the incident light (cf. Ch. 4.2).

Band structure: $\mathbf{A(E_B, k)}$ This term is known as *one-electron removal spectral function* and encodes the information on the band structure of the system. It stems from a description of the photoemission process in terms of the Green functions, which is the best suited formalism as it can account for the electronic correlations [11] and allows extending the treatment to the time-resolved case [37] (cf. Sec. 2.2). Since the terminology is ubiquitous in the field of correlated systems and therefore used in this thesis, we will briefly discuss it here.

For a noninteracting system of scattering-free particles, the spectral function A_0 takes the form of a Dirac-delta function centered at the energy and momentum values dictated by the dispersion relation $E(\mathbf{k})$ of the band structure:

$$A_0(\mathbf{k}, E) \propto \delta(E - E_B(\mathbf{k})). \tag{2.5}$$

The interaction among electrons, or with collective excitations of the system, modifies the dispersion relation in a way described in the Green function formalism by means of the complex *self energy* Σ. We refer to [38, 39] for a detailed description of the concept and the formalism of self energy. Here we only report the form of the spectral function A for an interacting system once the self-energy effects have been taken into account:

$$A(\mathbf{k}, E) \propto \frac{\Sigma''(\mathbf{k}, E)}{[E - E_B(\mathbf{k}) - \Sigma'(\mathbf{k}, E)]^2 + [\Sigma''(\mathbf{k}, E)]^2}, \tag{2.6}$$

where Σ' and Σ'' indicate the real and imaginary parts of the self energy.

The functional form of $A(\mathbf{k}, E)$ is that of a Lorentzian centered at $[E(\mathbf{k}) - \Sigma'(\mathbf{k})]$, with a broadening given by $\Sigma''(\mathbf{k}, E)$. The role of the real and imaginary parts of the self energy are exemplified in Fig. 2.3(c) [32]. Going from the upper panel to the lower one, the imaginary part of the self energy increases. Its effect is to broaden the electron distribution, and it accounts for the finite lifetime of the state. Going from the lower to the upper panel, instead, the real part increases, and the dispersion changes shape acquiring a kink close to E_F. The role of the real part of the self energy is thus to modify the bare-electron dispersion $E(\mathbf{k})$ by an amount Σ'. The renormalization of the electronic dispersion is the formal equivalent of the concept of *quasiparticle*, *i.e.* an electron dressed by the many-body interactions felt in the system, which thus behaves as an electron with modified (renormalized) dispersion and finite lifetime [40].

Band structure population: $\boldsymbol{f(E_B, T)}$ The Fermi-Dirac distribution accounts for the capability of equilibrium ARPES of probing only the occupied states. The finite temperature is a physical source of the Fermi edge broadening that adds up to the experimental

sources of broadening discussed in the following sections. It can be used to estimate the temperature of the electronic subsystem, provided that background and energy resolution effects are taken into account.

2.1.2 ARPES: experimental perspective

In this section we briefly discuss the key issues in the realization of a photoemission experiment. A comprehensive overview on the state-of-the-art equilibrium ARPES is outside the scope of this work, and we refer to the vast review literature on the subject [3, 12, 13]. Nonetheless, several aspects deserve attention as they define fundamental properties of the APRES experiment and are of key importance in discussing the extension of the technique to the time domain.

The photon source Several properties of the ARPES experiment directly depend on the characteristics of photon sources employed. Three parameters define the properties of a photon source with respect to the photoemission experiment: the photon energy, the spectral content and the photon flux.

The conservation relations of Eq. 2.1 and 2.2 indicate a physical limitation to the extent of binding energy and parallel momentum that can be probed for a given photon energy. The choice of the photon energy to employ has to deal with this constraint in the first place. As discussed above, the photon energy also selects the k_z at which the band structure is probed, and together with the polarization it modulates the photoemission intensity *via* the matrix elements effects. Photon energy tunability is therefore a useful knob to gain control on both aspects.

The photon source for ARPES must be monochromatic since all the photoelectrons measured at a given kinetic energy must be traced back to a single value of E_B, which is not possible if photons of different energy are involved. For this reason, the finite spectral content of the source contributes to the broadening of the measured spectra and thus to the total energy resolution of the measurement.

Good photon flux is required in the photoemission experiment in order to acquire significant statistics to enhance the signal-to-noise ratio within reasonable measurement times. Monochromatizing the radiation typically goes at the expenses of the photon flux and hence of the acquisition time.

At present date, the photon sources capable of offering reasonable compromises between these parameters are discharge lamps, synchrotron and free-electron lasers (FELs), and sources based on tabletop lasers. Discharge lamps are a good option for a laboratory-based setup or *in situ* characterization of samples, offering intrinsic small bandwidth ($<$1 meV) but fixed photon energy (tens of eV) and partial polarization control [41]. Synchrotron radiation offers key advantages for equilibrium APRES measurements [42]. Photon energies from few eV to several keV can be obtained, hence covering the whole Brillouin zone of material systems and giving access to the core levels. It also offers continuous tunability of photon energy and polarization, in addition to a large photon flux in a quasi-continuous wave régime. Photon flux is an important parameter since the narrow

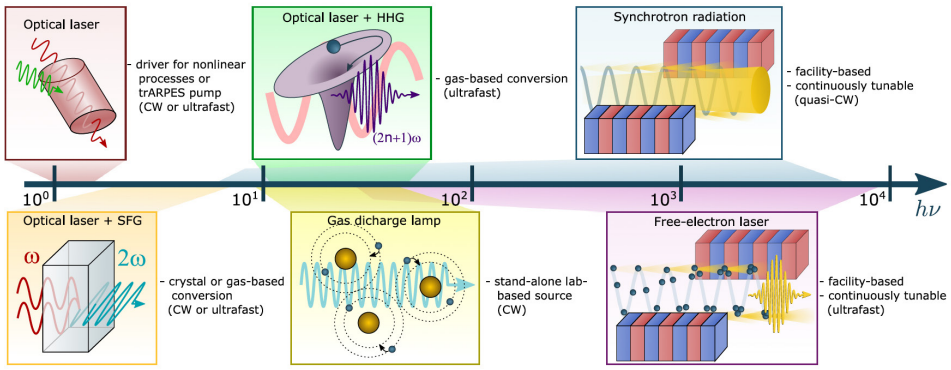

Figure 2.3: Light sources as a function of the photon energy range they typically cover [12]. The availability of the sources for time-resolved experiments is defined by the possibility to operate them in a pulsed mode (labeled here by ultrafast). Continuous wave (CW) sources as discharge lamps or synchrotron-radiation are used for static ARPES only.

spectral content is obtained by means of monochromators that filter out the radiation and diminish the photon flux at the sample.

Tunability and high photon energy are also common to FELs, that on the other hand have a limited repetition rate and a huge number of photons per pulse, which causes space-charge related issues (Sec. 2.1.2) [43]. FELs are considered for photoemission mainly in the time-resolved case. Laser-based systems offer the advantage of being laboratory-based sources, in contrast with large-scale facilities as synchrotrons and FELs. The majority of the laser-based setups rely on the generation of higher harmonics in crystals and gases [20, 44] and operate in the UV-VUV range, although recently soft X-rays can also be generated in suitable schemes [45]. For equilibrium ARPES, laser-based setups offer high flux at very low photon energies, where synchrotrons might have lower photon flux; at these energies, due to technical reasons related to the photoelectron detection, high energy and momentum resolutions can be reached. Laser-based photoemission is the most suited starting point to implement the time resolution thanks to the capability of laser pulses to reach very short pulse durations [13]. Since they pertain to the field of TR-ARPES, FELs and pulsed laser sources are discussed in more detail in the next chapter.

To stress the importance of the photon energy in defining the maximum k range available (Sec. 2.1.1), we show in Fig. 2.4 the momentum range visible at an angle of $\pm 30°$ for two selected values of photon energies. The lowest, 6.2 eV, is common in crystal-based setups for TR-ARPES (Sec. 3.1), and is compared with the 10.8 eV photon energy of the source we developed and employ in this work. Panel (a) shows the band structure of the kagome metal CoSn (Ch.5) along ΓK measured with 92 eV with a synchrotron source [46]. As visible, the 6.2 eV is capable of accessing only a small portion of the band structure around Γ, while the 10.8 eV captures the whole extension of the feature at $E - E_F \sim 0.3$ eV. Even more striking is the case of Bi2212, whose Fermi surface (intensity as a function of k_x and k_y close to E_F) is shown in panel (b). At 6.2 eV photon energy the bands can not be reached, and larger angles must be employed. At 10.8 eV, instead, a large part of the bands can already be reached, and larger angles can allow access the full Brillouin zone of

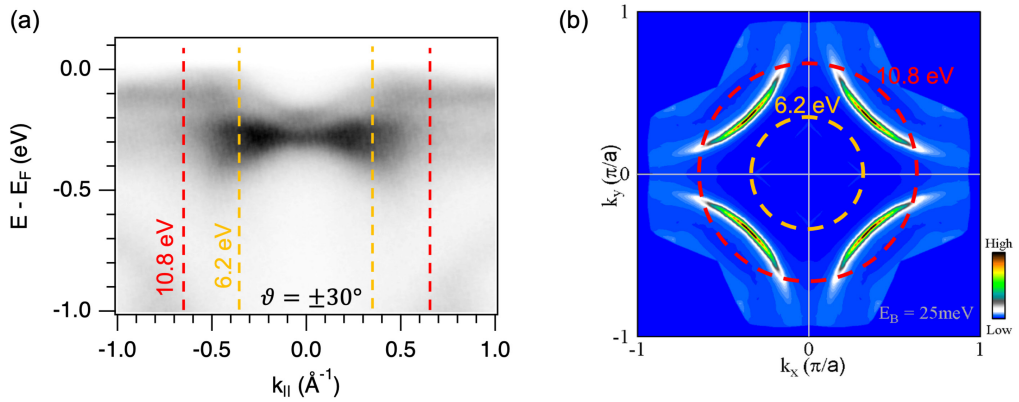

Figure 2.4: (a) Dispersion of CoSn measured with 92 eV photons along ΓK. Plot of data already published in [46]. The red line marks the momentum value reached with 10.8 eV photon energy and $\vartheta = \pm 30°$, while the yellow one is for 6.2 eV photon energy. (b) Photoemission intensity as a function of k_x and k_y of Bi2212 at $E - E_F = 25$ meV. The circles mark the momentum with the same angle and photon energies as those of panel (a) [47].

this system.

The spectrometer The photoemission experiment is based on the possibility to determine the kinetic energy and the two angles of emission (ϑ, φ) of the photoelectrons (Fig. 2.3(a)). The dispersion along at least one momentum direction can be acquired with modern electron spectrometers thanks to 2D detection schemes. Three kinds of such spectrometers are currently in use, namely the hemispherical analyzer, the time-of-flight analyzer and the momentum microscope [12].

A scheme of the hemispherical analyzer, extensively used in this work, is reported in Fig. 2.5(a) [48, 49]. The collected photoelectrons pass through a system of electrostatic lenses and are fed into the entrance slit aperture, which selects only a slice of the incoming photoelectron cloud. The hemispherical analyzer thus records the photoelectron distribution with momentum resolution only along the angular direction parallel to the slit, which we will call k_x, and for an extent defined by the length of the slit itself. The angular acceptance varies typically from 15° (low angular dispersion, LAD) to 30° (side angle mode, WAM), and contributes to the maximum momentum range detectable in the single measurement. Along the direction perpendicular to the slit (k_y), the photoelectron distribution is averaged out. This also means that a larger slit integrates over a larger k_y interval, at the expenses of the energy and momentum resolution of the measurement. The potential difference between the two electrodes of the hemispherical capacitor preserves the angular distribution along the direction of the slit (apart from a mirroring), and spatially disperses the electron trajectories along the perpendicular direction, to an extent that depends on their kinetic energy. The electrons impinge on a 2D multi-channel plate and are subsequently detected with a delay-line detector [50] or a CCD camera.

The result of the measurement is thus a distribution of intensity over the area of the detector, with one axis representing the angular distribution and the other the electron

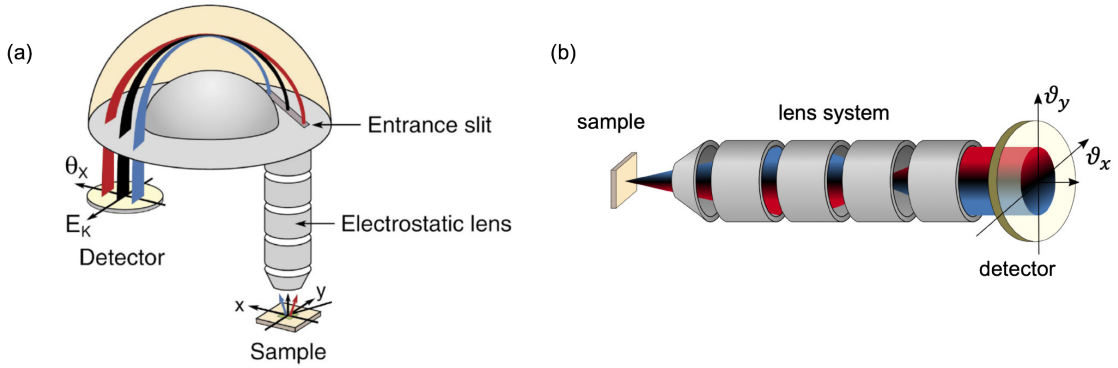

Figure 2.5: (a) Scheme of a hemispherical analyzer, with the colored lines indicating photoelectrons emitted at different ϑ angles [3]. (b) Scheme of a time-of-flight analyzer. Also in this case the color helps distinguishing electrons emitted at different angles. Adapted from [12].

kinetic energy. This can be converted into a two-dimensional map of photoemission intensity as a function of the binding energy and one momentum direction, and is a slice of the whole 3D (E_B, k_x, k_y) phase space available at given photon energy. Larger values of k_x can be probed up to the limit imposed by Eq. 2.1 by rotating the polar angle of the sample (ϑ in Fig. 2.3(a)). The dispersion along the k_y must be retrieved rotating either the tilt angle ψ or the azimuthal angle φ and acquiring a 2D map for each angle. Some hemispherical analyzers also include the capability of changing the vertical direction of acceptance through special deflectors in front of the lens system. In this way the dispersion along k_y can be mapped with the net advantage that the relative orientation between photon source, sample and analyzer remains fixed.

The time-of-flight detection scheme is schematized in Fig. 2.5(b). The measurement of the kinetic energy in this case is based on the time elapsed between the photoemission event and the revelation of the electron on the detector [51] [52]. Due to the speed of event detection and recording of the system, only pulsed sources of suitably low repetition rate ($\lesssim$1 MHz) are compatible with this detection system [53]. This scheme allows employing both the directions of the detector for the mapping of the 2D angular distribution of the photoelectrons, hence simultaneously acquiring the whole $I(E_B, k_x, k_y)$ distribution.

An important development starting from this scheme is the time-of-flight spectrometer based momentum microscope developed by Gerd Schönhense [54], which was used for the measurements shown in Ch. 6 of this thesis. It employs the lens system of a typical spectrometer for photoemission electron microscopy (PEEM), where the lens settings can be changed to project on the detector either the real space distribution of electrons (PEEM) or the reciprocal space distribution (ARPES). The strong electric field exerted on the sample by the first elements of the lens column allows collecting the full distribution of photoelectrons up to $\vartheta = 90°$, with huge advantage both on the momentum range accessible at given photon energy and on the total photoelectron count rate. The combination with the ToF scheme adds the kinetic energy resolution and allows performing the complete ARPES experiment. The PEEM mode additionally allows estimating the position

and size of the photon beam on the sample by looking at the real-space distribution of photoelectrons. However, the momentum microscope features a complex system of lenses to image the incoming angular distribution onto the detector, and optimal working conditions require fine optimization of a number of parameters. Moreover, the strong electric fields exerted at the sample surface requires that in the field of view of the microscope surfaces are extremely flat with little corrugation. On the other hand, the effective field of view can be suitably reduced, by means of filtering apertures in the lens column, to avoid sample edges and macroscopic surface discontinuities, or to push the technique towards a micro-APRES régime [55].

Space-charge effects Space-charge is a drawback effect in photoemission spectroscopy arising from the Coulomb interaction among photoelectrons [56]. The consequence is a distortion of the energy-momentum distribution of the photoelectrons. At a first approximation it shifts in energy and broadens the photoelectron spectrum, and is thus detrimental for the resolution of the experiment. Small spot sizes and pulsed sources are thus the conditions where space-charge effects are more severe, since the density of electrons in real space and thus the electron-electron interaction is larger. For moderate regimes of space-charge, the Coulomb interaction within the electron cloud can be modeled and the original distribution is retrieved [57]. However, for pulsed sources, decreasing the number of photons per pulse is the preferred strategy, and the possibility to achieve a good signal-to-noise ratio in the measurement critically depends on the repetition rate of the source (cf. corresponding paragraph in Sec.2.1.2).

Energy and momentum resolution The bandwidth of the photon source has typically the largest contribution in limiting the experimental resolution. This can be as good as 1 meV for synchrotron and discharge lamp sources, while FELs and pulsed lasers are subject to further constraints and are extensively discussed in Ch. 3. Since synchrotrons and FELs commonly rely on monochromators for the photon energy filtering, improving the energy resolution on the source side means reducing the effective flux of photoelectrons, with consequent scaling of the measurement time for equivalent signal-to-noise ratio. Another case in which the photon flux must be reduced in favor of the energy resolution is when the space-charge regime is approached, with the same drawbacks on the count rate.

Hemispherical analyzers, operated at the smallest values of entrance slit aperture, can achieve an energy resolution of $\sim$ 1 meV. Since these conditions require very small entrance slit aperture and hence limited photoelectron flux, hemispherical analyzers are most often operated with a resolution around 10 meV. The momentum microscope has proven capable of delivering a similar energy resolution, the main difficulty being the minimization of space-charge effects inside the lens column [53, 58].

The momentum resolution is usually determined by the angular resolution of the analyzer, that can go below 0.1°. Large spot sizes can also be a source of k broadening, since photoelectrons emitted at the same angle but from distant regions over the spot area are mapped into different real-space positions on the entrance slit. The possibility of reducing the field of view in momentum microscopes mitigates this effect. Moreover, propagating the uncertainty on the angle in Eq. 2.2, one obtains that

$$\Delta k \propto \sqrt{E_{kin}}\Delta\vartheta.$$

The momentum resolution is thus intrinsically worse at higher photon energies, since a larger k interval corresponds to the same angular interval.

A special case of space-charge induced broadening occurs in the detection schemes of the momentum microscopes, since at the focal planes inside the lens column (Fig. 2.5(b)) the electrons are constrained in a small volume. For this reason, the limit of photoelectrons per pulse to avoid space-charge with a momentum microscope is a factor 100 smaller than for a hemispherical analyzer [58], although suitable schemes have been developed to reduce this effect [59] or to model and correct the deterministic part of the distortion [60].

ARPES analysis techniques Basic analysis of the photoemission data is usually performed integrating the $I(\mathbf{k}, E_B)$ in suitable ranges of either energy and momentum, and displaying the result as intensity *vs.* the other variable. Integrating in momentum yields the so-called EDCs (energy distribution curves), which are actual spectra extracted at precise values of $\mathbf{k}$; integration in energy produces the MDC (momentum distribution cuts).

The simplest model to fit the EDCs is to employ a sum of Lorentzian peaks to describe the density of states, which are multiplied by a Fermi-Dirac distribution and convoluted with the Gaussian accounting for the experimental resolution. If the thermal broadening is in excess of the energy resolution, fitting the Fermi edge is also a method to retrieve the electronic temperature (cf. corresponding paragraph in Sec. 2.1.1).

The background of secondary electrons can be approximated as linear or polynomial in small energy regions (few eV), but should be described by a Shirley form or a polynomial approximation [61]. However, spurious effects due to the detector can distort the actual shape of the background and it is necessary to seek for *ad-hoc* solutions lacking the physical meaning of the Shirley background.

MDC cuts can also be modeled by a sum of Lorentzian peaks, broadened by the experimental resolution, which is typically much smaller than the linewidth of the features.

From the statistical point of view, the photoelectron analyzer records rare events in multi-dimensional histograms (kinetic energy and one or two momentum directions), and thus the number of counts N in each bin follows the Poissonian statistics with standard deviation $\sqrt{N}$ [13]. This is treated as a statistical uncertainty and propagated in the fitting procedures to determine the uncertainty on the extracted parameters.

2.2 Basics and state of the art in TR-ARPES

Time-resolved ARPES (TR-ARPES) is an extension of the equilibrium technique to the time domain by implementation of the photoemission experiment in a pump-probe scheme. It is based on pulsed sources to excite the system out of the equilibrium condition, and measure the band structure in the excited state by photoemission. This section presents the basic aspects of the technique from an experimental point of view. A detailed discussion of the photon sources for TR-ARPES is instead subject of Ch. 3.

2.2.1 Operating principles

The basic principle of a TR-ARPES experiment is illustrated in Fig. 2.6. The pump-probe scheme requires two pulses at variable time delay Δt from each other (panel (a)). The first, known as *pump*, impinges on the sample and brings it out of the equilibrium condition (panel (b)). The second pulse, called *probe*, is used to measure the system by photoemission in its excited state.

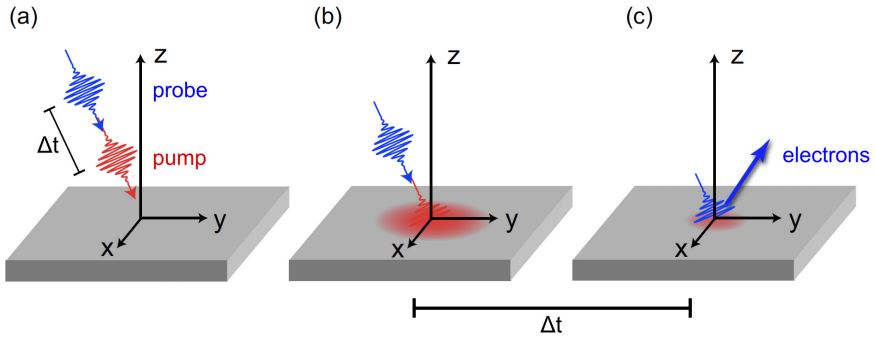

Figure 2.6: Basic principle of the TR-ARPES technique. (a) Pump and probe pulses are directed onto the sample at a Δt time distance. (b) The pump pulse impinges on the sample before the probe pulse and brings the system out of equilibrium. (c) The probe pulse photoemits the electrons from the excited sample at a time delay Δt after the pump.

Nonequilibrium conditions are by nature not stable, and the system eventually relaxes back to equilibrium. The process of excitation and relaxation towards equilibrium can be tracked by varying the time delay between the pump and the probe pulse and acquiring the band structure measurement for each delay. The condition in which the pump and the probe pulses impinge together on the sample ($\Delta t = 0$) is known as temporal overlap, or more commonly *time zero*. Negative values of Δt mean that the pump pulse arrives after the probe pulse, and thus the system is measured under unpumped conditions. Since the system is periodically excited and measured by a couple of pump and probe pulses, the unpumped condition might differ from the true equilibrium condition due to the residual effect of a previous excitation, or average heating effect of all the preceding pump pulses.

The effect of photoexcitation is visually better distinguished in difference maps between the one acquired at a specific delay Δt and the one integrated over the negative delays of the measurement. As an example, Fig. 2.7(a) shows the unpumped dispersion of Bi_2Se_3

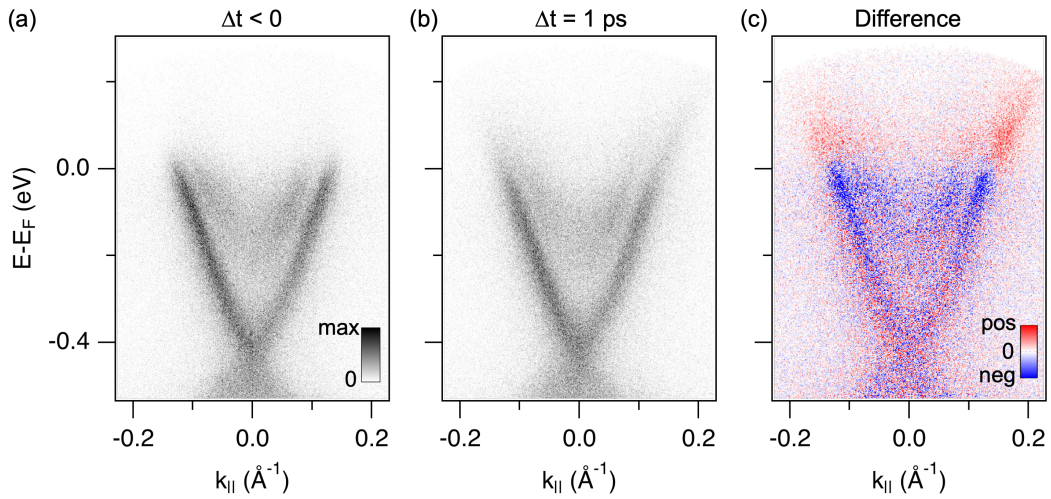

Figure 2.7: (a) Unpumped band structure of Bi_2Se_3 measured with 10.8 eV probe photon energy at 100 K. (b) Pumped band structure at $\Delta t = 1$ ps . (c) Difference between (b) and (a), plotted in false color to evidence the changes induced by the pump.

obtained with 10.8 eV probe photons at 100 K. The effect of the pump at $\Delta t = 1$ ps is visible already in the map of panel (b), especially in the population above E_F. All the effects can instead be well distinguished in the difference map between the two (panel (c)), where as customary an increase in population is shown in red and a decrease in blue. This convention of representing the pump-probe data will be used throughout this thesis.

The difference map, plotted in the appropriate color scale, highlights the regions where the number of electrons detected has decreased and the ones in which it has increased. The population variation, however, can stem from different effects, which are briefly discussed in the next section.

2.2.2 Observables in TR-ARPES

A qualitative view to understand what pump-induced changes to the photoelectron distribution can be expected in a TR-ARPES experiment is provided by the relation for the ARPES intensity of Eq. 2.4. Each of the terms expresses a contribution that might undergo a change due to the presence of the pump. Adding an explicit time dependence to the terms of Eq. 2.4 means treating the time-dependent phenomena in a quasi-static approximation, where at each time instant the formalism is the same as in the equilibrium case but with modified parameters. Although a more correct treatment based on nonequilibrium Green functions has been recently developed [37, 62, 63], it addresses discrepancies that occur at very short time delays and that are not subject of discussion in this thesis. We will thus restrict ourselves to a quasi-static approximation throughout the analysis and discussion of the results.

Band structure population: $\tilde{f}(E_B, T)$ A large part of the TR-ARPES experiments is performed to study the population dynamics induced by the pump pulse. In addition

to a sudden temperature increase in the electronic subsystem, that can reach thousands of K, the pump redistributes the electrons in a nonthermal fashion by triggering optical transitions from below E_F to the unoccupied part of the band structure above E_F. For this reason, at short time delays the distribution of electrons can be highly nonthermal, which is advantageous to study the unoccupied band structure up to energies hardly attainable at equilibrium with temperature effects alone. At later time delays, however, the distribution recovers a Fermi-Dirac distribution and allows an estimation of the electronic temperature.

Accessing the dynamics of the excited quasiparticles is also fundamental to elucidate which mechanism drives the relaxation back to equilibrium, since different interactions that are intertwined at equilibrium have distinct recovery timescales and can be disentangled in the nonequilibrium regime.

Band structure modifications: $\tilde{\mathbf{A}}(\mathbf{E_B}, \mathbf{k})$ The influence of the pump on the band structure can be of various origin, including structural deformations [64] and activation of collective excitations like phonon modes [65]. In correlated systems, photoexcitation can renormalize the effective interactions among the electrons or with collective excitations, leading to a change in the self energy and thus to a renormalization of the electronic dispersion [16]. The pump can also trigger nonequilibrium phase transitions, that are revealed by monitoring the changes in the band structure. A well-studied example is the closure or filling of the gap in correlated phases such as superconducting [66] or charge-density wave systems [67], to name a few. The excitation density required to melt the phase also carries information on its robustness [68], and thus can contribute in discerning the driving mechanisms involved. The band structure and population dynamics can then be monitored as the system relaxes back to equilibrium, and the melted phase sets in again. In general, nonequilibrium conditions can differ significantly from any possible equilibrium counterpart, hence opening the possibility to study new phases of matter under conditions unattainable at equilibrium, for example changing the temperature of the sample [69].

Matrix element effects: $\tilde{\mathbf{I_0}}(\mathbf{k}, \mathbf{E_B}, \mathbf{h}\nu,)$ The ultrafast change in the matrix element has been recently pointed out as a source of the change in the photoelectron distribution measured in photoemission possibly alternative to other explanations such as a change in the dispersion or a lattice deformation [70]. Its validation requires a system where this effect can be isolated from possible momentum-dependent redistribution of charges that might mask the matrix element variation, which is typically not the case due to the complex possible pathways involved in the relaxation. A possible pump-induced variation of the matrix elements is reported in Sec. 4.3.2.

2.2.3 TR-ARPES: experimental perspective

A detailed treatment of the photon sources is given in the next chapter; here we discuss some aspects that concern the realization of a TR-ARPES experiment and thus constrain the design of the dedicated setups.

Time resolution The possibility of detecting the nonequilibrium dynamics occurring in a photoexcited system critically depends on the time resolution attainable by the setup. The time resolution shapes the nonequilibrium signal *via* a broadening defined by the cross-correlation (XC) between pump and probe pulses. In the simple but common case of a Gaussian shape (in the time domain) of the pulses, the cross-correlation is also a Gaussian whose total FWHM is the square sum of the two:

$$FWHM_{XC} = \sqrt{FWHM_{probe}^2 + FWHM_{pump}^2}. \tag{2.7}$$

Both pulses duration hence contribute to the effective time resolution of the apparatus.

For VUV pulses, the use of autocorrelators to determine the pulse length can be challenging if not impossible due to experimental constraints. A simpler method to retrieve the experimental resolution is to look for nonequilibrium dynamics relaxing on a timescale shorter than the cross-correlation itself. In this case, if the dynamics are not exceedingly short and hence overshadowed by the noise, the response of the system follows the pump and probe cross-correlation, that can be retrieved by gaussian fit of the population dynamics (corresponding paragraph in Sec. 2.2.3).

The time resolution is among the crucial parameters of a TR-ARPES experiment, as it determines the shortest dynamics that can be probed by the setup. Its optimization depends on the possibility to shorten the pump and the probe pulses, and this sets the fundamental trade-off with the other parameters (photon energy, energy resolution, photon flux) that defines the current challenge in the advancement of the TR-ARPES state-of-the-art. In particular, a fundamental physical constraint is the Fourier transform limit [71], that in the case of Gaussian pulses limits the product of their time duration and energy bandwidth (expressed as FWHM) to 1825 meV·fs.

Space-charge effects In the time-resolved experiment, both the pump and the probe pulses can be source of space-charge effects [57, 72]. As mentioned, photoemission with ultrashort probe pulses is more prone to space-charge with respect to continuous sources, since photoelectrons are emitted in a small time window and are little separated in the time of flight towards the analyzer.

Also the interaction with photoelectrons emitted by the pump can induce space-charge effects. Since this thesis deals only with pump photon energy is much smaller than the work function of the materials, in these cases the photoemission from the pump stems from multi-photon processes and thus occurs only for particularly large excitations densities, typically of several mJ/cm^2. The interaction between the photoelectron clouds emitted by the probe and by the pump depends on their distance, and thus on the time delay. Moreover, since the probability of a multi-photon event scales with a power law on the order of the process, the largest part of pump-emitted photoelectrons has a very small kinetic energy. For this reason the probe-induced photoelectron cloud is for the largest part of the time of flight ahead of the pump-induced one, and the expected energy shift is towards higher kinetic energies [73].

Analysis of the time-resolved data It is customary to visualize the changes induced in the photoelectron distribution by integrating the photoemission intensity in suitable

regions of the E *vs.* k space and displaying it as a function of time delay. Notable examples are the exponential and double-exponential decay [74, 75], or more complex models including decay bottlenecks [76] or cascade effects [77]. In all these cases, the resolution is taken into account as a convolution with the gaussian of the cross-correlation.

As stated above, the dynamics of photoemission intensity can stem for various changes occurring either in the occupation or in the band structure itself. To determine what changes origin the observe signal, in the quasi-equilibrium approximation invoked above it is possible to perform the same EDC or MDC analysis as in the equilibrium case. The nonequilibrium data are thus fit by the same model as at equilibrium, but with modified parameters. If the effect of the pump is purely thermal, the nonequilibrium occupation function $\tilde{f}(E_B, T)$ is a Fermi-Dirac with elevated temperature. If the occupation cannot be fit with such model, the nonthermal distribution must be reproduced by suitable step functions that account for the electrons nonthermally promoted above the Fermi level.

The initial parameters are determined by fitting a suitable average over the unpumped delays. The fitting procedure is repeated for each of the delays that comprise the measurement, and the parameters of the n-th delay are used to fit the $n+1$-th delay. In this way, it is possible to reconstruct the dynamics of the fitting parameters and attribute a physical cause to the observed changes in the photoemission signal.

As shown in this chapter, the major limitations to the capabilities of a TR-ARPES setup, namely the momentum range accessible, the experimental resolution and the count rate, are largely set by the properties of the probe photon source employed. The next chapter discusses the relevant aspects of the current state of the art in this direction and introduces the principles and capabilities of the 10.8 eV setup.

Chapter 3

Light sources and experimental setups

As shown in the previous chapter, TR-ARPES is a powerful technique that can contribute to unveil aspects of the physics of condensed matter systems that would be unattainable under equilibrium conditions. Nonetheless, the fundamental parameters defining the performances of a TR-ARPES experiment, namely the photon energy (implying maximum energy and momentum range attainable), the resolution (in the energy, momentum and time domains) and the count rate, are characterized by a trade-off due to both fundamental and technical reasons. Each probe generation scheme constitutes a particular choice of compromise between these quantities. The main focus of this chapter is about the description of the principles and the realization schemes involving nonlinear processes in crystals and gases, as they constitute the building blocks of the 10.8 eV setup. The design and fundamental characterization of this setup are then presented. Since this thesis also comprises complementary measurements performed with an HHG and an FEL source, a brief description of these generation techniques and of the specific setups employed for these experiments is given.

3.1 Nonlinear optical processes in solids and gases

3.1.1 Harmonic generation by nonlinear processes in crystals

In this section we only describe those aspects of harmonic generation in crystals that are relevant to the generation of the 10.8 eV probe, referring to the existing literature for more extensive insight [78, 79].

Higher-order harmonics in the UV range can be generated employing second-order processes in crystals, in particular sum-frequency generation (SFG) and its degenerate counterpart, second-harmonic generation (SHG) [78]. By symmetry considerations, the second-order susceptibility is nonzero only in non-centrosymmetric media, hence including crystals but not liquids or gases. The parameters influencing the generation efficiency can be recognized by inspecting the relation between the intensity $I_{2\omega}$ of the generated harmonic at 2ω and the intensity I_ω of the fundamental:

$$I_{2\omega} \propto I_{\omega}^2 (\chi^{(2)})^2 L^2 \frac{\sin^2(\Delta k L/2)}{(\Delta k L/2)^2}, \tag{3.1}$$

where $\chi^{(2)}$ is the second-order susceptibility, L is the length of the crystal and Δk the phase (wavenumber) mismatch between the fundamental and the higher harmonic.

In the case of SHG: $\Delta k = \frac{4\pi}{\lambda_1}(n_2 - n_1)$, where n_j is the refractive index of the j-th harmonic and λ_1 the fundamental wavelength. Since $I_{2\omega}$ quickly falls off for $\Delta k \neq 0$, the efficiency of the generation critically depends on the *phase matching* condition $\Delta k = 0$, which requires $n_1 = n_2$. This condition can only be achieved in birefringent crystals, where the refractive index depends on the polarization of the incident light as well as on the direction of propagation. Phase matching can thus be achieved in a birefringent crystal for suitable combinations of photon energy, light polarization and incident angle. In particular, if the incoming beams have the same polarization, the phase matching is said to be of type I, while if they have different polarizations it is said to be of type II [79].

One of the limiting factors in the generation of harmonics in crystals is the difference in the optical paths of the harmonics due to the different refractive indexes experienced (temporal walk-off) [78]. The consequence is a degradation of the overlap between the two pulses. This fact affects both the generation efficiency and the time duration of the generated harmonic. This difference in the optical path is proportional to L, hence it sets a trade-off with the dependence on L^2 of the generated harmonic intensity.

Among the possible crystals for harmonic upconversion, Beta Barium Borate (β-BBO) crystals are the most commonly employed as they are transparent in a wide spectral region, offer large second-order susceptibilities and high versatility in the phase matching optimization in a very wide spectral range. The transparency of BBO crystals extends up to 6.59 eV [80], but the phase matching condition for SHG can be achieved only up to 5.9 eV [20]. The photon energy limit can be increased by employing a cascade of SHG and SFG generation in BBO, which however cannot exceed the transparency limit.

BBO-based sources are by far the most common for applications in TR-ARPES. To date, the best compromises in terms of repetition rate, bandwidth and pulse duration are achieved in this kind of setups. Due to the large conversion efficiency provided by BBO crystals (also in excess of 50% for SHG), laser sources with high repetition rate and low energy per pulse (down to a few nJ per pulse) can be used [21], as compared to the laser required for third-order processes or HHG (cf. Sec. 3.2.1). Lasers with Ti:Sapphire as a gain medium are commonly employed [20], since they can reach pulse durations well below $\sim$ 100 fs with average powers in excess of 1 W at hundreds of kHz of repetition rate, delivering several μJ per pulse. At present date, the generation schemes based on BBO crystals are the ones more commonly capable of reaching a time-bandwidth product closest to the Fourier limit [21].

The photon energy in the UV greatly simplifies the design of these setups. Since $\sim$6 eV photons are not absorbed by air, no vacuum systems for the transport to the photoemission chamber are needed, and a viewport with good transmission in the UV (made of UV Fused Silica or CaF_2) can be used to introduce the laser beam. Moreover, standard optical elements of the type employed for visible radiation can be used to manipulate

the beam after generation, in particular for the beam delivery, the focussing and the full polarization control. BBO crystals also have a good damage threshold and, being excited with moderate energy densities, are very stable on the long term and require minimal maintenance.

The low photon energy attainable constitutes the most severe limitation of these schemes, hindering the exploration of large parts of the Brillouin zone of most materials. Potassium-beryllium-fluoraborate crystals (KBBF) allow pushing this limit up to 7 eV. This photon energy is however partially absorbed by air, so the setups acquire the complication of dealing with low vacuum already at the stage of harmonic generation and delivery to the experimental chamber. Moreover, large and uniform KBBF crystals are challenging to fabricate. Since the degree of additional complication is high with respect to the gain in photon energy (less than 1 eV) and accessible k range (less than $0.05\,\text{Å}^{-1}$ at $\vartheta = 15°$), the KBBF-based setups are seldom used [20].

Above the 7 eV threshold, it is not possible to find a transparent crystal offering suitable phase-matching conditions, and the generation of a pulsed probe with higher photon energy must resort to different techniques.

3.1.2 Harmonic generation by nonlinear processes in gases

Gases, being centrosymmteric media, display only odd-order susceptibilities [81] and are thus suitable candidates for the generation of higher-order harmonics via third-order processes. In particular, frequency tripling is considered here, as it has direct application in the generation of 10.8 eV photons.

The possibility of efficiently generating the third harmonic in gases strongly depends on the focussing geometry of the fundamental beam. As shown in Fig. 3.1(a), the conversion efficiency for third harmonic generation (THG) reaches a plateau value at a fundamental power of $\sim 10^{12}\,\text{W/cm}^2$ [82]. An advantageous way to reach this value is to decrease the spot dimension by tightly focussing the beam. This approach, as we shall see, has several advantages for the generation of the harmonics and for the design of the setup.

For a tightly-focussed Gaussian beam, the total phase mismatch Δk also includes a positive contribution, coming from the Gouy phase, acquired upon passing through the focal point [83]. The condition for phase matching thus relaxes to $\Delta k = \Delta k_{geom} + \Delta k_{gas} = 0$, where $\Delta k_{gas} = k_3 - 3k_1$ is the ohase mismatch due to the gas dispersion only. With these considerations, the third harmonic intensity $I_{3\omega}$ depends on the fundamental intensity I_ω and on the medium phase mismatch Δk_{gas} via

$$I_{3\omega} \propto \begin{cases} I_\omega^3 (\chi^{(3)})^2 (\Delta k_{gas})^2 e^{\Delta k_{gas}}, & \Delta k_{gas} < 0 \\ 0, & \Delta k_{gas} > 0. \end{cases} \tag{3.2}$$

This result is plotted in Fig. 3.1(b) as a function of $b\Delta k_{gas}$, where b is the beam confocal parameter [81]. Its maximum occurs for $b\Delta k_{gas} = -2$, where it happens the exact compensation of the positive Gouy phase.

The presence of the Gouy phase related term is a key advantage for the generation of harmonics in gases. It allows exploiting the spectral regions where the gas mismatch is negative, that is a much less stringent condition than $\Delta k_{gas} = 0$. While in crystals this

condition can be achieved thanks to the birefringence, in a centrosymmetric medium like a gas it would be necessary to exploit other methods. The condition $n_1 = n_3$ can only be obtained in an anomalously dispersive region close to a resonance, where the gas has a peaked absorption, and constrains the fundamental and generated photon energies to the precise values that satisfy $n_1 = n_3$ [84]. As we shall see, with modern laser sources capable of delivering suitable energy densities, it is challenging to arbitrarily tune the fundamental photon energy while preserving high repetition rates.

The dispersion of the gaseous medium can be easily adjusted by exploiting the dependence of Δk_{gas} on the pressure of the gas, given the relation for the refractive index of the j-th harmonic:

$$n_j(p) = 1 + d_j \frac{p - p_0}{p_0}$$

where d_j is a coefficient that does not depend on the pressure [81]. Optimization of the gas pressure is also required to compensate for the dependence of the THG efficiency on the incoming power density, as reported in [82] (Fig. 3.1(c)).

We note that the medium dispersion can be adjusted up to some extent also by appropriate gas mixtures [85], but the generation efficiency critically depends on the partial pressures of the two gases and the optimization is less straightforward. As we will show, suitable choice of the laser frequency and the gas pressure allows an efficient driving of THG in Xe alone.

3.1.3 THG for TR-ARPES: experimental challenges

Among inert gases, Xe is the most suitable candidate for THG as it displays the smallest ionization energy and therefore a larger polarizability. This leads to a larger third-order susceptibility and hence a better generation efficiency [81].

Although the theoretical and experimental study of higher harmonics generation in gases largely predates the spread of BBO-based schemes, application of such methods to TR-ARPES dedicated setups requires a source providing high energy per pulse at high repetition rate (ideally, above 100 kHz). Early examples of THG applied to time-resolved photoemission employed either sources at much lower repetition rates [86], with a low number of generated photons per pulse [87], or having duration above 10 ps [88], hence unsuited for studying ultrafast processes in complex materials.

The combination of high repetition rate and high energy per pulse has become possible thanks to the advent of laser sources based on Yb-doped fibers or crystals emitting photons at 1030-1035 nm. The average power that can be delivered by these lasers is of several tens of W at MHz repetition rate, hence well in excess of 10 μJ per pulse. The time duration, however, is commonly of $\sim$ 300 fs, hence longer than the one provided by Ti:Sapphire lasers. Reducing the time duration should therefore rely on pulse compression, that can be detrimental for the energy bandwidth and thus for the resolution of the experiment.

The advent of these laser sources is rather recent, and this accounts for the limited amount of reported TR-ARPES setups based on THG in gases. We will see that the fundamental wavelength around 1030 nm allows to generate high harmonics under favorable

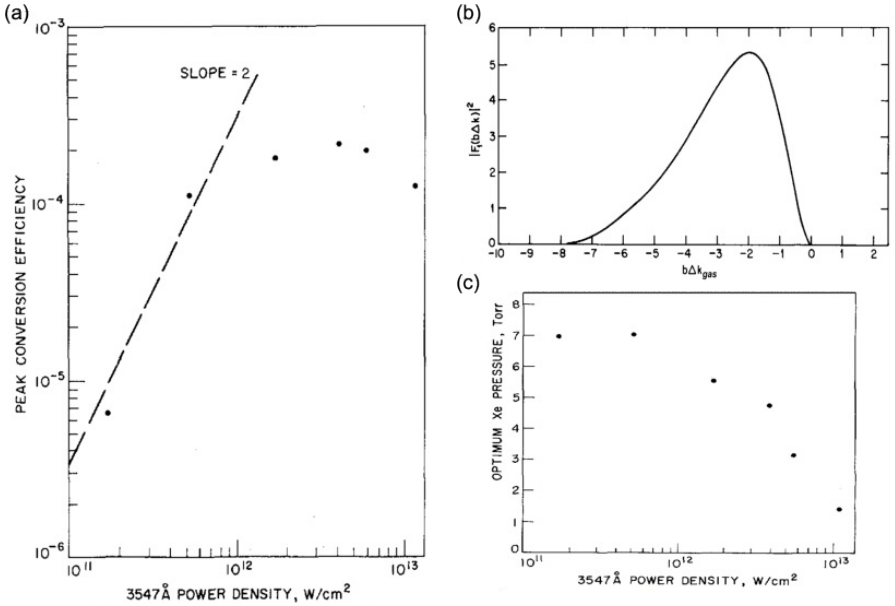

Figure 3.1: (a) Dependence of the conversion efficiency on the power density of incoming light for THG in Xe gas. The plateau is reached at around $10^{12}\,\mathrm{W/cm^2}$ [82]. (b) Dependence of the second member of Eq. 3.2, proportional to the third harmonic power, on the quantity $b\Delta k_{gas}$, where b is the beam confocal parameter and Δk_{gas} the gas-induced phase mismatch [81]. (c) Optimal Xe pressure as a function of the power density of the fundamental [82].

phase-matching conditions.

Figure 3.2(a) schematizes three possibilities for THG available with modern stat-of-art ultrafast laser sources. Panel (b) reports the phase mismatch per atom for THG in Xe, marking the three possibilities with a dashed line [89]. Shaded areas indicate where negative mismatch between the fundamental and the third harmonic occurs, and thus the THG is efficient.

As an account of the relevance of the Yb-based laser sources for the application of THG, we report as a first scheme in panel (a) the proposal by Cilento *et al.* [90] employing a Ti:sapphire regenerative amplifier (RegA). Upon frequency-doubling the fundamental (1.55 eV) and tripling the output in Xe, the result is the sixth harmonic of the fundamental (9.3 eV). However, since the first step already involves a second-order nonlinear process and the second step a third-order one, Ti:Sapphire lasers are not capable of providing the necessary energy per pulse to obtain suitable photon flux after generation. More fundamentally, this scheme is very inefficient as the photon energies fall in the region of positive phase mismatch (magenta line in panel (b)). Since in this region third-harmonic generation by four-wave mixing is not possible, it was shown that the interaction involved is a six-photon mixing [91] which, being a higher-order process, is inherently less efficient. The overall estimated generation efficiency is in fact of $\sim 10^{-9}$. Performing TR-ARPES experiments under these conditions is nonetheless possible, although with very limited statistics [90].

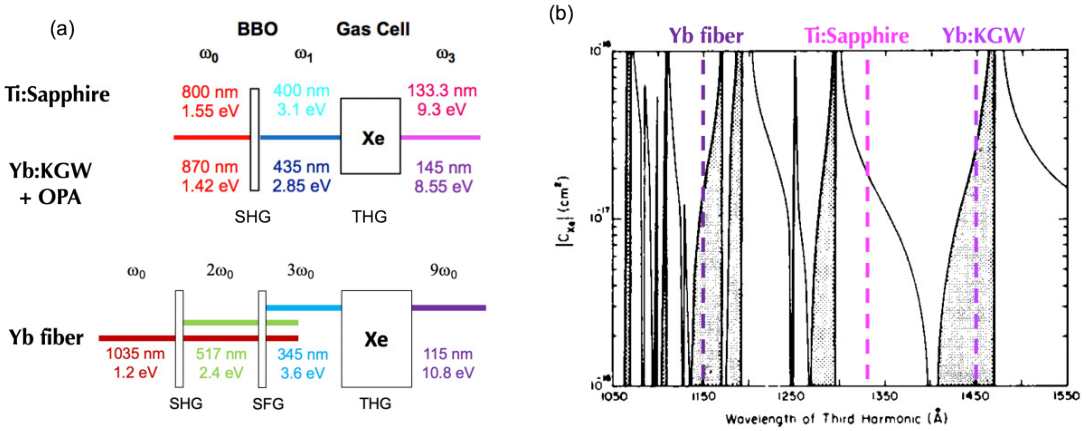

Figure 3.2: (a) Harmonic generation schemes combining frequency upconversion in BBO crystals and Xe gas for the three options described in the text. Form top to bottom: sixth harmonic generation from Ti:Sapphire source, from Yb:KGW source, and ninth harmonic from Yb-doped fiber laser. (b) Phase mismatch per Xe atom between the fundamental and the third harmonic, as a function of the generated wavelength. The dark regions are those of negative dispersion for the gas [89]. Colored lines at the third harmonic wavelengths discussed in the main text highlights the sign of the gas phase mismatch obtained in each of the three generation schemes in panel (a).

Among Yb-based sources, one possibility is to use a Yb:KGW (Potassium-Gadolinium-Tungsten) laser and pump an optical parametric amplifier (OPA), in order to adjust the initial photon energy and access a region of negative phase mismatch. The presence of an OPA renders the requirement of high energy per pulse even more stringent than the previous scheme. With a fundamental of 1.42 eV, after frequency doubling in BBO and tripling in Xe, 8.55 eV can be reached. For this photon energy, as shown by the light-violet line in panel (b), the phase mismatch is negative and the generation is inherently efficient. Nonetheless, the gain in photon energy with respect to BBO-based setups is not very large, and the optimal operation of OPAs limits the repetition rate to 50 kHz. At this repetition rate it is already possible to perform equilibrium and time-resolved measurements, but it is desirable to reach repetition values in excess of 100 kHz and ideally up to the MHz.

Similar energy per pulse can be obtained with a Yb-doped fiber as a gain medium. The fundamental photon energy is in this case of 1.2 eV; the second harmonic can be generated in a BBO crystal and combined with the fundamental to obtain the third harmonic. Within this scheme there is no need to adjust the photon energy with an OPA, since the phase mismatch for THG in Xe is negative (violet line in panel (b)) and the generation is efficient. The cascade process is also capable of providing a higher photon energy than the previous schemes, amounting to 10.8 eV. The novel TR-ARPES setup used in this thesis is an experimental implementation of this scheme for application in TR-ARPES.

3.1.4 The 10.8 eV generation setup

Figure 3.3 shows the scheme of the experimental setup to generate the 10.8 eV probe for TR-ARPES experiments. The source is the ultrafast Yb-fiber based laser Coherent

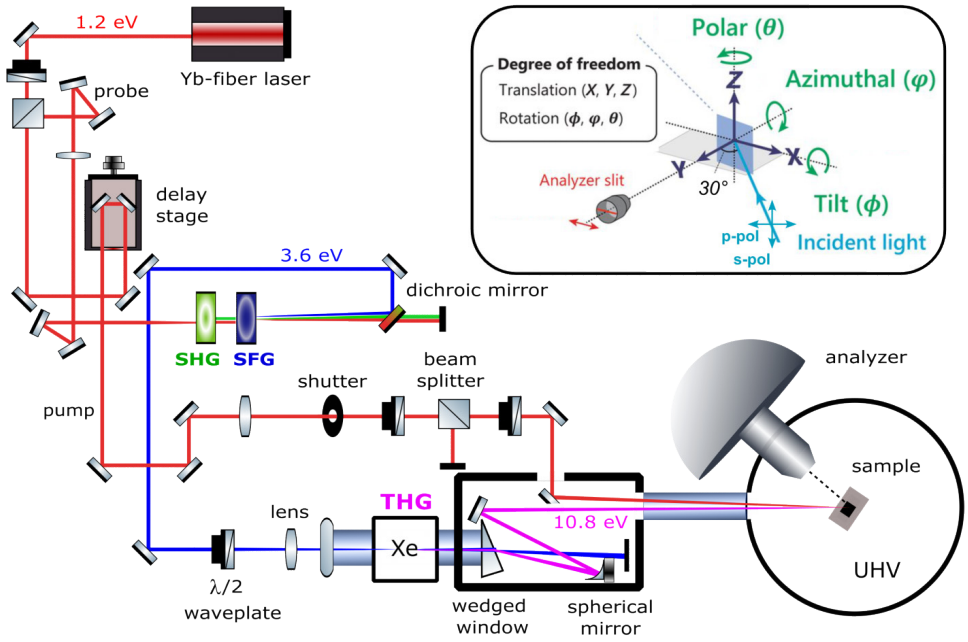

Figure 3.3: Scheme of the experimental setup for TR-ARPES with probe at 10.8 eV and pump at 1.2 eV. The inset indicates the spatial and angular degrees of freedom of a six-axes manipulator, along with the relative orientation between the sample and the p and s polarizations [92].

MONACO 1035. It produces pulses at 1.2 eV with ∼290 fs duration. The combination of a $\lambda/2$ waveplate and a polarizing beam splitter allows obtaining the pump and probe intensity with a user-defined ratio.

The reflected fraction of the beam is focussed into the BBO crystals to generate the third harmonic of the fundamental. The lower order harmonics are filtered out by reflection on dichroic mirrors. A $\lambda/2$ waveplate allows defining the polarization of the third harmonic, which is focussed in the Xe cell by a lens of +100 mm focal length. After generation, since the 10.8 eV light is absorbed by air, the beam must be handled in a vacuum environment (at least as good as 10^{-3} mbar). The generation cell is separated from the refocussing chamber by a MgF_2 wedged window which acts as a dispersive prism and allows separating the third from the ninth harmonic. The separation angle is sufficient to deflect from the beam path almost all of the third harmonic, which impinges on a beam dump. The ninth harmonic is collected by a spherical mirror (250 mm curvature radius), which allows focussing the beam at the sample position. In order to precisely adjust the pointing of the beam at the sample position, the last plane mirror is motorized with piezoelectric actuators. Both the spherical and the plane mirrors are suitably coated for optimized reflection at 10.8 eV. A MgF_2 viewport separates the refocussing chamber from the ultrahigh-vacuum analysis chamber.

The pump beam, after the first beam splitter, is directed to a motorized delay stage to control the relative delay in the pump-probe experiment and is focussed on the sample

by a lens of 1 m focal length. The pump power is regulated by a $\lambda/2$ plate placed before a polarizing beam splitter, and the output polarization (linear) can be adjusted by means of a further $\lambda/2$ plate. The angular separation between the pump and the probe beams in the refocussing chamber is minimized by using D-shaped mirror for the last reflection of the pump, so that the two beams are almost collinear when impinging on the sample.

The polarization of the ninth harmonics is the same as that of the third harmonic, hence it is entirely determined by the $\lambda/2$ waveplate placed before the generation cell. Possible birefringence effects due to the propagation through the MgF_2 elements are negligible. The orientation of s and p polarizations with respect to the sample, and of the sample with respect to the analyzer, are shown in the inset of Figure 3.3. The angle of incidence in the normal emission geometry is of 30°.

In the following paragraphs, a more detailed description of the design and operation of the crucial elements of this setup are discussed.

SHG and SFG in BBO After the first beam splitter, the probe is s polarized. It is focussed on the first BBO crystal that generates the second harmonic at 2.4 eV with p polarization [79]. The crossed polarizations of fundamental and second harmonics allow directly for type-II SFG in the second BBO crystal. This is advantageous since no waveplate must be added to change the polarization of one of the two beams. This would require compensating for the different optical path lengths experienced by the two beams in the waveplate.

The moderate duration of the pulses (∼290 fs at the laser output) renders the temporal walk-off due to the generation negligible also for crystal thicknesses of the order of the millimeter. Besides removing the complication of a delay compensation, this also allows employing thicker crystals to enhance the generation efficiency, that scales as the square of the medium length. In this way the efficiency is very high: the BBO for SHG is 2 mm thick and reaches 50% efficiency, while the BBO for SFG is 2 mm thick leading to 25% efficiency for the THG.

The refocussing chamber The 10.8 eV photon energy is very close to the abrupt transmittance cutoff of both LiF and MgF_2, that occurs slightly above 11 eV [88]. This also means that 10.8 eV is an upper limit for the implementation of a scheme not comprising diffraction gratings to monochromatize the light and differential pumping to couple the source to the experimental chamber. The choice of the optics (both in reflection and transmission) to handle the 10.8 eV light after generation must minimize losses. This also means that the thickness of the optical elements has to be reduced as much as possible.

The use of a prism to separate the harmonics in the refocussing chamber is also common to the work of Zhao *et al.* [85]. In this case, the prism employed has an apex angle in excess of 60°. However, such a large apical angle can be detrimental for the time resolution of the apparatus. When traversing the prism, different parts of the Gaussian light beam follow different paths inside the prism, with a consequent retardation of one of the two tails due to the refractive index of the prism. This is schematized in Fig. 3.4(a), which shows for simplicity the case of a pulse traversing the prism close to the apex at the minimum deviation angle (equal incidence and emergence angles). The tilting of the

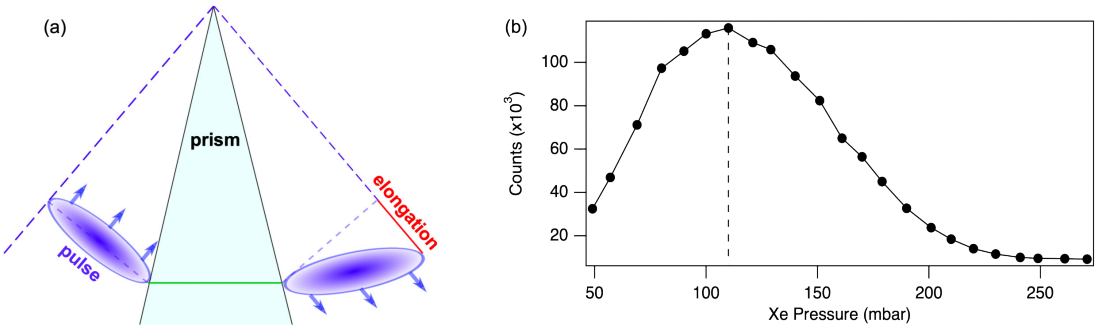

Figure 3.4: (a) Wavefront tilting due to the transmission of the beam through a prism close to the apex at the minimum deviation angle. The green line is the path of the lower tail that undergoes the maximum retardation due to the refractive index. The red segment indicates the fraction of tilting of the wavefront. (b) Number of photoemission counts as a function of the Xe pressure, with the dashed line evidencing the optimal pressure of ∼120 mbar.

wavefront results in an effective degradation of the time resolution of the setup. In order to minimize this effect, we use a MgF_2 window with 5° apex angle, which also reduces the length traversed by the pulses (less than 1 mm), thus minimizing the losses. LiF has proven to be mechanically more fragile, hence less suited for sustaining also moderate pressure differences at small thicknesses [93].

The difference in the refractive indexes for the two harmonics in MgF_2 induces a separation in excess of $\sim 2°$. A small fraction of the third harmonic can still reach the main chamber, but the deviation from the 10.8 eV beam is enough to avoid hitting the sample in the standard measurement conditions.

The alignment of the refocussing chamber is crucial for the proper operation of the setup. The 10.8 eV beam must impinge at the center of the spherical mirror in order to have optimal focussing without deformation of the focal spot. Moreover, the probe path must pass close to the pump D-shaped mirror in order to reach the main chamber with the minimum angular separation.

A major drawback in our geometry, as noted in [93], is that the third harmonic and the ninth harmonic impinge on the same spot of the wedged window, and the high power of the third harmonic degrades the window at the expenses of its overall transmittance. We observed that the MgF_2 window must be replaced less frequently than the LiF one, possibly due to the larger robustness of the material. Severe degradation of the window after long utilization times (in the order of a few months) can only be overcome by replacement of the window itself.

The refocussing chamber is purged with a continuous flux of nitrogen at moderate pressure (∼20 mbar) in order to provide a mild cooling for the optical elements, with negligible absorption of the VUV light.

3.1.5 Characterization and operation of the 10.8 eV setup

Pressure optimization inside the cell As mentioned, the realization of the perfect phase matching condition in Xe is achieved by varying the pressure inside the generation cell. The cell is filled with Xe through a limiting valve that allows precise tuning of the pressure. It is also connected through a different port to a scroll pump to evacuate the cell before every new filling with Xe. The vacuum level is monitored by a Pirani sensor, while the pressure of the Xe gas is measured with a piezo-based sensor.

In order to characterize the overall generation efficiency as a function of Xe pressure, the most suitable option would be to directly measure the ninth harmonic power with a channeltron electron multiplier, thus also allowing for an exact definition of the efficiency as the ratio between fundamental and generated power. The implementation of this instrument in the experimental setup is not straightforward, due to the vicinity of the experimental chamber to the generation cell. We thus directly monitor the ninth harmonic intensity by looking at the photoelectron count rate in an actual photoemission experiment.

The result of this procedure is reported in Fig. 3.4(b). The gas is pumped in the cell well above the typical optimal pressure, and is subsequently pumped out through the same limiting valve used to fill it. In this way the pressure can be reduced in steps of $\sim 10\,\mathrm{mbar}$ and the total number of photoemission counts is registered. The whole measurement is performed within one hour, so that long-timescale effects such as gas cell pollution or sample surface degradation are ruled out. As shown in Fig. 3.4(b), the optimal pressure equals $\sim$120 mbar. The shape of the curve is also qualitatively compatible with the one reported in Fig. 3.1(b) and in [94].

Although with this method the generation efficiency cannot be directly estimated, we point out that the possibility of observing severe probe-induced space-charge with this source demonstrates that the number of generated photons per pulse is in excess of the optimal value required by a high-resolution photoemission experiment.

Pump-probe overlap The spatial overlap between the pump and the probe beams is performed on a YAG scintillator that can be inserted at the exact position of the sample in front of the analyzer, and allows revealing both the 1.2 eV (pump) and the 10.8 eV (probe) beams. The small angular separation between the two beams also guarantees that small movements of the sample along the spatial or angular axes will not affect the overlap.

The scintillator also allows for an estimation of the pump and probe beams size with a gaussian fit of their footprint. This yields a FWHM of $\sim 260\,\mu\mathrm{m}$ and $\sim 350\,\mu\mathrm{m}$ for the probe and the pump respectively, hence guaranteeing that with optimal overlap only pumped regions are probed.

Space-charge and energy resolution The operation mode of the laser source allows following several strategies to minimize the space-charge, as summarized in Fig. 3.5. The repetition rate can be varied from single-shot to 50 MHz. Up to 1 MHz, the integrated pulse-picker offers the possibility to preserve the same energy per pulse of $40\,\mu\mathrm{J/cm^2}$ (Fig. 3.5(a,b)) while lowering the effective repetition rate and hence the average power.

Above 1 MHz instead the repetition rate is increased but the power stays constant at 40 W, hence the energy per pulse decreases (Fig. 3.5(c)).

A strategy to lower space-charge is to attenuate the probe intensity. Figure 3.5(d) shows the photoelectron spectra obtained on a gold polycrystal. Since they lack long-range crystalline order, these samples display no defined band structure and ideally the only visible feature is the Fermi level. The spectra resemble a Fermi-Dirac distribution close to the Fermi energy. In the panel, EDCs are normalized to their maximum and shifted for clarity. These curves were fit with by a Fermi-Dirac distribution convoluted with a Gaussian to account for the experimental resolution. The energy of the Fermi level is indicated on the traces as a black dot and reported as a function of the third harmonic power fraction in panel (e). For excitation densities above 80% of the maximum, the Fermi level shift seems to saturate. It is only by reducing the power to 10% of its full value that the position of the Fermi level stabilizes, indicating that the space-charge free condition is achieved. This means that, in order to operate in a space-charge free regime, a large fraction of the laser output is not used for the harmonic generation. Also the configuration schematized in panel (c) can reduce space-charge, since the number of photons per pulse is reduced in favor of the repetition rate. The spectra acquired at repetition rate up to 4 MHz are shown in panel (f). The only Fermi level position compatible with the one found in panel (d) for the space-charge free regime is the one at 4 MHz, proving the effectiveness of this approach.

What shown above proves that a higher repetition rate is a suitable route to perform space-charge free photoemission measurements. It is not possible, however, to apply in general this operation régime to the case of pump-probe experiments, since an elevated repetition rate leads to undesired average heating effects due to the large average pump power, also in the case of moderate fluences [96]. Based on the experienced gained, nonequilibrium measurements can generally be performed at repetition rate of at most 1 MHz. Higher repetition rates can be employed successfully to perform equilibrium measurements, increasing the signal the statistics in a space-charge free régime.

In a space charge-free regime, the overall energy resolution attainable with a 2 mm slit aperture of the analyzer is of ~ 80 meV, as resulting from the EDC acquired on polycrystalline gold reported in panel (f). A narrower slit (0.5 mm) allows reaching $\sim$26 meV resolution [95]. However, this operation condition impacts on the statistics of the measurement with a factor 4 less counts per second. For this reason, in presence of small pump-probe signals the larger slit is preferred. This is hence the standard measurement condition of this thesis, unless otherwise stated.

Time resolution We estimated the cross-correlation of the apparatus by fitting fast population dynamics. In Fig. 3.6 we report as an example the measurement of the population dynamics in the Dirac semimetal $NiTe_2$. The measurement is performed along the ΓM direction at large momentum values. This proves that the overlap of pump and probe beams is efficiently preserved also at large polar angles ($\sim 40°$). The lifetime of the population immediately above the Fermi level (red area in panel (b)) is shorter than our time resolution, as proven by the trace extracted in the dashed box of panel (b) and displayed in (c). The Gaussian fit of this curve yields $\sim$ 1.3 ps as FWHM, which sets the time

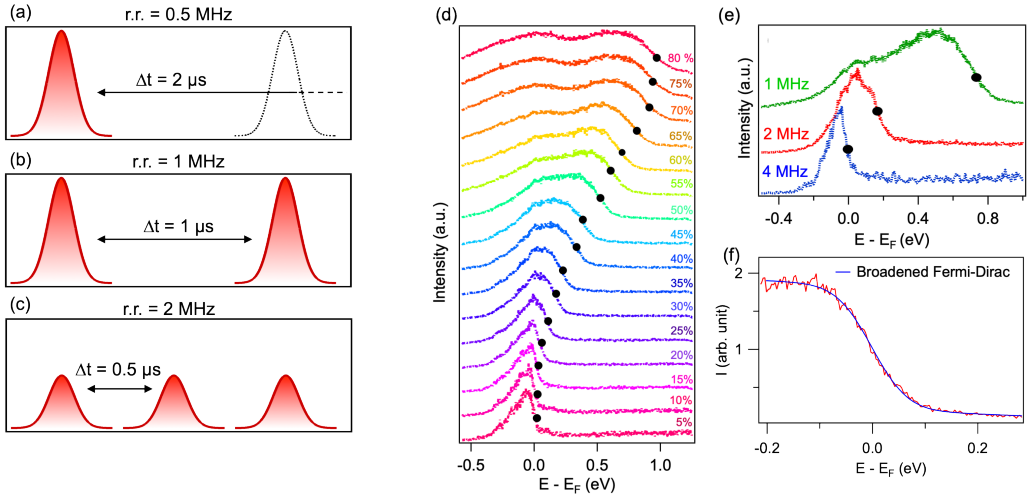

Figure 3.5: (a-c) Illustration of the built-in repetition rate tunability options in Coherent Monaco laser, here illustrated for 0.5, 1 and 2 MHz. Width and inter-pulse distance are not in scale to each other. (a) Below 1 MHz, it is possible to use the pulse-picker to reduce the effective repetition by diminishing the number of pulses, while keeping a constant energy per pulse. (b) Reference repetition rate at 1 MHz. (c) Above 1 MHz the laser delivers the same average power, hence diminishing the energy per pulse. (d) Photoemission spectra from polycrystalline Au [95] as a function of the third harmonic power at repetition rate of 1 MHz. The black dots indicate the position of the Fermi level extracted from a fit of the curves as described in the main text. Curves are normalized to the maximum and shifted for clarity. (e) Same spectra as a function of the repetition rate above 1 MHz. (d-f) are adapted from [95]. (f) EDC extracted from a polycrystalline gold sample at room temperature and with a 2 mm slit aperture, yielding ~ 80 meV Gaussian FWHM.

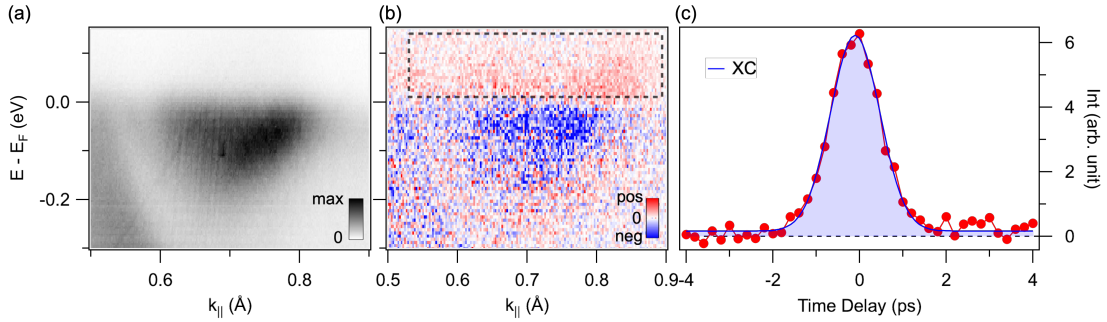

Figure 3.6: (a) Equilibrium dispersion of the Dirac semimetal $NiTe_2$ at large k values along ΓM at 110 K temperature. (c) Difference pump-probe map with the region of integration to extract the cross-correlation. (d) Trace extracted in the box of panel (c) with superimposed the Gaussian fit yielding 1.3 ps time resolution.

resolution of our experimental setup for TR-ARPES. This result agrees well with other resolution-limited effects measured with this setup on different systems (cf. Fig. 5.4 and 5.5).

Since the laser source provides fundamental pulses of ∼290 fs duration, which are also used as a pump, the origin of the time resolution must be sought in the probe pulse. The largest source of broadening along the 10.8 eV beam path is the prism used to separate the harmonics, although being very thin. The pulse chirp induced by the other optical elements cannot elongate the pulse to this extent. This point is proven by the superior time resolution (360 fs) achieved by the recent work reported in [93], where a dichroic mirror is used instead of the prism in an otherwise very similar arrangement to our 10.8 eV setup.

3.2 Light sources for complementary measurements

3.2.1 HHG sources

A further step in the quest for higher photon energies from tabletop sources is represented by the so-called high-harmonic generation (HHG). Although also the result of the nonlinear processes described in the previous sections is the generation of higher-order harmonics, the term HHG specifically designates the particular class of techniques briefly outlined in this section.

HHG is based on a highly nonlinear process fundamentally different from SHG and THG, since the latter two exploit the nonlinear contributions to the susceptibility of the medium, while the former uses the ionization of the rare gas atoms, requiring for this reason pulses of even higher energy density ($\sim 10^{14}\mathrm{W/cm^2}$). The HHG process is usually described by a phenomenological three-step model [97]. First, one or more photons from the driving pulse ionize a rare gas atom. Ionization can occur also for low driving photon energies, if the field is intense enough to deform the potential barrier experienced by the valence band electrons and allow them to escape the barrier by tunneling. However, at even higher intensities, ionization by multi-photon processes can occur. The emitted electron is accelerated by the electric field of the pulse, which reverses sign after half optical cycle,

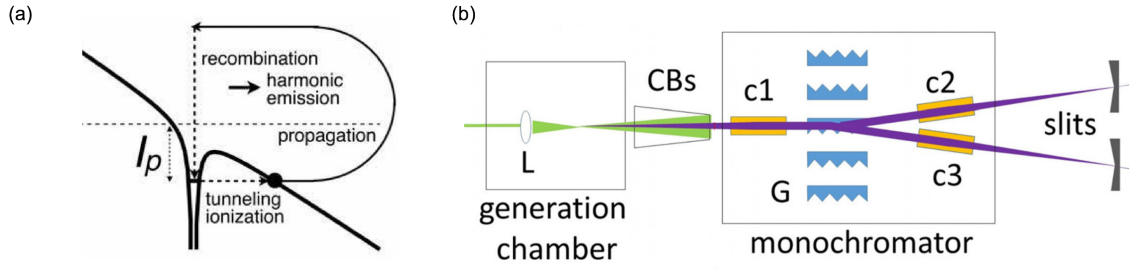

Figure 3.7: (a) Three-step model for the HHG process. The electric field deforms the atomic potential and ionizes the atom; the electron is accelerated in the vacuum and subsequently driven towards the parent ion, where upon recombination it emits one photon. (b) Detail of the generation and harmonic separation stages of the HHG setup at the SPRINT laboratory (FERMI, Elettra, Trieste). L, lens; CBs, conical beam stopper; c1, c2, c3, toroidal focussing mirrors, G, gratings. Adapted from [98].

hence driving the electron back towards the parent ion. If the recombination occurs, the excess energy acquired due to acceleration is emitted as a photon, that can range from the VUV to the X-rays.

The requirement of high fundamental power is even more stringent in HHG than in THG, since the driving electric field must be able to ionize the rare gas atoms. Typical values are in excess of 100 μJ/pulse [21], which can be provided by the laser sources already introduced above, based on Yb-doped crystals or fibers. At variance with THG in gas, the trade-off between the energy per pulse and the repetition rate is constrained to very high values of the first parameter. This fact prevents the extension of the repetition rate to the MHz regime, where HHG is still possible but with low overall efficiency. Much higher repetition rates (10-60 MHz) can be achieved with cavity-enhanced HHG [99]. However, in this regime the average power from the pump beam sets some constraints in TR-ARPES experiments.

The emission of (coherent) laser radiation from a large number of atoms is obtained when suitable phase matching conditions are fulfilled [100]. With respect to the THG, additional terms contribute to the phase mismatch between the harmonics; however, the main parameters that are adjusted in a setup to optimize the phase matching are likewise the focussing of the beam and the gas pressure. Typically, harmonics are generated in a gas jet that provides a continuous gas flux from a thin nozzle (tens of μm), hence also the relative position of the focus and the nozzle is a crucial parameter to define the interaction region. Typically, HHG sources for TR-ARPES are optimized in a range of few tens of eV, in the spectral region of approximately 10-70 eV [22].

HHG produces a discrete spectrum comprised of the sole odd harmonics of the fundamental, due to the symmetry of the process. The harmonics of interest required by the photoemission experiment is obtained by filtering out the other harmonics, *e.g.* by a selectively absorbing thin metal films or a grating monochromator [101]. Since the efficiency of the generation scales with the wavelength as $\sim \lambda^{-6}$, HHG setups for the generation of VUV radiation typically employ a first stage of frequency doubling or tripling in BBO crystals. A higher fundamental photon energy also implies a larger energy separation

among the harmonics, which is beneficial to efficiently monochromatize the output for the photoemission experiment.

Since it results in photon energies above 11 eV, the design of an HHG setup requires vacuum systems for the beam transport from the generation stage to the experimental chamber. Moreover, the beam cannot be handled with standard optical elements, hence the delivery and focussing has to rely on grazing incidence optics. The design and construction of an HHG setup is thus of a substantially higher level of complexity with respect to the sources discussed so far.

The HHG source at SPRINT The measurements of Sec. 6.2 were performed using the HHG source at the endstation of the Spin Polarized Instrument in the Nanoscale and Time (SPRINT) facility at CNR-IOM (Trieste). A photon energy larger than 11 eV was required in order to address the oxygen states in Bi2212 which lie at $k_{||} \sim 1\,\text{Å}^{-1}$ and $\sim$1 eV below the Fermi level. The measurements were performed in the SPRINT experimental chamber. The generation and the monochromator chambers comprising of the setup are shown in Fig. 3.7.

The laser source is a Yb:KGW system (LightConversion Pharos) producing 300 fs pulses at 1030 nm, with 400 μJ/pulse at 50 kHz. Above this value the repetition rate can be increased at the expense of the energy per pulse. The second harmonic that seeds the HHG is generated in a BBO crystal and is tightly focussed in the generation chamber, where a gas nozzle of $\sim 70\,\mu$m diameter delivers a constant flux of Ar at a few bar pressure. A large part of the second harmonic is blocked by a cone beam stopper. A toroidal mirror collimates the beam on the grating monochromator that selects the single harmonics. A translation stage allows selecting the specific grating, and to feed the SPRINT or the T-ReX branch. The beam is focussed on the slit aperture that selects the harmonic, and further focussed in the experimental chamber by a toroidal mirror placed in the refocusing chamber.

The setup is capable of providing an energy resolution better than 30 meV and a time resolution of $\sim$ 100 fs, hence above the Fourier limit but at the state-of-the-art for VUV HHG sources [21].

3.2.2 Free-electron laser sources

Synchrotrons, as discussed in Sec. 2.1.2, are the best suited sources for equilibrium ARPES. In particular, soft x-ray energies are customarily employed in photoemission. Time resolution can be achieved in synchrotrons by suitable bunch slicing techniques [102]; however, the photon flux achieved for sub-picosecond slicing is too small to perform a TR-ARPES experiment with high signal statistics [73]. The most natural extension of soft x-ray photoemission in the time domain is by using the emission of fourth-generation free-electron lasers (FELs).

An FEL is an amplifier based on a linear accelerator that drives the electrons along sinusoidal trajectories, causing them to emit radiation [103]. A positive feedback mechanism sets in due to the interaction of the electrons with the emitted radiation itself. The interaction modulates the spatial distribution of electrons into microbunches, that emit radiation coherently, and are further bunched by the radiation itself. The result

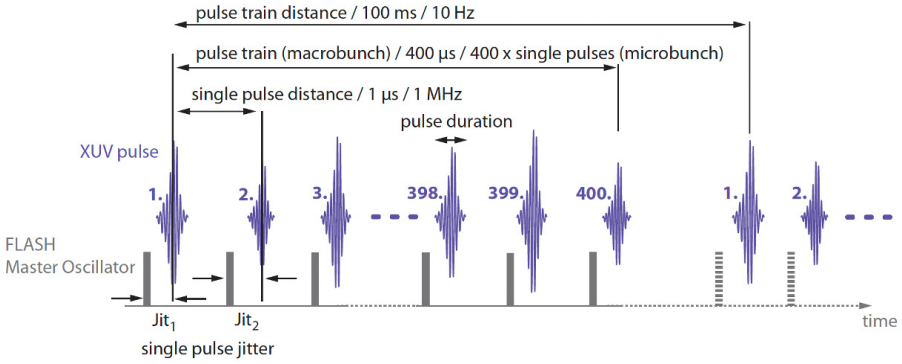

Figure 3.8: Scheme of the temporal structure of the pulses delivered by FLASH [105].

of this mechanism is the production of pulses with high peak brilliance and remarkable coherence properties. In the schemes presently in use for time-resolved photoemission, the initial modulation of the electron distribution is generated by the shot noise in the electron cloud, a process known as self-amplified spontaneous emission (SASE). The emission from an FEL is inherently pulsed, with pulse durations down to the attosecond [104]. The wavelength of the emission is selected by the parameters of the undulator, but since the process is highly nonlinear also the harmonics are present in the spectrum, and only the odd ones due to symmetry properties of the emission.

FELs are promising sources for applications in time-resolved photoemission, thanks to their capability of reaching photon energies in the soft X-rays with sub-picosecond pulse durations. Soft x-rays can be also beneficial for TR-ARPES in the valence band, having larger bulk sensitivity and hence accessing buried interfaces in heterostructures [102, 106]. The full polarization control is also a desirable feature; while THG in gas and HHG only allow for linear polarization, generation of circular polarization is attainable only by FELs [107].

FELs also pave the way to the development of the ultrafast counterpart of techniques such as X-ray photoelectron spectroscopy (TR-XPS) and diffraction (TR-XPD), to gain chemical and environmental sensitivity and study the photoinduced lineshape modifications in the core levels due to the generation of hot carriers [108], ultrafast phase transitions [73], screening dynamics [109] and charge redistribution (cf. Sec.6.3).

The Momentum Microscope instrument at PG2-FLASH FLASH (DESY, Hamburg) is historically the first FEL operating in the VUV and soft X-ray spectral regions [110]. It can deliver pulses of photon energy from 25 eV to 300 eV in the fundamental, hence reaching 900 eV in the third harmonic. The temporal structure of the pulses is shown in Fig. 3.8. The repetition rate of the pulses within each train is 1 MHz, with 400 pulses per train, while the repetition rate of the pulse trains is of 10 Hz. The average repetition rate is thus 4 kHz. The beamline PG2 is capable of delivering monochromatic light, being equipped with a plane-grating monochromator to select the harmonic of interest. The grating induces a tilt in the wavefront that effectively elongates the probe pulses up to ~ 150 fs. Given the low repetition rate, the operation conditions are usually close to the

space-charge limit.

The pump pulses, coming from a Yb-YAG amplifier, have a fundamental photon energy of 1.2 eV and can be compressed down to 70 fs after broadening in a Herriott-type cell [111]. The pump laser is synchronized with the FEL pulses [112] with typical jitter of the order of 50 fs, which together with the probe pulse broadening is the major contribution to the time resolution of the experiments. The two beams are coupled before the analysis chamber in a quasi-collinear configuration.

Photoelectron spectroscopy at an FEL can be performed with hemispherical analyzers [57], but a fascinating possibility is to exploit the capabilities offered by momentum microscopes (Sec. 2.1.2). In addition to the advantages for TR-ARPES already discussed, the rather limited count statistics provided by the repetition rate of 4 kHz can be partially counterbalanced by the wide angular acceptance of the momentum microscope, capable of detecting photoelectrons emitted in the full solid angle. Moreover, in the soft x-ray régime, the capability of simultaneously resolving two momentum directions allows recording the two-dimensional diffraction patterns of core-level photoelectrons to perform a TR-XPD experiment [113].

The momentum microscope at FLASH, designed by the group of Prof Gerd Schönhense, is based on a time-of-flight scheme with a delay-line detector [23]. At variance with ordinary delay lines, that are capable of recording one event at a time, the 2D detector of this instrument is divided in four independent delay-line quadrants, thus allowing the detection of up to four electrons per each FEL shot, with advantage for the statistics of the measurement. The lens column can also be operated as a filter to cut out spurious electrons of lower energy that would impinge on the detector and contribute to the background. The PEEM mode allows for the imaging of the pump and probe spots directly at the sample position, in order to perform spatial overlap and estimate the spot size for accurate fluence calculations.

The detection is performed on a shot-to-shot basis. Each electron is recorded as an event with specific values of the parameters of the electron itself (kinetic energy and two momentum values) and of the FEL-pump couple of pulses that generated it (photon energy, intensity, polarization, time delay, ...). The data are then sorted in multidimensional histograms as a function of the quantities of interest, taking the average along the others [114].

3.3 Outlook

In the trade-off between the numerous parameters that characterize a pulsed light source, each of the generation methods described in this chapter offers specific capabilities and compromises, hence representing a complement to the other sources with respect to one or more of the parameters. For example, the BBO-based setups offer high resolutions and count rates, but at low photon energy (<7 eV), while HHG sources offer high photon energies but at the expenses of either the resolution or the count rates. The advancements in one of the techniques are essentially oriented to overcome one or more of the limitations that characterize that specific technique and reduce the gap with the capabilities offered by another.

In this perspective, THG in gas can be viewed as a development that conceptually evolves from the SHG-based setups and, employing interactions of the same class but of higher order, pushes the photon energy limit towards that achieved with HHG setups. With respect to these, THG in gas preserves a simpler design of the generation and the need for a lower energy per pulse, and thus the possibility to achieve the space-charge free regime upon operating at high repetition rates, without lowering the number of photoelectron counts per second below reasonable limits. The major drawback of the 10.8 eV setup described in this work is the time resolution, that is outperformed both by BBO-based and HHG sources. Since the 9HG generation only requires a few μJ per pulse, the excess power delivered by the source laser can be used on the pump path to pump an OPA that, in addition to the possibility of tuning the photon energy, can shorten the pump pulse. Since the major source of broadening comes from the separation of the harmonics after generation, shortening the probe pulse is the most important and urgent improvement to the 10.8 eV source.

An approach similar to the generation of THG in a gas cell was used by Lee *et. al.* [115] who employed a hollow-core fiber filled with Xe gas for the generation and a grating monochromator to separate the third and the ninth harmonic. The setup operates at a repetition rate of up to 250 kHz, with energy and time resolution of 16 meV and 250 fs. After this and our work [95], Kawwaguchi *et. al.* [93] reported on a setup for TR-ARPES based on the same scheme generation scheme as the 10.8 eV setup (SHG in type-I BBO, SFG in type-II BBO, THG in Xe), but with a different refocussing geometry. In this setup, a dichroic mirror is used to separate the harmonics, and the sole ninth harmonic passes through a thick LiF lens that focusses the beam on the sample. The energy and time resolution achieved in this case are 25 meV and 360 fs.

Based on these evidences, we conclude that the separation of the harmonics by means of a wedged window is not optimal to preserve the time resolution of the setup, since it has a considerable impact on the probe pulse duration. A dichroic mirror can be an option that preserves the simplicity of the design, although the geometry of the refocussing chamber should be changed since it must be operated at relatively grazing incidence to minimize losses [93]. Moreover, it only works with *p*-polarized ninth harmonic, hence the polarization must be set directly by rotating the 10.8 eV electric filed with custom waveplates. For these reasons, a near-incidence grating monochromator seems to be a better choice since allows keeping the compactness and ease of operation of the present setup, while substantially improving the time resolution. This advancement would bring the time resolution closer to the ones achieved by typical BBO-based and HHG sources, while preserving the parameters that define the uniqueness of this source. In this respect, the 10.8 eV source would offer a unique compromise between count statistics and time-energy resolution for TR-ARPES with probe energy the low portion of the VUV spectrum.

Chapter 4

Spin-orbit coupling in the topological insulator Bi_2Se_3

After having discussed the relevant features of the novel 10.8 eV setup, this chapter focusses on the first sample system investigated, the topological insulator Bi_2Se_3. The large nonequilibrium signal typically found in this material makes it a good system to assess the capabilities of our TR-ARPES setup. Despite the numerous ARPES experiments reported on the subject, however, the band structure of Bi_2Se_3 still presents aspects that are not fully explored and understood by the current state-of-the art. This chapter deals in particular with the role of the spin-orbit coupling (SOC) in shaping the dispersion close to the E_F.

The first part of the chapter introduces the basic aspects of the physics of topological insulators and especially of the role of the SOC in these systems. The second part illustrates the role of SOC in defining the Bi_2Se_3 dispersion as revealed by *ab-initio* photoemission calculations. The comparison of these calculations with the ARPES and TR-ARPES measurements performed with the 10.8 eV setup occupies the third part and gives a physically sound reason for the SOC-dependent calculations, showing evidences that the effective value of the SOC transferred at the surface of Bi_2Se_3 is reduced from its full atomic value.

4.1 Basic physical properties of topological insulators

Topology was first introduced in the description of the electronic properties of solids with the discovery of the quantum Hall effect, that occurs in a 2D electron gas at low temperature under a perpendicular magnetic field [5]. The quantization of the energy levels associated with the circular motion of the electrons is equivalent to a gap opening in the electronic spectrum, that defines the system as insulating. At the edges, however, the open orbits actually form conducting states (Fig. 4.1a), at variance with a band insulator that hosts no conducting states. The difference between these two kinds of insulator can be described in terms of the topological properties of the band structure [116]. Topology classifies surfaces depending on the number of holes they possess or, equivalently, on the value of the integration of the Gaussian curvature on the whole surface, called topological invariant [117]. No smooth transformation can lead to a surface with a different number of

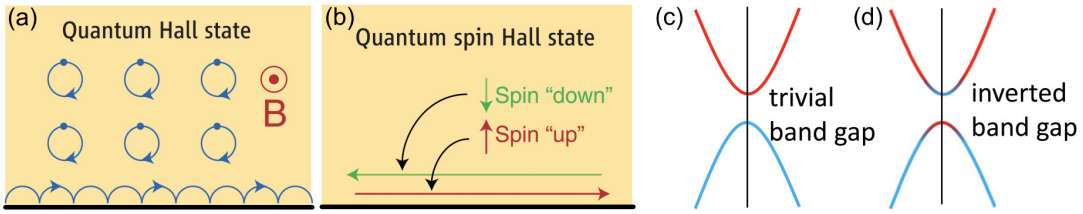

Figure 4.1: (a) Representation of the electronic motion in the quantum Hall insulator state under an applied magnetic field **B** pointing out of the plane. The incomplete circular orbits at the edges originate the conducting edge states [120]. (b) Spin-polarized edge currents in the quantum spin-Hall state [120]. (c) Trivial bandgap between valence and conduction band of different orbital character [121]. (d) Band character inversion across the gap due to SOC [121].

holes, *i.e.* a different topological invariant. In the theory of the quantum Hall effect, the topological invariant is obtained by integrating its Berry curvature [118] over the whole Brillouin zone, a quantity known as Chern number n [119]. The quantum Hall state is distinguished from a trivial insulator (like the vacuum itself) because of a different value of n. At the edge between a quantum Hall insulator ($n = 1$) and the vacuum ($n = 0$) the gap must close to allow for the discontinuous change in n. The topological theory of the quantum Hall effect hence accounts for the existence of conducting edge states.

4.1.1 SOC in 3D topological insulators

Realization of a nontrivial topological phase of matter is also possible without any external magnetic field. In the following only the 3D case will be discussed, where the interior of the system is the bulk and the edge states become surface states. Since the bulk of these systems is insulating, and the electronic properties of bulk and surface are classified in terms of the band structure topology, these systems are known as topological insulators.

Phenomenologically, the interaction of electrons with the external magnetic field that originates the quantum Hall effect is mimicked in 3D topological insulators by the presence of the SOC [122]. At variance with the quantum Hall effect, where the magnetic field breaks the time-reversal symmetry, the SOC preserves this symmetry, which is a necessary condition to realize a topological insulator [123]. The presence of the SOC causes the surface currents (analogous to the edge currents of the 2D case) to be counter-propagating spin-polarized currents (Fig. 4.1(b)). For this reason this phenomenon is called quantum spin-Hall effect.

Regarding the band structure, the SOC interaction combined with crystal field opens a gap in the spectrum of systems lacking inversion symmetry [5]. A necessary but not sufficient condition for the insulator to be topologically non-trivial is that SOC induces an inversion of the valence and conduction band orbital character (Fig. 4.1(c,d)). If this happens, it is the exact value of the topological invariant that assesses the trivial or nontrivial nature of the insulator, depending on the Hamiltonian of the system. The topological invariant for time-reversal symmetric systems, indicated with ν, is computed

differently from the Chern number [121]. It is the sole parity of ν that differentiates trivial (even ν) and nontrivial (odd ν) insulators, and for this reason ν is a $\mathbb{Z}_2$ topological invariant, as only two equivalence classes are distinguished.

The existence of conducting states at the surface is revealed in the band structure by the presence of surface states located in the gap between the bulk valence band (BVB) and the bulk conduction band (BCB), called for this reason topological surface states (TSS). The TSSs are linearly dispersing and described by the Dirac equation [124]. This can happen also for a trivial insulator, and also in the presence of band inversion. What characterizes the system as a nontrivial insulator is the number of surface states crossing E_F between two high-symmetry points, which is an equivalent definition of the $\mathbb{Z}_2$ invariant ν [125]. The combination of the SOC and the translational symmetry breaking induced by the surface lifts the spin degeneracy everywhere in the Brillouin zone, and thus TSSs are spin-polarized, accounting also for the spin-polarization of the surface currents in the quantum spin-Hall effect. The degeneracy is preserved due to the Kramers theorem for the high-symmetry points where inversion symmetry is valid [122]. This means that at these points the spin-polarized surface states cross, so that the net spin polarization vanishes. In the ideal case, the dispersion of the Dirac states is linear and defines a cone in the E *vs.* (k_x, k_y) space, with the crossing acting as origin of the cone, and thus known as Dirac point (DP).

The simplest system predicted to host the quantum spin-Hall effect in two dimensions is graphene [126]. Carbon, being a light element, has a small SOC, and the gap is predicted to be smaller than 1 meV, hence easily masked by thermal effects and experimentally difficult to access. A measurable gap size can be obtained by addressing compounds of heavier elements. The realization of the spin-Hall effect in a 2D system was first proven in HgTe quantum wells [127] and later in the 3D alloy compound $Bi_{1-x}Sb_x$, although in this case with a relatively small band gap ($\sim$50 meV) and several crossings of the surface state at E_F [128].

A larger band gap and a simpler Fermi surface structure can be found in the so-called second generation topological insulators Bi_2Se_3 [129], Bi_2Te_3 [130] and Sb_2Te_3 [131]. In this family, the topological character derives from the inversion of the p bands at the Γ point, and the inverted band gap hosts a single Dirac cone. Due to the large bandgap, much in excess of the room-temperature k_BT, these systems enable observation of topological physics also at high temperatures, in addition to the simplicity of the Fermi surface with respect to the $Bi_{1-x}Sb_x$ alloys [132]. For this reason they are known as "the hydrogen atom" of topological insulators [133] and are the most extensively studied by means of various probes [134, 135] and ARPES in particular [136, 137]. In as-grown Sb_2Te_3 the DP occurs above the Fermi level, so it is inaccessible under equilibrium conditions. The DP in Bi_2Te_3 occurs instead below the valence band maximum, buried in an "M"-shaped dip of the valence band dispersion [130]. Conversely, Bi_2Se_3 displays a Dirac cone crossing the Fermi level and well separated from the bulk bands [36]. For this reason it constitutes the ideal candidate to investigate the dispersion of the whole Dirac cone by means of direct photoemission.

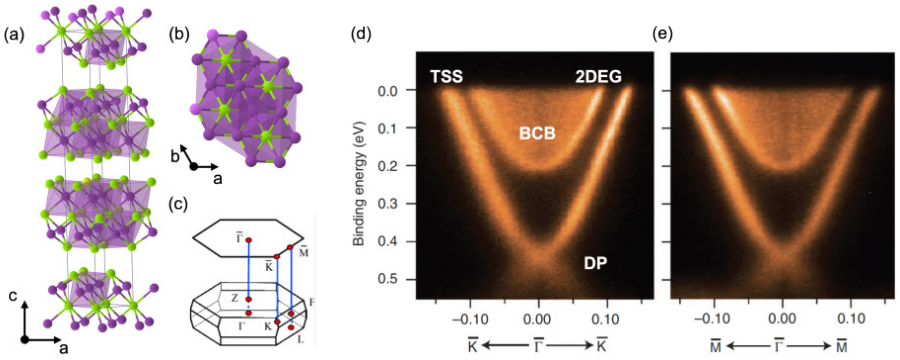

Figure 4.2: (a) Side view of the unit cell of Bi_2Se_3. The unit cell comprises three quintuple layers in total due to the stacking order of the planes. (b) Top view of the cell evidencing its hexagonal symmetry. These two panels have been generated using the software VESTA [140]. (c) Bulk and surface-projected Brillouin zone with the common nomenclature for the high-symmetry points. (d) Dispersion of Bi_2Se_3 along the ΓK direction measured with 16 eV photons. The topological surface state (TSS), the 2D electron gas (2DEG) and the bulk conduction band (BCB) are visible. The DP is also indicated. Adapted from [139]. (e) Same as in (d) but along the ΓM direction [139].

4.1.2 SOC and dispersion in Bi_2Se_3

Bi_2Se_3 has a rombohedral crystal structure composed of quintuple layers of alternated Bi and Se planes (Fig.4.2(a)) with hexagonal symmetry (Fig.4.2(b),(c)).

The dispersion of Bi_2Se_3 close to E_F and Γ is shown in Fig. 4.2(d),(e) for the two high-symmetry directions ΓK and ΓM. In addition to the TSS of characteristic "V" shape, the position of the Fermi level is such that also a part of the BCB is populated, and is in fact visible as a diffuse intensity inside the Dirac cone. This is due to a finite intrinsic electron doping that moves the chemical potential above the minimum of the BCB. This effect is already present in the as-grown sample due to substitutional defects of Bi atoms with Se atoms in the bulk. The effect can increase with the sample aging and the creation of additional defects at the surface [138]. The measurements additionally show a parabolic-like band between the Dirac cone and the BCB. This feature was attributed to a two-dimensional electron gas confined to the surface and arising from defects at the surface and sample aging [139].

The dispersion of the Dirac cone in Bi_2Se_3 is only approximately linear close to the Dirac point [141], but recovers linearity from ∼100 meV above the DP. Along ΓK, linearity is preserved up to the Fermi level (Fig. 4.2(d)). Along ΓM, instead, the dispersion starts to deviate significantly from linearity, with the band velocity that decreases upon approaching E_F (Fig. 4.2(d)). This behavior is more clearly seen in the $k_x - k_y$ cuts of the two-dimensional band structure at constant energy (Fig. 4.3(a)). In the energy region close to the DP, the constant energy surfaces (CESs) are circular, as expected for ideal Dirac states. Upon approaching the Fermi level, the CES is gradually deformed into a hexagon. Further measurements suitable to detect the unoccupied states above E_F show how the effect is more pronounced as the distance from the DP increases [17]. This de-

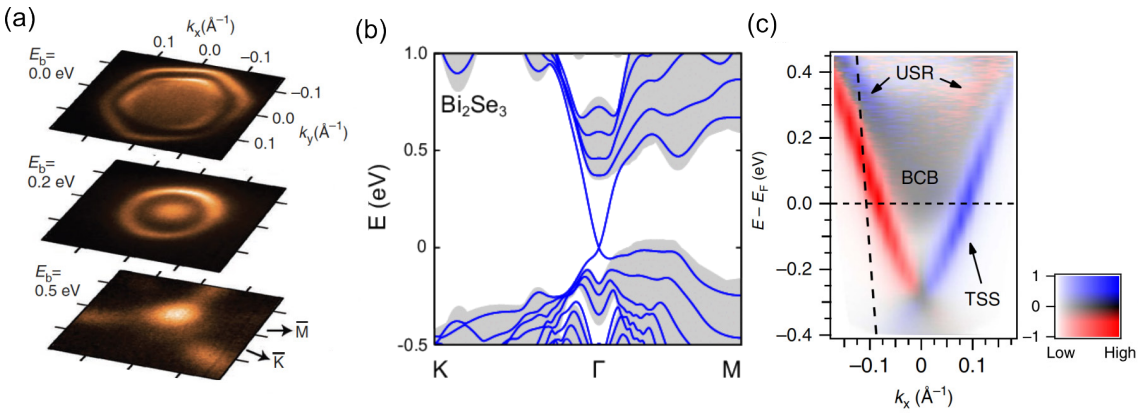

Figure 4.3: (a) Constant-energy surfaces (CES) for three energies from the Dirac point to the Fermi level. The uppermost one shows the hexagonal warping of the TSS [139]. (b) Calculated surface (blue lines) and surface-projected bulk band structure (grey areas) for Bi_2Se_3 along ΓK (left side of the k axis) and ΓM (right side) [147]. (c) Spin-resolved pump-probe measurement at time zero with 6 eV probe photon energy, showing the existence of the surface resonance (here indicated with URS, unoccupied resonance state). The color scale is reported in the right bottom corner, indicating the magnitude of spin polarization (vertical axis) and the photoemission intensity (horizontal axis) [148].

formation, known as hexagonal warping, is ubiquitous among 3D topological insulators and their alloys, although with different deformation strengths [138, 142]. Bi_2Te_3 displays the strongest warping, with the CESs that deviate already at the Fermi energy from the hexagonal shape towards a more severe deformation called snowflake-like [130, 143]. Intriguing consequences in the physics of topological insulators were predicted and observed, like strong quasiparticle interference [144], the possibility of hosting spin density waves due to the nesting of the Fermi surface [145], and in general a disruption of the in-plane perpendicular spin-momentum locking typical of TSS [146].

The hexagonal symmetry of the warped TSS contour indicates that the symmetry properties of the bulk are transferred to the surface, suggesting an interaction between the two [149]. In fact, the strong differentiation of the TSS dispersion along ΓK and ΓM can be traced back to the different dispersion of the surface-projected bulk band structure along these high-symmetry directions (Fig. 4.3(b)) [147]. However, the direct hybridization between the TSS and the bulk states is believed to be small, also in view of the striking difference in the relaxation times of the two populations [150]. The interaction with the bulk is instead accounted for in terms of hybridization mediated by the surface resonance states (SRS) [151]. These states originate from the BCB and reside within it but have a strong component localized in the surface [152]. As visible in Fig. 4.3(c), the SRS in Bi_2Se_3 lies in the unoccupied part of the spectrum and exhibits opposite spin polarization with respect to the TSS [148, 150]. Its presence causes a decrease of the BCB population, which explains the small hybridization among of the TSS with the BCB in favor of the SRS or, equivalently, that the TSS hybridizes with the bulk *via* the SRS, owing to the strong bulk character of the latter [149].

The hexagonal warping of the CESs in 3D topological insulators is most often ex-

plained as a consequence of the **k**-dependent influence of the SOC on the band structure, described in the framework of the semi-empirical $\mathbf{k} \cdot \mathbf{p}$ perturbation theory [145, 153]. In this model, the effect of SOC on the dispersion is accounted for by a term that is cubic in **k** and is known as Dresselhaus SOC [10]. While correctly reproducing the shape of the CESs, the first attempts to use this model indicated that the warping originates from an increase in the band velocity along ΓK, which results in an inward bending of the circular CES along this direction [145, 154]. As pointed out in several works [143, 155] this is incompatible with the experimental observations both in Bi_2Se_3 and Bi_2Te_3, where the dispersion seems to be linear along ΓK and bend outwards along ΓM, as shown above for Bi_2Se_3. It also requires an additional term proportional to k^5 to account for the non-planar spin components due to the warping [142]. In contrast, first principle calculations can correctly account for these phenomena and are being increasingly applied to describe these nontrivial features of 3d topological insulators [17, 146, 153, 156, 157].

Summarizing, we have introduced the role of the SOC in defining the physics of topological insulators. That the SOC has a major impact on the bulk band structure is demonstrated by the SOC-induced inverted bandgap opening, as schematically shown in Fig. 4.1(d). The bulk dispersion in turn influences the TSS dispersion via the SRS, as the symmetry of the TSS warping shows. Also the $\mathbf{k} \cdot \mathbf{p}$ model, although semi-empirical and not fully capable of accounting for the surface-bulk interaction, indicates a dependence of the TSS warping on the SOC strength. In the next section we will see how the strength of the SOC strength is influencing the bulk and surface states for the particular case of Bi_2Se_3.

4.2 *Ab-initio* one-step photoemission calculations varying the SOC strength

Despite the considerable effort in the theoretical and experimental characterization of the band structure properties of 3D topological insulators, a detailed first-principle investigation describing the role of the SOC in the TSS dispersion is still lacking. Tight-binding calculations are reported for variable SOC strength for Bi_2Se_3 to rationalize the origin and the spin-polarization properties of the surface resonance state in Bi_2Se_3, but the warping of CESs was not investigated [148]. More in general, several studies report the band structure calculations with and without SOC [133, 158], but not a detailed investigation of the dependence of the TSS dispersion on the SOC strength. Motivated by these evidences, we started a collaboration with Dr. Jürgen Braun (LMU) who performed *ab-initio* one-step photoemission calculations on Bi_2Se_3 varying the SOC strength close to the surface in order to characterize which is the role of the SOC in shaping the TSS dispersion and in particular the TSS warping.

The physical background consists in the fact that surface states are not emerging from the single ion-core potentials of the semi-infinite solid that determine the bulk electronic properties, rather by the reduced symmetry of the system introduced by the presence of the surface itself. In the calculations, the surface region is accounted for by a realistic surface potential barrier, typically of Rundgren-Malmström type, which has been successfully applied in particular to the case of Bi_2Se_3 [148]. The presence of the surface barrier and its coupling to the atomic potentials of the surface-most layer can be dealt with by multiple scattering theory [159]. Inclusion of such a surface potential in the theoretical model allows for quantitatively describing the dispersion behavior as well as the energetic position of all types of surface states and surface resonances. The surface potential, however, includes no relativistic effects, at variance with the atomic ion-core potentials which are determined in context of the fully-relativistic Dirac equation. Due to this mechanism, the amount of SOC transferred to the surface is smaller than the full atomic value that determines the purely bulk properties. Broadly speaking, the presence of the surface potential filters the SOC strength as experienced by the surface features of the band structure [151].

This description was first applied to the Shockley surface states of low-index metal surfaces, like the (111) surface of Ag, Pt [160] and Au [159]. In particular, the Rashba splitting observed by ARPES on Au(111) was reproduced in calculations assuming an effective SOC transfer between bulk and surface of 50 %. However, the case of the TSS in topological insulators is different, since these states extend for about 20 atomic layers into the bulk, and thus they retain a marked bulk character, due to the nontrivial topology of the bulk bands that allows their existence [151]. Furthermore, the interaction with the bulk states is not direct, but mediated via hybridization with the SRS [149, 161]. This way the SRS is able to modify via multiple scattering processes the strength of the atomic SOC which determines the dispersion of the TSS. In other words, it is not sufficient to reduce the strength of the SOC in the surface region, nor it is possible to apply in a direct way a theoretical formalism to compute the scattering properties needed. As a consequence, the fraction of SOC transferred to the TSS in the presence of the interaction with the SRS cannot be determined by first principles. The solution we propose consists

in a model where the SOC strength in the first 20 layers is artificially scaled. Bi is more than a factor 2 heavier than Se, and thus its SOC has the largest influence on the band structure. Fir this reason, the SOC scaling is conducted only on the Bi atoms, in the near-surface region of the semi-infinite bulk. We point out that the pure band structure calculation is performed within the full value of the SOC for all layers of the semi-infinite bulk. The atomic potentials are then used as input properties for the photoemission calculation, which includes the surface barrier and its coupling to the atomic potentials *via* multiple scattering. The SOC of the Bi atoms is varied only in the photoemission step of the complete calculation: in this way, our model simulates the situation where the bulk properties are determined by the full SOC, but the surface resonances experience a reduced SOC due to the surface-most Bi atoms, which is transferred *via* hybridization to the TSS.

The self-consistent electronic structure calculations are performed *ab-initio* in a spin-density functional theory in a fully relativistic way, solving the full Dirac equation. The Perdew-Burke-Ernzerhof parametrization is used for the exchange and correlation potentials [162]. The spectroscopical analysis is based on the spin-density matrix formulation of the fully relativistic one-step model [163]. Within this approach the final state is a spin-polarized inverse LEED state [151]. As the Rundgren-Malström surface barrier implies a z-dependent potential, the total photocurrent also includes a surface contribution that explicitly accounts for the dispersion of all the surface features. Furthermore, the relative intensities of surface-related spectral features are quantitatively accounted for by calculating the corresponding matrix elements in the surface region [159], hence accounting also for final-state effects.

To analyze in detail the impact of the SOC on the TSS, its strength is scaled from 100 % of its full atomic value to 85 %, 70 % and 50 %. The underlying approach focuses on the SOC term of the first-principle Hamiltonian while leaving all other relativistic corrections unchanged [164]. In the following, manipulation of the SOC strength is understood to be conducted in this way.

Figure 4.4(a) shows the calculated photoemission maps along the ΓK direction for s-polarized 10.8 eV photons from slightly below the DP to ∼800 meV above it. The energy scale is relative to the DP ($E - E_D$). The linearly dispersing Dirac cone displays the characteristic "V" shape above the DP, while close to it the dispersion slightly deviates from exact linearity as commented above. This is the result of final-state and surface potential effects that, as commented above, are fully taken into account in our model [156]. The part below the DP instead strongly deviates from the linear dispersion, displaying an "M"-like shape (dashed red box) reminiscent of what reported in Bi_2Te_3 [36]. No population is observed in between the two branches of the TSS up to ∼ 500 meV above the DP. From here to higher energies a small diffuse population is visible, which we attribute to the surface projection of the BCB. Around ∼ 800 meV above the DP a second sharp feature emerges (dashed blue box). The position and dispersion of this feature is compatible with the surface resonance state introduced in Sec. 4.1.2. No signature of the 2DEG is instead visible, since the *ab initio* calculations do not take into account surface defects or sample aging, which determine the emergence of this band.

Upon decreasing the SOC strength (panels (b-d)), several changes occur in the band

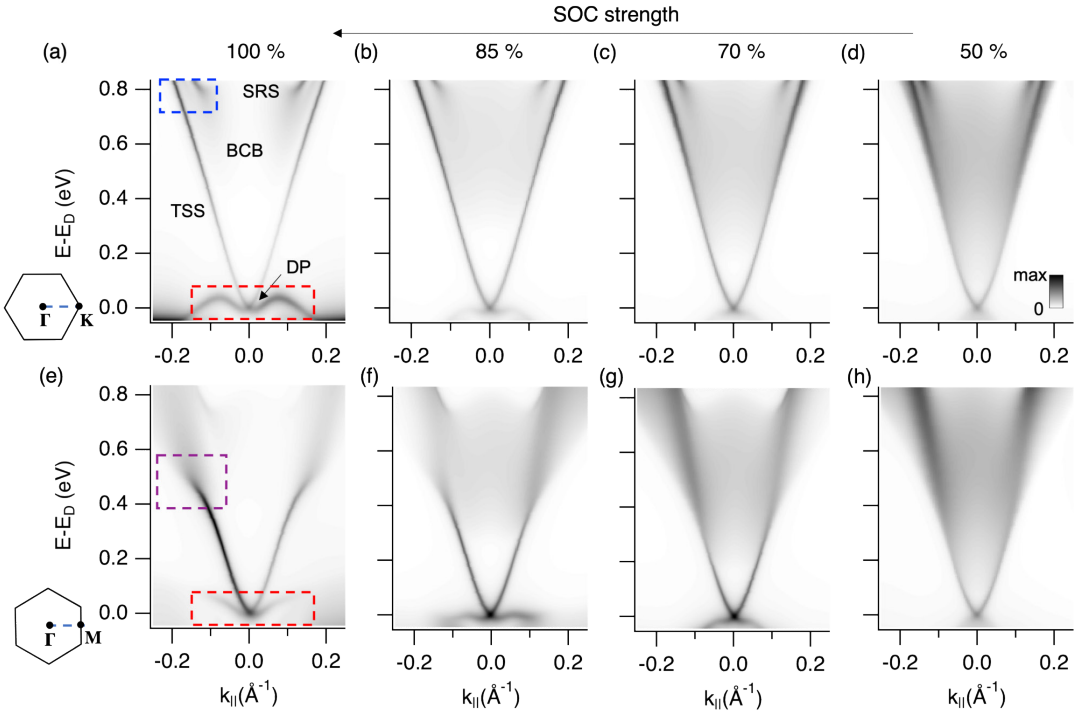

Figure 4.4: (a-d) Calculated E *vs.* k photoemission intensity along the ΓK direction for s-polarized 10.8 eV photons, upon varying the SOC strength. Panel (a) also indicates the relevant features as defined in 4.2(d): TSS, topological surface state; BCB, bulk conduction band; SRS, surface resonance state (highlighted by the dashed blue box); DP, Dirac point (dashed red box). The energy scale is referenced to the Dirac point. (e-h) Same as (a-d), but along the ΓM direction. Boxes in panel (a) highlight the point at which the band strongly bends outwards and severely broadens (violet box) and the Dirac point (red box).

structure. We first observe that the "M" shape of the dispersion below the DP is gradually reduced (panel (b)), until it disappears at 70 % SOC in favor of a monotonic dispersion (panel (c)). The TSS is also broadening, with a width that increases with the distance from the DP. This is particularly striking in panel (d) where the states close to the surface resonance become more intense and broader. Alongside with this, an increase in the BCB is visible as a gradual change in contrast between the area enclosed by the TSS and that outside. The small intensity of the BCB with respect to the TSS is due to the unfavorable matrix element at this photon energy [154]. At 50 % SOC, however, the BCB intensity is strong and visible down to ∼100 meV above the DP. Apart from the conduction band population and the band broadening, however, the dispersion along ΓK undergoes minimal changes, and remains linear above the DP throughout the SOC-dependent evolution. Also the changes in the SRS are minimal.

The dispersion along ΓM is strikingly different from the one along ΓK. Panel (e) shows the dispersion for the full value of the SOC. Similarly to panel (a), also here the TSS below the DP is bending upwards (dashed red box). The dispersion, while being approximately

linear in the energy range between 100 and 300 meV, is strongly bending outwards around 400 meV (dashed violet box). Here the bands start to broaden until they are very diffuse. Also in this case the surface state is visible around ∼800 meV above the DP, although the contrast with respect to the TSS is markedly weaker.

The evolution with decreasing SOC has some similarities with what observed for ΓK. A strong population of the BCB becomes visible inside the two TSS branches. The upward bending of the TSS below the DP decreases and vanishes with decreasing SOC. In the region up to around 400 meV from the DP, the cone is broadening. In the region above, instead, the TSS gains relative intensity and, since at 100 % SOC the TSS is very broad and weak, it becomes more defined at lower SOC values (see panel (h)), in contrast with what observed along the ΓK direction. This also allows clearly distinguishing how the strong band bending observed in panel (a) reduces with decreasing SOC, and almost vanishes at 50 % SOC. Moreover, while the surface resonance is visible for all the other SOC values, in this last panel no intensity appears at ∼800 meV above the DP.

As seen, the variation of the SOC brings intriguing changes in the band structure. Along both directions, the dispersion below the DP undergoes dramatic changes across 85 % SOC. Above the DP, a striking dichotomy is observed in the SOC dependence between the two directions. The dispersion of the TSS along ΓK undergoes negligible changes, apart from the reduction of the bulk bandgap common to both materials. The major change along ΓM is instead the TSS warping, which increases with the SOC and in particular between 85 % and 100 %. We want to stress that it is the downward bending along ΓM that causes the hexagonal warping of CESs, while the dispersion along ΓK remains linear.

4.3 Comparing calculations with experimental results

The SOC-dependent calculations were not performed solely as a telltale of the role of this interaction in defining the band structure of Bi_2Se_3. Such an approach is also rooted in the reported evidence that agreement with the experimental data might be achieved by taking into account a reduced transfer of the SOC interaction from the bulk to the surface, as reported above for examples low-index metal surfaces [156, 159]. Since these studies prove the possibility that the effective SOC strength felt by the surface states of a solid system is smaller than the full atomic value, we benchmark our SOC-dependent calculations with photoemission measurements acquired with the 10.8 eV source in order to estimate the effective SOC strength at the surface of Bi_2Se_3. The occupied band structure is investigated with equilibrium ARPES. The pump-probe capability of the setup allows extending the comparison also to the unoccupied part of the spectrum, where the TSS is closer to the surface resonance and in general the warping is stronger [155]. This joint comparison allows estimating if and to which extent the SOC strength is effectively reduced at the surface, inspecting the effects of its variation on the TSS dispersion in Bi_2Se_3.

4.3.1 Dispersion of the occupied band structure

Figure 4.5 shows the comparison between the experimental and the theoretical dispersions along the two high-symmetry directions ΓK (top row) and ΓM (bottom row). The spectra were measured with *s*-polarized 10.8 eV photons, at a temperature of 110 K, to minimize temperature-induced broadening. In order to compare the experimental results with the *ab initio* calculations, a common energy scale is needed, since in general the Fermi levels in the calculations and in the experiment might not coincide. The only clearly identifiable common feature in the occupied band structure is the DP. The details of the procedure followed to locate the energy of the DP and the Fermi energy are reported in Appendix A. Experimental dispersion and calculations are thus aligned to the DP, and energies are now referenced to the experimental Fermi energy.

In the measured dispersion along ΓK (Fig. 4.5(a)), the DP is located ~ 410 meV below E_F, hence signaling an *n*-doping of the system due to aging. This is advantageous for our investigation since it allows probing a larger part of the band structure with equilibrium ARPES. The dispersion below the DP is monotonic and almost linear. Above the DP, the intensity of the two TSS branches becomes asymmetric. While the branch at negative k values (left branch) is weak and broad, the one at positive k values (right branch) is sharply defined. In between the TSS branches, the 2DEG is visible as a narrow feature at positive k. The presence of the 2DEG confirms the aging of the surface also revealed by the rather low DP position. Also for this feature, the dispersion at negative k is weaker and broader, which makes it hard to distinguish the TSS and the 2DEG. In between the TSS branches, also the population from the BCB should contribute to the photoemission intensity. As commented above, however, the *s* polarization of the probe minimizes the presence of the BCB. In the vicinity of E_F the two 2DEG branches are separated in momentum due to their parabolic dispersion, and the intensity in between can be ascribed to the BCB. The weak intensity in this region proves the small contribution of the BCB.

The blue dashed lines mark the energies at which the momentum distribution cuts

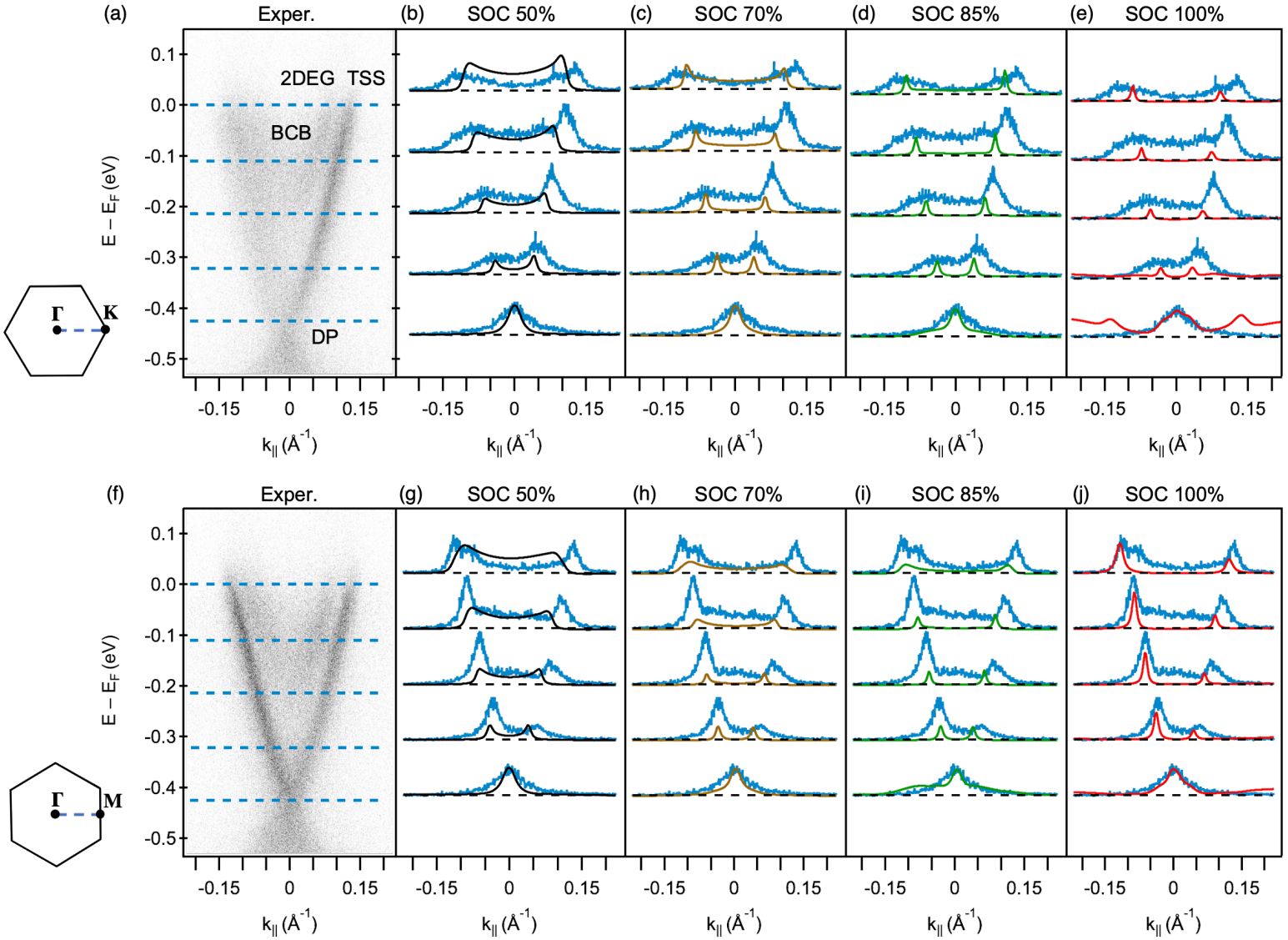

Figure 4.5: (a),(f) Measured band structure along the ΓK and ΓM directions. (b-e),(g,j) MDC cuts extracted from the measurement and from the calculations with increasing SOC strength: (b),(g) 50 %, (c),(h) 70 %, (d),(i) 85 %, (e),(j) 100 %. The cuts are extracted at the DP, at E_F and at three energies in between.

(MDC) have been extracted, *i.e.* at intervals of $\sim$ 100 meV from the DP to E_F and integrated in an energy window of 10 meV. The MDCs are reported in panels (b-e) in light-blue and compared to the MDCs extracted from the calculated maps at variable SOC strength: (b),(g) 50 %, (c),(h) 70 %, (d),(i) 85 %, (e),(j) 100 %.

Comparison of the dispersion in the vicinity of the DP evidences the inadequacy of the full SOC (red MDC) to account for the measured dispersion, where the TSS shows no "M"-like shape: its linearity is instead best reproduced at 50 % SOC (Fig. 4.4(a) and (d)). Above the DP, both the experimental and the theoretical dispersions are slightly parabolic, as discussed above. However, the MDCs show a discrepancy between experiment and calculations. In particular, the calculated MDCs seem to underestimate the cone aperture, hence predicting a higher band velocity than the one actually observed, and the discrepancy increases with the distance from the DP. This can be explained as a shortcoming of the local spin-density approach, as already reported in [157, 159]. For the MDCs $\sim$ 100 meV and $\sim$ 200 meV below E_F, the 50 % SOC seems to give a better agreement, due to the higher population of the BCB with respect to the other SOC values. The intensity measured in this region, however, is more correctly attributable to the 2DEG, since its two branches get close and due to their broadening they partially merge. Overall, the measured relative intensity between the left and right branch of the TSS is well reproduced by all the SOC values, demonstrating that the spectroscopic calculations correctly account for the matrix element effects in our experimental geometry.

Panel (f) shows the measured dispersion for the ΓM direction. The intensity distribution is more symmetric than in panel (a), both for the TSS and for the 2DEG. The prevalence of the 2DEG on the BCB inside the TSS is analogous to what observed along the other direction. Below the DP the dispersion is very close to linearity, and better reproduced at low values of the SOC. Along this direction also the dispersion in the vicinity of the DP for a SOC of 85 % is evidently inadequate, since the bands are bending upwards (see the bump in the MDC at $k \simeq -1\,\text{Å}^{-1}$). This rules out a SOC value as high as 85 %. Upon approaching the Fermi level, the difference among the theoretical dispersions becomes more evident. Due to the same overestimation of the band velocity commented above, the 100 % SOC seems to agree better with the experimental dispersion at the Fermi level, since the effect of the warping is a detectable reduction of the band velocity along ΓM. The experimental dispersion, however, is not reflecting the strong warping experienced by the 100 % SOC case (Fig. 4.4(e)). Also along this direction the BCB contributes with negligible intensity with respect to the 2DEG, as proven in the vicinity of the E_F.

The comparison between measurements and calculations for the occupied part of the spectrum gives interesting hints on the effective value of the SOC in Bi_2Se_3. The 100 % SOC calculation does not satisfactorily reproduce the dispersion deduced from the experiments below the DP, for both directions. Along ΓM, this is true also for the 85 % SOC. In addition, the full SOC predicts at E_F a warping larger than the one observed in the experiment. This brings to the first conclusion that the effective value of the SOC transferred to the TSS is at least as low as 70 % of its full value.

4.3.2 Dispersion of the unoccupied band structure

Since the warping increases with the distance from the DP, access to larger portions of the band structure above E_F is beneficial to compare the experiments and the calculations in an energy interval where the influence of the SOC on the warping is more pronounced. This could be achieved my means of chemical doping, which however adds the complications of dealing with a system whose structure and chemical composition is not identical to the bare compound [165]. While two-photon photoemission is a possibility [166], carriers can efficiently be injected above E_F with an infrared pulse in a pump-probe scheme [17, 148, 155]. Excitation with infrared light pulses populates the unoccupied band structure to a suitable extent to benchmark the warping features revealed by the calculations (Fig. 4.4), which can be distinguished also at moderate energy distance above E_F.

The pump-probe measurements were performed at the fixed time delay of $\sim$1 ps, at which the population in the vicinity of the Fermi level is maximum due to a cascade relaxation mechanism of the charge carriers [77, 167]. We used a p-polarized pump with a fluence of $\sim$150 μJ/cm^2.

Figure 4.6 shows the comparison between measured and calculated photoemission maps following the same arrangement of Figure 4.5. The measured maps are reported as a difference between the pumped map and the equilibrium one, as customary in TR-ARPES measurements to emphasize the change in the electronic population. The measurement along ΓK (panel (a)) shows that the linear dispersion of the TSS is also observed above E_F. The branch at negative k values remains broad and weaker, but the one at positive k values is well distinct from the 2DEG and allows discerning that the latter disperses roughly parallel to the TSS. Accessing the dispersion above E_F is also beneficial for circumventing the unfavorable coincidence of a broad 2DEG and a small BCB contribution to the intensity. As discussed above for the region close to E_F, the parabolic dispersion of the 2DEG causes its branches to be well separated in momentum, hence allowing the attribution of the intensity detected in between to the sole BCB. This is better visible in the MDC cuts taken at $\sim$55 meV and $\sim$110 meV above E_F and shown in subsequent panels. It is clear that the 50 % SOC (b) shows a too high BCB population. The 70 % and 85 % SOC, (c) and (d), are instead closer to the experimental dispersion, while the 100 % SOC in (e) shows no significant BCB intensity.

The measurement along ΓM is shown in panel (f). The right branches of the TSS and of the 2DEG display a larger intensity, which is also reflected in the presence of a red signal up to higher energies. This might be due to a delay-dependent matrix element effect [70], although the depopulation of the TSS below E_F is more symmetric. The right branch clearly shows that the dispersion is deviating from linearity. Incidentally, the 2DEG population drastically decreases from $\sim$100 meV above E_F, at variance with what observed along ΓK. The intensity of BCB population instead follows a behavior similar to the other direction, and is well reproduced for 70 % and 85 % SOC, as proven by the MDCs in panel (h). The magnitude of the warping agrees well with the prediction of the 85 % and even 100 % SOC. Since for lower SOC values the TSS is severely smearing out at higher energies, also the sharpness of the features is better accounted for at higher SOC values.

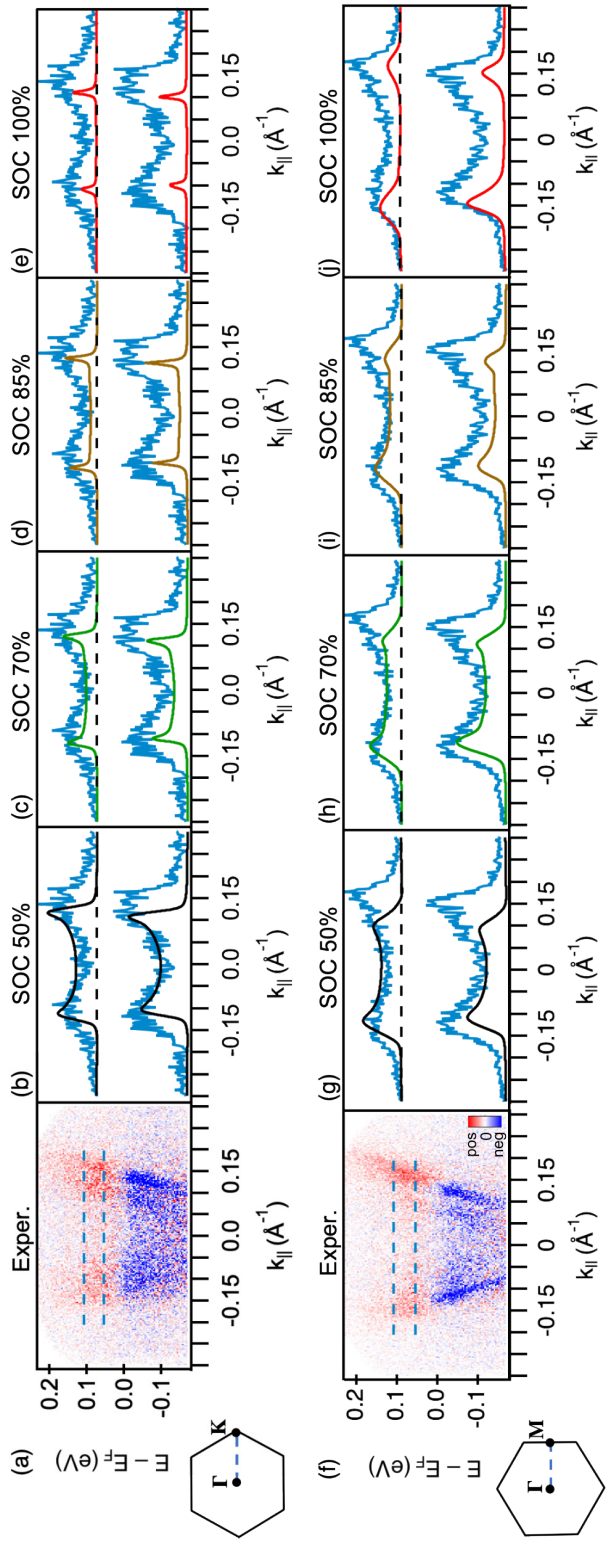

Figure 4.6: Pumped counterpart of Fig. 4.5. Top (bottom) row refers to the ΓK (ΓM) direction. The experimental dispersion is reported in (a) and (g) as a difference map between the one acquired at $\Delta t = 1$ ps and the equilibrium one, to evidence the population of the band structure above E_F. (b-e),(g,j) MDC cuts extracted from the measurement and from the calculations with increasing SOC strength: (b),(g) 50 %, (c),(h) 70 %, (d),(i) 85 %, (e),(j) 100 %. The cuts are extracted 55 meV and 110 meV above E_F.

The inspection of the pumped *E vs. k* maps proves that the intensity from the BCB is small compared to the TSS and 2DEG. It also allowed to confirm that the dispersion along ΓK is linear also above E_F. The dispersion along ΓM instead shows a strong warping that is compatible with the highest values of SOC.

We point out that, in the WAM mode of the hemispherical analyzer, the maximum momentum coverage for a single *E vs. k* at 6 eV is of $\pm 0.17\,\text{Å}^{-1}$ at E_F. The highest part of panel (f) would therefore be at the edge of the analyzer lateral acceptance, hindering a good comparison with the calculations. The 10.8 eV photon energy is thus beneficial to the investigation of this material system in the nonequilibrium régime.

4.3.3 Comparison of constant-energy surfaces

The details of the dispersion viewed as a single *E vs. k* cut are of fundamental importance to understand the role of the SOC in determining the dispersion of the TSS. A more comprehensive picture can be gained by inspecting the full CESs, hence looking at the same phenomenon but from the point of view of how the SOC drives the deformation of the circular CESs into hexagonal and eventually snowflake shapes. At variance with the *E vs. k* analysis, in this case it is easier to visualize the symmetry and the degree of deformation of the CESs, so to evaluate which strength of the SOC is more effective in describing the shape of the experimental CESs.

The CESs were measured by rotating the sample in steps of 0.5° along the tilt axis (perpendicular to the analyzer slit, corresponding to k_y in our axis system for the reciprocal space) and recording an *E vs.* k_x map for each angle. These maps are stacked together to obtain the full 3D map of the $I(E, k_x, k_y)$ photoemission intensity, which can be visualized by slicing it at constant energy.

The result of this procedure is shown in Fig. 4.7(a-e) for the CES measured with *p*-polarized light. The cuts are taken at five energies: at the DP, between the DP and E_F, at E_F, and at the two energies above E_F already considered in Fig.4.6. The TSS contour at the DP (panel (a)) is circular as expected from the vertex of a cone broadened by the experimental resolution. No intensity is detected outside this circular area, apart from a sharp line at $k_y \sim 0.12\,\text{Å}^{-1}$. This spurious intensity is probably the result of the probe beam impinging on a bad sample spot during the tilt angle scan. The cut at -210 meV (panel (b)) has a round shape with some larger broadening at negative k_y values, where also the photoemission intensity is larger. The TSS contour at E_F (panel (c)) is also broader at negative k_y. At this energy there is a clear deformation towards a hexagon. The small discontinuity at positive k_y values is likely due to a change in the position of the probe on the sample due to the angular motion of the latter, as witnessed by the strong spurious strike of intensity commented above. The CES at 50 meV above E_F (panel (d)) shows a larger deformation of the TSS, going towards the snowflake-like shape. The case of panel (e) is analogous, with the deformation particularly visible on the right edge of the snowflake at $k_x \sim 0$ and in the top left edge. We also emphasize that the contrast between the TSS and the region inside it confirms that the BCB photoemission intensity is very weak.

We only calculated them at the two intermediate SOC values of 70 % and 85 %, *i.e.*

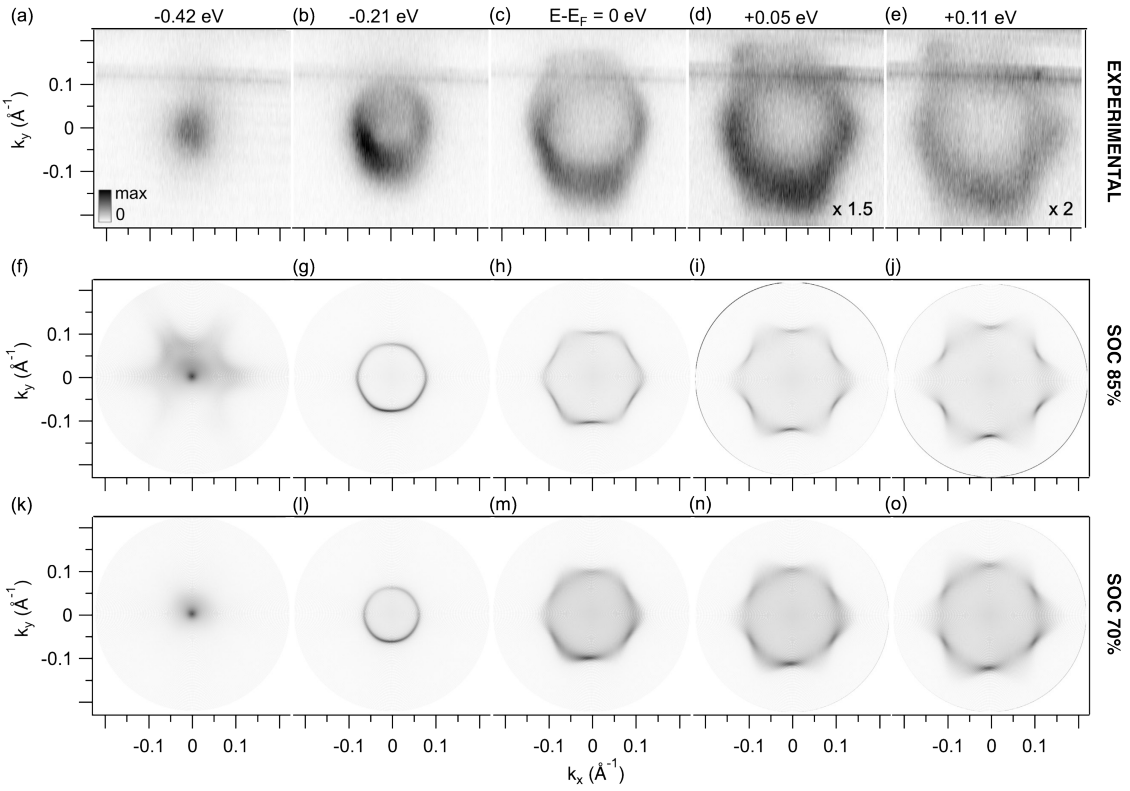

Figure 4.7: (a-e) Experimental CES for the selected values of energy indicated above: (a) at the DP, (b) between the DP and E_F, (c) at E_F, (d) 0.05 meV and (e) 0.11 meV above E_F ($\Delta t = 1$ ps). The intensity of (d) and (e) the last two is multiplied by a factor of 1.5 and 2 for better visibility. (f-j) CESs calculated for 85 % SOC at the same energies. (k-o) CESs calculated for 70 % SOC at the same energies.

those that yield the best agreement with the experimental E *vs.* k data. Panels (f-j) show the 85 % SOC case. The "M" shaped dispersion commented in Fig. 4.5(f),(i) close to the DP here appears as a star-like contour of intensity, in contrast with the experimental observation in (a). Panel (g), showing an already deformed contour, agrees well with the experimental counterpart of panel (b), notwithstanding the broadening of the latter. The following CESs (h-j) also show a good agreement with the experiment, also evidenced by the correct accounting of the intensity asymmetries. In fact, the most intense regions of the hexagon are towards negative k_y values.

A better agreement is found for 70 % SOC (k-o). The DP (k) is properly reproduced as a small circular area. The CES at -210 meV shown in (l) is still circular, in partial disagreement with the measurement in (b), and becomes hexagonal only at E_F (m). Another drawback of this SOC value is that the warping is less severe, and thus the size of the contours above E_F (n-o) are slightly smaller than what actually measured. Also at this SOC the intensity asymmetry is reproduced, being the CES more intense in the negative k_y portion. We stress the fact that for both SOC values, the snowflake deformation above E_F comes along with an intense smearing of the TSS, as already commented for

Fig. 4.6(m), with the result that the tips of the snowflake along ΓM are almost vanishing.

The comparison between the measured and the calculated CESs gives indications in agreement with what found from the analysis of the *E vs. k* maps. The shape of the CES close to the DP suggests a SOC value lower that 85 %. On the other hand, the hexagonal deformation of the 70 % SOC occurs closer to E_F than the experiment suggests, and the size of the CES contour above E_F is smaller, pointing to a value of the SOC closer to 85 %. The CESs also further prove that the calculations correctly account for matrix element effects.

4.4 Conclusions

This study proves that changing the SOC strength in Bi_2Se_3 brings intriguing changes in the band structure and offers hints on the role of this interaction in shaping the dispersion of the surface states.

Along both ΓK and ΓM, the dispersion below the DP undergoes dramatic changes across 85 % SOC, passing from an "M"-shaped to a quasi-linear dispersion. Above the DP, the dependence on the SOC shows a striking dichotomy between the two directions, apart from the change of the bulk bandgap that is common to both. The shape of the TSS dispersion along ΓK undergoes negligible changes, remaining linear at all energies. Along ΓM, instead, the TSS warping increases dramatically with the SOC and in particular between 85 % and 100 %. We stress that the hexagonal deformation of the CESs is due to a band bending along ΓM. This is also the direction along which the SOC has the largest effect on the dispersion, bending it downwards close to E_F. This points to the conclusion that the warping of the TSS closely depends on the SOC strength, and in particular on its effect along ΓM. That the warping depends on the SOC strength also agrees with the results of the $\mathbf{k} \cdot \mathbf{p}$ model, which draws this conclusion from a semi-empirical approach.

Regarding the TSS warping, our SOC-dependent results are in contrast with the proposal that its cause is the level repulsion between the TSS and the BCB [143]. Instead, in our calculations the warping increases with the SOC, where the BCB population is smaller. The opposite trend of the BCB population and the TSS warping with the SOC proves that the former cannot be the origin of the latter. Nonetheless, there must be a mechanism that transfers the symmetry of the bulk states to the surface states, hence reflecting the anisotropy of the bulk states among ΓK and ΓM and endowing the TSS with hexagonal symmetry. We thereby confirm that this happens *via* hybridization of the TSS with the SRS, that in fact undergoes small changes in our SOC-dependent calculations. As already suggested in [148], the variation of the SOC changes the dispersion and thus the interaction between the TSS and the SRS, modifying in turn the TSS dispersion.

The comparison of the calculated photoemission maps with our 10.8 eV data confirms by experiment that the SOC transferred to the surface states in Bi_2Se_3 is reduced from the full atomic value that determines the bulk band structure.

The 100 % SOC is clearly incompatible with the measured dispersion below the DP, where the surface state acquires an "M"-shaped dispersion reminiscent of what is observed in Bi_2Te_3, but contrasting with the monotonic dispersion actually measured in Bi_2Se_3. The warping predicted by the 100 % SOC is also too strong to fit the measured dispersion close to E_F along ΓM. This conclusively points to a reduction of the SOC at the surface. The inspection of the unoccupied part of the spectrum, both in the E *vs.* k maps and in the CESs, reveals that the warping is actually strong in the immediate vicinity of E_F, and thus the SOC cannot be less than 70 % and is likely closer to 85 %. The small discrepancy of this SOC value with the experimental dispersion below the DP might be due to many-body effects not fully taken into account in our approach. Recent works [156, 157] show that suitable many-body corrections can reduce the deformation close to the DP. We also stress that the inspection of the dispersion above E_F benefits form the 10.8 eV photon energy: the TSS branches disperse away, and at smaller photon energies the separation

among the two far above the DP makes it impossible to visualize them both in a single measurement, given the typical $\pm 15^\circ$ angular aperture of hemispherical analyzers [77].

Taken together, these evidences show that the SOC has a strong influence on the dispersion of the TSS in Bi_2Se_3, in particular shaping the warping of the CESs by modifying the dispersion along ΓM. However, the SOC of the heavy element Bi is transferred to the surface of Bi_2Se_3 for only the 80 % of its full value. This number is an estimate that takes into account the dispersion around the DP, that suggests a SOC not larger than 70 %, and close to E_F (above and below), that suggests a SOC of around 85 %. This small discrepancy between the two values might be due to an underestimation of many-body effects.

Chapter 5

Photoinduced flat band dynamics in the kagome metal CoSn

Kagome systems have recently attracted increasing attention owing to their capability of simultaneously hosting a variety of exotic phases of both correlated and topological nature [168–172]. Examples include high-temperature superconductivity [173–175], charge-density waves [176–178], Bose-Einstein condensation [179] and anomalous Hall effect [180–182]. Several types of magnetic ordering have also been observed in coexistence with one or more of these phenomena [183–185].

An intriguing feature in the band structure of kagome systems are flat bands, that originate due to electron localization in real space. Charge confinement derives from the peculiar geometry of the kagome lattice, that hinders hopping at nearest-neighbor sites by the destructive interference of the wavefunctions [186]. Since the localization is of electronic origin, it is reasonable to expect that an ultrafast perturbation of the electronic subsystem will affect the localization, and in turn the band structure. We therefore performed TR-ARPES measurements on the kagome metal CoSn, which is the first kagome system where the flat bands extend over the whole Brillouin zone and below E_F [46, 187], to unveil the response of the electron localization to photoexcitation through the inspection of the transient modifications of the flat bands.

5.1 Basic properties of kagome compounds

The arrangement of atoms in a kagome system is shown in Fig. 5.1(a) [188]. An exact solution of the electronic problem on such a lattice is one where the wavefunctions at nearest neighbor sites have opposite sign (red and cyan circles) [185]. This causes the hopping pathways to nearest neighbors to vanish (red and cyan arrow pointing to the white circle). As a result of this destructive quantum interference effect, the charge will be confined inside the hexagonal region marked in violet. The mobility of electrons is thus reduced, which leads to the appearance of dispersionless (*i.e.* flat) bands in reciprocal space [189].

In addition to the flat bands, the kagome lattice hosts pair of Dirac bands (panel (b)). If also a strong SOC is present, a gap opens at the touching point between the Dirac and

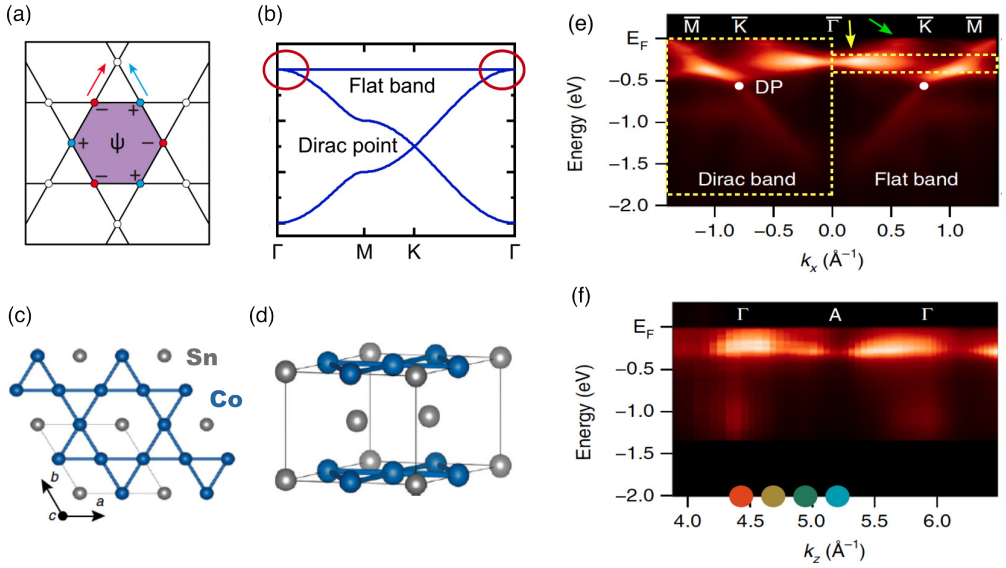

Figure 5.1: (a) Schematic illustration of charge confinement by destructive quantum interference in a kagome lattice. Minus (red) and plus (cyan) indicate the wavefunction relative phase [188]. (b) Scheme of the kagome-derived bands in a model kagome system. Red circles indicate the touching point where the SOC-gap can opens [192]. (c) Structure of a kagome layer of CoSn. The Co atoms form a lattice of corner-sharing triangles, and the hexagonal holes are filled with Sn atoms. (d) Side view of the structure of CoSn. The kagome planes are intercalated with Sn planes. (e) Band dispersion measured with s-polarized 92 eV photons along the $\Gamma - \mathrm{K} - \mathrm{M}$ path. The Dirac points occur at the K point (white dots), where the signal of the flat bands becomes fainter. The upper and lower flat bands are highlighted by a green and a yellow arrow respectively. (f) k_z dispersion of the flat band obtained by varying the photon energy; orange, yellow, green and cyan dots correspond to 70, 78, 87 and 97 eV respectively. Panels (c-f) are adapted from [46].

the flat bands [169, 190], marked with red circles in the figure. This endows the flat bands with nontrivial topological character [191].

Realization of flat bands extending over the whole Brillouin zone is challenging due to the presence of additional effects that can spoil the physics of the ideal case [193]. In real systems, even for perfect nearest-neighbor destructive interference, the effect of next-nearest neighbor hopping can contribute in delocalizing the electrons [171]. In addition, the pure two-dimensional properties of the Dirac bands are not guaranteed when, instead of a single layer, a layered 3D system is considered, and finite interlayer coupling must be taken into account. As a result, systems can lack quasi-2D behavior [184], or display bands which remain flat only for subregions of the Brillouin zone [183].

Quasi-2D kagome metals can be realized, among the existing families, by decoupling single kagome layers of the type ASn (A = Mn, Fe, Co) with intercalated layers of Sn [188, 192]. The states involved in the kagome-induced destructive interference in these cases are the 3d orbitals of the transition metal. In addition to bringing magnetism and SOC into play, with the d bands the kagome geometry is enhancing the effect of correlations

which are already intrinsically strong. FeSn is magnetically ordered [188] and hosts two Dirac bands in the vicinity of the Fermi level, originating from the in-plane 3*d* orbital components [168]. However, the corresponding flat band of the same orbital character lies above the Fermi level, and thus is not accessible to equilibrium ARPES.

Substitution of Fe with Co, while suppressing the magnetic ordering due to higher *d* orbital filling, shifts the Fermi energy well above the flat band [194]. In this way, in CoSn all the kagome-derived features lie below the Fermi level and can be studied by equilibrium techniques [46]. Figure 5.1(e) shows the dispersion of CoSn as measured with 92 eV photons. Two flat bands are visible, marked by a green and a yellow arrow. These originate from the different degrees of freedom of the 3*d* orbital: the upper flat band comes from in-plane components (d_{xy}, $d_{x^2-y^2}$, green) and the lower flat band from out-of-plane components (d_{xz}, d_{yz}, yellow). The two appear as a single feature close to Γ. At larger k values, the bandwidth increases and the two flat bands disperse away from each other. This is due to the effect of next-nearest-neighbor hopping, typical of realistic kagome systems, that causes the flat bands to acquire a finite dispersion close to the K point [171]. The intensity of the lower flat band drops off around $k_{||} \simeq 0.5\,\text{Å}^{-1}$, possibly due to the increased dispersion of the two bands.

Tuning the photon energy demonstrates that the flat band has a small dispersion also along k_z (Fig. 5.1 f), although in this case due to the quasi-2D nature of the CoSn kagome layers rather than to geometric frustration. CoSn is hence the first kagome compound to realize the coexistence of Dirac states and topological flat bands in the whole Brillouin zone and in the low vicinity of the Fermi level.

An interesting question regards the stability of the electronic localization mechanism upon external perturbations. Calculations predict that an increase in temperature also up to 1000 K has little effect on the band dispersion [195]. Time-resolved optical and photoemission spectroscopy has been applied to study the kagome metal CsV_3Sb_5, where the pump pulse induces a nonthermal melting of its unconventional charge-density wave phase [196, 197]. At present, however, no report discusses the robustness of the electron localization upon ultrafast photoexcitation. Since it is of electronic origin, it is reasonable to expect that the localization is altered if the electronic subsystem is perturbed by excitation with a laser pulse. Since the flat bands encode direct information on the effectiveness of localization, they offer a suitable access point to monitor its response to photoexcitation.

To perform this study, CoSn is the ideally suited material, since the flat bands lie below the Fermi level and extend in the whole Brillouin zone, and can be monitored by photoemission during the whole excitation and relaxation dynamics. We thus performed TR-ARPES measurements on CoSn to detect the response of flat bands to photoexcitation and deduce that of the electronic localization.

5.2 Sample preparation

Details on the sample fabrication can be found in [168]. Samples grow as thin posts (Fig. 5.2(a)) extending for several mm along the *c* axis but with lateral size of at most

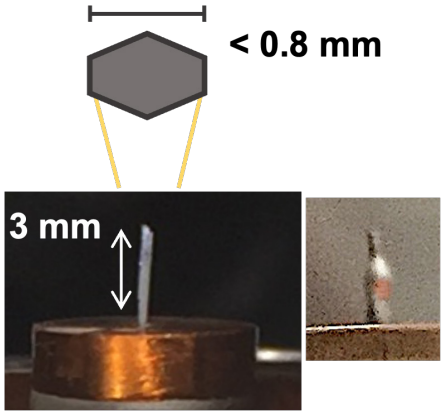

Figure 5.2: (a) Lateral view of a thin CoSn sample glued on the sample mount. The sketch above indicates the hexagonal section of the sample. (b) Thicker but shorter CoSn elongated with a Cu post glued on top of it, as described in the main text, to fracture the sample as far as possible from the holder surface and the glue.

800 μm. They are thus cleaved in ultrahigh vacuum by fracturing them in order to expose a fresh surface parallel to the *a*-*b* plane. Smaller lateral size tends to produce better exposed surfaces, but the thinnest samples are less suited for a photoemission experiment. Especially at the low electron kinetic energy at which measurements are performed, as compared to synchrotron-based photoemission, proximity to the sample edges can lead to severe distortions or even disruption of the energy-momentum distribution, due to the fringing fields generated by the discontinuity of the edge. This effect is more severe for electrons of low kinetic energies, and thus the 10.8 eV photon energy is essential to limit this effect and allow the measurement of the band structure by photoemission. Additionally, if the pump fluence is sufficiently high, edge effects can enhance multi-photon processes producing photoelectrons due to the pump beam alone.

It is hence desirable to have crystals with the largest possible lateral size. On the other hand, if the sample is thicker, the cleaving fracture tends to happen at the basis of the sample, hence exposing the surrounding glue to the laser beams. Using a suitably thin post solidly glued on top of the sample (Fig. 5.2(b)) would increase the probability for the sample to fracture farther from the basement, ideally close to the sample-glue-post interface. We emulated the post-cleaving technique by adding a glue capping on top of the sample, depositing small amounts of it at a time to get an elongated shape. The assembly (the sample placed on the sample holder and with the capping on top) is then baked at 100 K for the glue to harden and become conductive.

CoSn samples display as hexagonal section, which can be related to the microscopic structure and used to pre-orient the samples outside the experimental chamber. The uncertainty of such procedure, performed under the optical microscope, is estimated to be of the order of 5°.

5.3 Dispersion of the flat bands

We compare the DFT calculations of the CoSn band structure already reported in [46] (Fig. 5.3(a),(c)) with our measurements at 10.8 eV both along the ΓK and the ΓM directions around Γ(Fig. 5.3(b),(d)). The former was measured at 120 K and the latter at room temperature. Using the estimate of ∼5.5 eV for the inner potential of CoSn [168] with 10.8 eV photons we are measuring at $k_z \simeq 1.77\,\text{Å}^{-1}$. The Dirac and the flat band have however been proven to have small dispersion also along k_z, and hence a comparison with the calculated band structure at $k_z = 0$ is reasonable.

In the ΓK direction, a broad feature with no dispersion is visible, with a width of ∼200 meV. In the ΓM direction the only difference is the width of the feature, presumably due to temperature effects, since the calculated dispersions are identical apart from a small difference in the flat band (Fig. 5.3(a),(c)). In both cases, the width of the observed feature is sufficiently large to comprise both the flat bands and the non-kagome-derived band. However, no spectral intensity is detected where the DFT calculations predict the upper Dirac band to strongly disperse away from the flat feature, at $\sim \pm 0.2\text{Å}^{-1}$.

We further investigated the behavior of the bands at larger k values in the ΓK direction, by inspection of the calculated band structure (Fig. 5.3 (e)) and of the ARPES measurements with s and p polarization (Fig. 5.3 (f),(g)). In the p polarization, the band starts fading away around $0.3\,\text{Å}^{-1}$. In the s polarization instead the intensity slightly drops only at $k_{||} \simeq 0.5\,\text{Å}^{-1}$, in agreement with the corresponding synchrotron measurement of Fig. 5.1(e). This is the origin of the linear dichroism observed when the difference among the maps acquired with two polarizations is taken (Fig. 5.3(h)). As commented above, we tentatively ascribe this effect to the increasing dispersion of the two flat bands. The main feature bends towards higher binding energies at larger $k_{||}$ values. To better ascertain this, we extracted two EDC curves on the two momentum separated by the zero-crossing of the signal in Fig. 5.3(h). We fit these curves with Lorentzian peaks multiplied by a Fermi-Dirac distribution and convoluted with a Gaussian accounting for the experimental resolution. The peak position of the brown and green EDC curves in (f), although integrated on a wide momentum region, differ by ∼ 21 meV. In addition, while the brown curve can be fit with a single peak (A), to fit the green curve one needs an additional peak (B) located ∼ 0.24 eV above the main one, in good agreement with the separation between upper and lower flat bands predicted by the calculations in this momentum region. Regarding the lower Dirac band and the non-kagome-derived band, the same arguments apply as in the case of the upper Dirac band: where the calculations would predict a strong band bending away from the flat features, no intensity is detected, presumably due to matrix element effects. The 10.8 eV photon energy is thus beneficial to selectively probe only the flat bands in CoSn.

Taken together, these evidences concordantly point towards attributing the main feature to the lower flat band, and the second one to the upper flat band. At smaller momentum values, the vicinity of the two results in a single broad feature, in agreement with the measurement in Fig. 5.1(f). On the other hand, we can rule out the Dirac band and the non-kagome-derived band as possible origins of the photoemission signal in this momentum region.

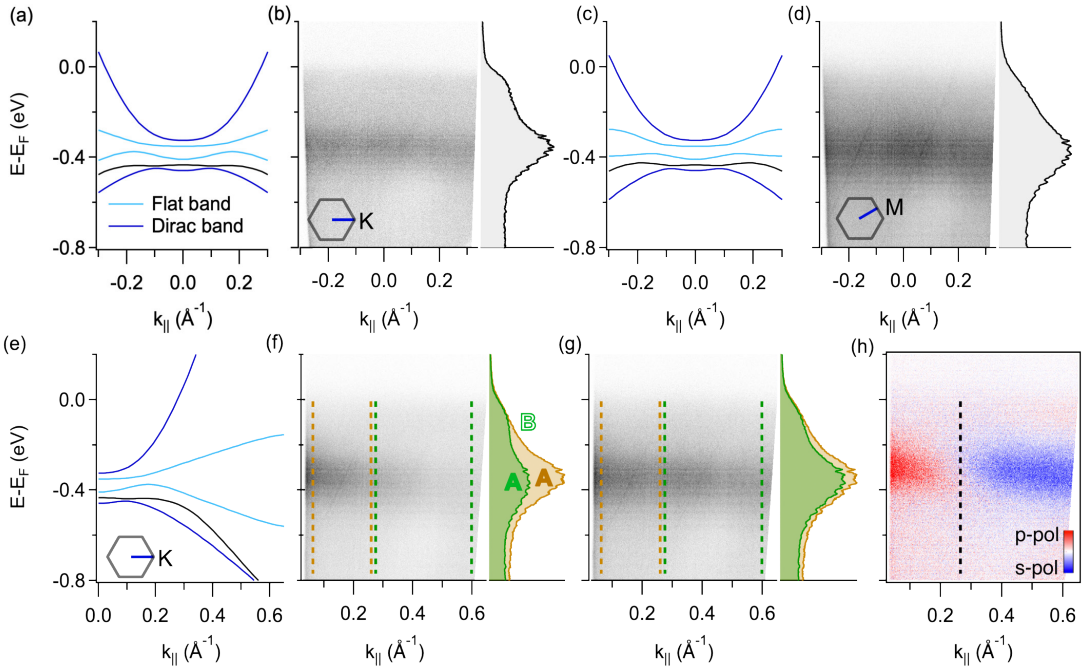

Figure 5.3: (a), (b) Dispersion along ΓK calculated with relativistic DFT and measured with 10.8 eV photon energy at 120 K. The color code in (a) identifies the kagome structures, and the non-kagome derived band is depicted in black. (c), (d) Dispersion along ΓM calculated with relativistic DFT and measured with 10.8 eV photon energy at room temperature. (e) Calculated dispersion along ΓK and closer to the K point. (f), (g) Dispersion measured at room temperature close to the K point, with *p*- and *s*- polarized probe respectively. A and B designate the lower and upper flat bands, respectively. (h) Difference between (f) and (g) with the dotted line marking the zero-crossing of the dichroic signal integrated on the whole flat feature.

5.4 Photoinduced dynamics of the flat bands

Pump-probe measurements were performed along the ΓK direction at base temperature of 115 K and a fluence of 260 μJ/cm^2. The momentum region covered by the measurement is away from Γ for two reasons. As seen, the dispersion of flat bands increases towards the K point, which facilitates to disentangle them and, in the time-resolved measurements, to detect possible differences in their dynamics. The off-normal geometry is also advantageous to minimize spurious counts coming from multi-photon photoemission by the pump enhanced at the sample edges. In our experimental geometry (Fig. 3.3) the pump beam impinges on the sample surface at an angle of 30°. This increases the lateral size of the spot and renders the task of avoiding sample edges more delicate. For this reason, we were not able to perform a proper pump-probe measurement at normal emission. On the other hand, upon approaching normal incidence, the spurious counts from the pump are minimized and the TR-ARPES experiment can be performed.

Fig. 5.4(a) shows the effect of photoexcitation on the flat bands of CoSn. The behavior of the flat bands is of particular relevance, as it displays both an increase and a decrease

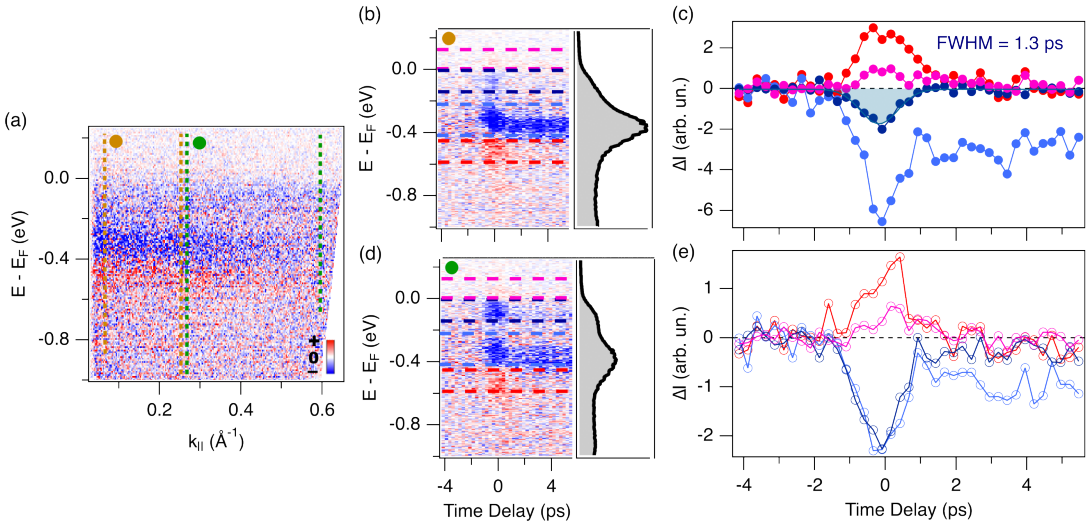

Figure 5.4: (a) Difference plot between the spectrum pumped at zero time delay and the average of the unpumped ones. (b), (c) Differential EDC curves plotted as a function of time delay. (c), (e) Time dependence of the photoemission intensity in different energy ranges of the spectrum, according to the color code of the horizontal dashed lines. The grey-filled cyan trace in (c) is the gaussian fit to the dark blue trace yielding the indicated FWHM.

in intensity as a function of energy, signaling a displacement or a broadening. A negative signal is also found below the Fermi level, along with a weak positive counterpart above. We thus extracted differential EDC (dEDC) curves integrated in the regions marked by the colored dashed lines in panel (a). In panels (b) and (d) they are displayed as a function of the time delay, while panels (c) and (e) show the corresponding intensity dynamics extracted at the flat band positions, below the lower flat band, and immediately above E_F. At small k values (panel (b)) the most intense changes are observed on the lower flat band; a small negative signal is also detected close to E_F. At large momentum values (panel (d)) a strong modification is also observed closer to the Fermi level, corresponding to the feature previously identified with the upper flat band.

The positive signals (red and purple traces in (c) and (e)) last for the duration of a cross correlation in (e) and slightly more in (c). The negative signal on the lower flat band, instead, has a different behavior in both momentum regions. Close to zero time delay the signal is large, and after the cross correlation time it goes to a smaller value, which seems stable in the time window of our measurement. Interestingly, the upper flat band in the right momentum region has a similar behavior. Comparing the two blue traces in Fig. 5.4(e), we can further observe that the maximum of the two signals is comparable, and at later time delays the dark-blue curve is smaller in absolute value. This does not happen in (c), where the duration of the signal in the dark-blue region is limited by the resolution and can be well fit by a gaussian of FWHM $\simeq 1.3$ ps, in agreement with the value reported in Sec. 3.1.5.

In order to identify the nature of the out-of-equilibrium changes in the spectra and

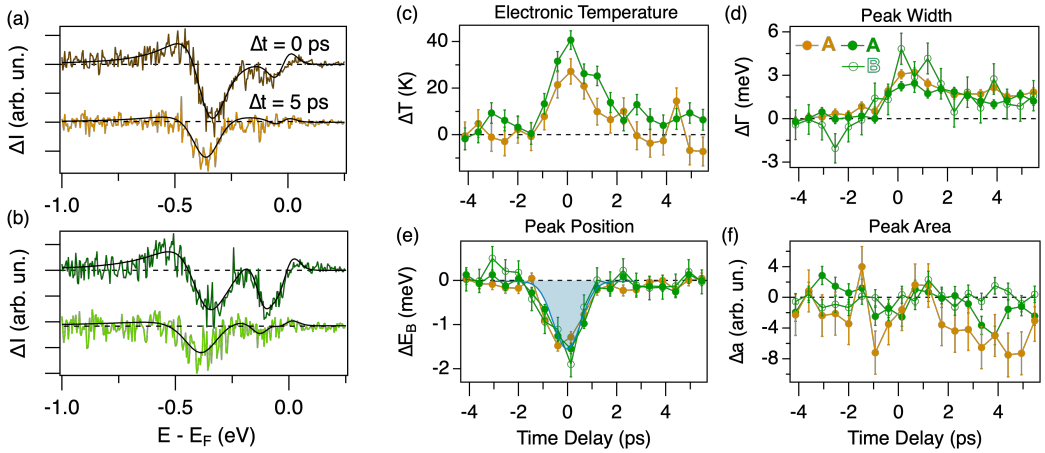

Figure 5.5: (a), (b) dEDCs taken at 0 ps and 5 ps delay in the two momentum regions of corresponding color. The best fit is plotted as a solid black line. (c)-(f) Variation with respect to equilibrium of the parameters extracted by fitting the dEDCs, as a function of time delay. The colors correspond to the code used so far. Bars indicate the uncertainty of the fitting procedure on the parameters. (c) Electronic temperature in the two momentum regions. (d) Lorentzian width of peak A (brown and green) and B (green, empty markers). (e) Position (binding energy) of the peaks. The solid cyan-filled line is the cross-correlation reported from Fig. 5.4(c). (f) Area under each Lorentzian peak.

shed more light on the differences pinpointed above, we fitted each EDC curve of time delay series. The model function of the fit is the one described above also for the out-of-equilibrium EDCs, namely a sum of Lorentzian peaks, convoluted with a Gaussian accounting for the experimental resolution and multiplied by the Fermi-Dirac distribution. As the photoinduced changes in the spectrum are very small (less than 0.4 %), it is convenient to visualize the results of the fitting procedure directly on the dEDCs. Just as the dEDCs are obtained by subtraction between the EDC and the equilibrium EDC, taken as average of the unpumped ones, the differential model is the difference between the fit function and the best fit of the equilibrium EDC. Four representative dEDCs are reported in Fig. 5.5(a),(b), with the color code indicating the momentum region they refer to. The dark-colored traces are taken at $\Delta t = 0$ ps, while the light-colored ones are taken at $\Delta t = 5$ ps, where the changes in the spectrum have become stationary. As visible in the upper trace of panel (a), the effect of photoexcitation is strong at time zero both in correspondence of the main band and in the vicinity of the Fermi level. This last effect is accounted for in the fit by a thermal broadening of the Fermi-Dirac distribution. At later time delays, a negative signal is detected only close to the lower flat band, as also expected from the traces in Fig. 5.4(c). The results are different for the traces of panel (b), extracted at large k values. Here the signal from upper flat band contributes both at time zero (upper trace) and at later time delays (lower trace), where it determines a small negative signal close to E_F. Also this observation is in agreement with the evidences from Fig. 5.4(e).

The variation with respect to equilibrium of the parameters of best fit are plotted

as a function of time delay in Fig. 5.5(c-f). The first important observation is that the parameters of the two A peaks and the B peak display almost identical dynamics, compatibly with the common origin from the $3d$ orbitals of Co. As expected from the previous observations, all the parameters, except for the peak area, display a larger change at time zero. The observed spectral changes are thus the result of an increase in the electronic temperature, along with a sudden shift and broadening of the flat features. which explain the observation of an increase in photoemission intensity at -0.5 eV below the Fermi level in Fig. 5.4. The relaxation dynamics after excitation are similar among the peaks, while qualitatively different among the fitting parameters. The electronic temperature for both regions relaxes on a timescale longer than one cross-correlation. The width of the flat features instead sets to a plateau of ~ 2 meV, $\sim 1\%$ higher than equilibrium, lasting longer than 5 ps. Finally, the peak position relaxation agrees with a gaussian of width comparable to the experimental cross-correlation (cyan line in (c)). This indicates that the observation of the dynamics of the photoinduced shift is limited by our experimental resolution. The peak areas, instead, show no clear dynamics across time zero, signaling that charge redistribution from or to the flat band is negligible. These observations point towards the broadening of the flat bands as the origin of the long-lasting nonequilibrium signal visible in Fig. 5.4(c),(d).

We interpret our results starting from the idea that the ultrafast pump pulse induces an electron delocalization, hence affecting the effect of electronic correlations on the flat band dispersion. Both on the short and on the long timescales, the energy injected by the pump pulse causes the electronic temperature to rise, which is indicative of an increased kinetic energy of the charge carriers. As discussed in Sec. 2.1, a change in the correlations experienced by the electrons can in principle modify the position and lifetime of the bands. In more detail, it is not the sole strength of the electronic correlations that determines their effect on the system properties, but also their ratio with respect to the electron kinetic energy [46]. The shift and broadening of the flat bands can thus be viewed as the result of a decrease of the weight of electronic correlations effects in determining the band structure with respect to the kinetic energy counterpart. Photoexcitation at 1.2 eV does not alter the population change of the flat bands, rather it induces a change in dispersion toward a less flat condition, due to an increased mobility of the charge carriers. However, since we integrate the dispersion on a wide momentum region, an increase in the dispersion appears as a broadening.

The changes in the lineshapes are not only larger at time zero than at later delays, but also qualitatively different. We conclude that the presence of the pump induces a disruption of the electron localization affecting both the position and the width of the bands. This stronger renormalization has a lifetime shorter than our cross correlation and vanishes as soon as the pump leaves the sample, signaling the recovery of the electronic localization. The case is different for the later time delays, where only a small broadening survives. Complete recovery can be hindered by some bottleneck effect that slows down the recovery of electronic temperature and preserves the itinerancy of a smaller fraction of charges. The residual fraction of delocalized electrons must be smaller than at equilibrium since it is sufficient to induce a band broadening but not a shift. We note that the order of magnitude of the long-lasting broadening is compatible with a thermal origin due to

the increase of the lattice temperature by a few K with respect to the equilibrium. That the broadening at time zero is not entirely of the same origin is instead suggested by the concomitant shift in binding energy. Overall, the small entity of lineshape changes in the flat bands suggests that the localization mechanism induced by the kagome geometry is robust upon infrared photoexcitation.

5.5 Conclusions

This investigation has provided access to the ultrafast dynamics of flat bands in a kagome system, that encode information on the response of electron localization to infrared photoexcitation.

The small lateral size of CoSn crystals renders the 10.8 eV photon energy essential to minimize the effects of fringing fields at the edges and to allow the photoemission experiment. More importantly, access to large k values allows exploring a region of the Brillouin zone where the two flat bands acquire a dispersion that separates them in energy. Thanks to this, they can be distinguished and fit separately. The equilibrium measurements also show that the 10.8 eV photon energy has favorable matrix elements for selecting the sole flat bands.

The time-resolved measurements show that the flat bands of CoSn undergo a small but detectable modification upon photoexcitation. We ascribe these effects to electron delocalization induced by the pump pulse, which reduces the effect of electron-electron interaction and renormalizes the flat bands. The majority of charges is relocalized within one picosecond, while a broadening of the flat bands lasts more than 5 ps, signaling either a partial persistent delocalization or an elevated lattice temperature. The small extent of both effects suggests that the flat bands are robust against infrared photoexcitation. More generally, this investigation calls for a deeper understanding of the response of a system in which electronic correlations are enhanced by localization, and paves the way for further exploration of nonequilibrium properties of kagome materials by TR-ARPES.

Chapter 6

Antinodal and oxygen dynamics in the cuprate superconductor Bi2212

The investigation of copper-based superconductors, known as *cuprates*, is at the present date an open field in condensed matter physics, despite the extensive experimental and theoretical effort accumulated in almost forty years of research after their discovery[198]. The scientific interest in cuprates only partially stems from the quest for the microscopic mechanism driving the superconducting transition at temperatures exceeding 100 K. The phase diagram of cuprates shows a number of other phases whose origin and reciprocal relation is yet to be fully understood [199, 200]. In particular, owing to the strong momentum anisotropy of the electronic properties of cuprates, the nonequilibrium dynamics at large k values can unveil key details for the understanding of the origin and interplay of different phases, including the superconducting one. For this reason, we explored this possibility employing the novel 10.8 eV source, since this photon energy allows for time-resolved photoemission experiments in the whole Brillouin zone of cuprates (see Sec. 2.1). As we shall see, the source in its present configuration is not perfectly suited for this kind of studies. The dynamics at large k are however closely related to other aspects cuprate physics, in particular to the dynamics of the oxygen states. We thus employed two different setups, namely an HHG source and a free-electron laser, to address the oxygen dynamics in Bi2212 in the valence band and in the core levels, respectively. This fact makes this study a particular case among those presented in the previous chapters, since we investigated complementary aspects of its properties benefiting from three of the four sources for time-resolved photoemission presented in Ch. 3.

6.1 Towards the antinodal dynamics

6.1.1 The node-antinode dichotomy in cuprates

The family of cuprates comprises several types of copper-based compounds capable of displaying superconducting properties [3]. These compounds share a crystal structure composed of several oxide planes stacked along the c axis. The most studied by means of ARPES is the family of bismuth-based compounds, and in particular the bilayer compound

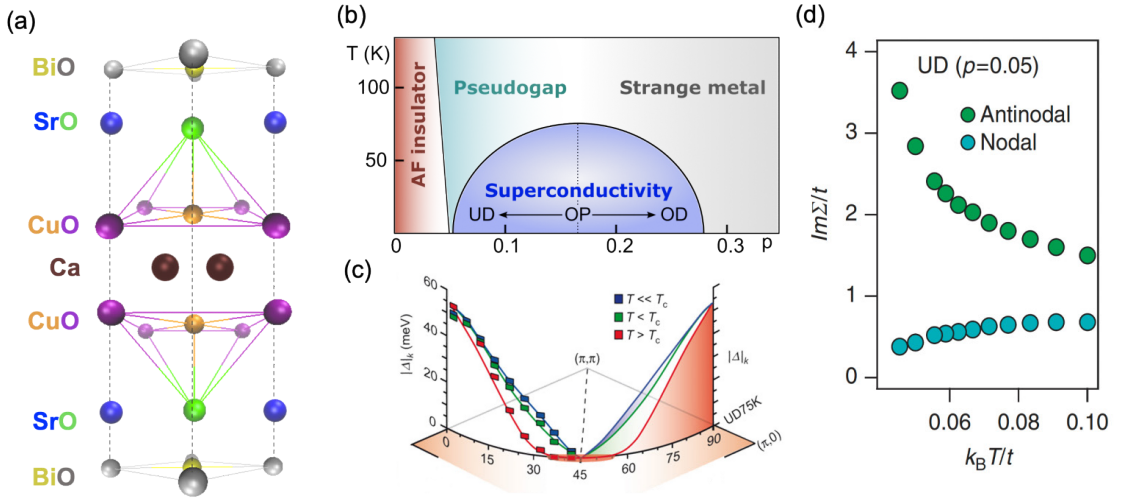

Figure 6.1: (a) Crystal structure of $Bi_2Sr_2CaCu_2O_8$ (Bi2212). Oxygen atoms occupying different planes are indicated with different colors. (b) Phase diagram of Bi2212 as a function of hole doping (p, hole per Cu site) and temperature. The position of optimal doping (OP), where the highest T_C is reached, is marked by a dotted line (p = 0.16) and separates the underdoped (UD) and overdoped (OD) regions. (c) Doping evolution of the *d*-wave gap in the superconducting phase ($T < T_C$, blue and green curves) and in the pseudogap phase ($T > T_C$, red curve) for a slightly underdoped sample [202]. (d) Imaginary part of the self energy, *i.e.* the scattering rate, calculated near the node (blue) and antinode (green) as a function of temperature for a lightly doped sample (p=0.05) [94].

of $Bi_2Sr_2CaCu_2O_8$, because of the good quality of the exposed surface upon cleaving [201]. This is also the sample we investigated.

Figure 6.1(a) shows a schematic crystal structure of $Bi_2Sr_2CaCu_2O_8$ (Bi2212). Along with the other oxide planes, it features two copper-oxygen planes per unit cell [203]. The unit cells are held together by van-der-Waals forces among the Bi-O planes, which makes it possible to exfoliate the Bi2212 samples along the *c* axis, with Bi-O as an exposed surface [204, 205]. It is universally accepted that the electronic properties of cuprates are determined by the many-body interactions within the Cu-O planes [206]. Cu- and O-derived states are the ones lying closer to E_F, hence they have a major contribution on the low-energy electronic properties of cuprate superconductors. Additional holes are introduced in the Cu-O plane upon variation of the oxygen content in the remaining layers, thus called *charge reservoir* layers, defining the landscape of phases illustrated in the phase diagram of Fig. 6.1(b) [207]. One of the most striking aspects of cuprate physics is that the parent undoped compound is an antiferromagnetic insulator (red area) and becomes conducting upon hole doping [208], in contrast with conventional BCS superconductors that are always metallic [209]. The nature of this doping-induced transition is relevant to the dynamics of the oxygen states and is discussed in detail in Sec. 6.2. The so-called superconducting dome (blue area) has a maximum critical temperature at the optimal doping value of p $\simeq$ 0.16, where p is the fraction of doped holes per Cu site. Upon

increasing the temperature at moderate (under-doped, UD) or optimal (OP) doping values, the superconducting phase evolves into a second gapped phase, called pseudogap. The overdoped side of the phase diagram (OD) is occupied by a strange metal phase, as the Fermi-liquid model fails to correctly predict its properties [210, 211].

One difference between the superconducting and the pseudogap phases is illustrated in the cartoon of Fig. 6.1(c), which shows the dependence of the gap on temperature in one quarter of the Brillouin zone, for a lightly underdoped sample [202]. Below the superconducting transition temperature T_C, the gap is zero at the so called nodal point, and is maximum at the antinodes, bearing a d-wave symmetry. As the temperature is increased close to the transition, little changes are visible. Above T_C, the near-nodal region is gapless, while the region at the antinodes is still gapped, with an amplitude comparable to the superconducting gap.

The mechanism originating the pseudogap is still a subject of debate [212]. Moreover, insight on the origin of both superconductivity and pseudogap can be gained by elucidating their relationship [213]. That superconductivity emerges from the pseudogap upon lowering the temperature opens two possible scenarios. Either the same mechanism that drives the emergence of the pseudogap is also involved in the formation and condensation of the Cooper pairs, thus the pseudogap is a *precursor* of superconductivity, or the interactions that drive the emergence of superconductivity dominate at the expenses of the pseudogap upon lowering the temperature, in which case the pseudogap is a *competitor* of superconductivity.

On the basis of the striking dichotomy between the nodal and the antinodal region, a mechanism based on the k-selective localization of the quasiparticles has been proposed as the origin of the pseudogap [214, 215]. It is schematized in Fig. 6.1(d). Quasiparticles in the nodal region (blue points) behave like charge carriers in a metal, with a scattering rate that increases with the electronic temperature. At variance, quasiparticles at the antinode behave as localized charges, with a scattering rate that diverges at lower temperatures. This is analogous to what happens in a Mott insulator [216], where the system is insulating because of the strong Coulomb repulsion that hinders the mobility of quasiparticles and localizes them on the atomic sites, opening a gap in the spectrum. The pseudogap would thus emerge as a result of the strong correlations felt by the Cu $3d$ electrons, that selectively localize quasiparticles at the antinode. This proposal is supported by calculations that numerically solve the Hubbard model [217] and, on the experimental side, by optical pump-probe measurements [94]. The latter, however, are momentum integrated measurements, hence not capable of directly validate the nature of the node-antinode dichotomy.

Since the distinctive hallmark of metallic and localized excitations is the dependence of the scattering rate on the electronic temperature, pump-probe photoemission is the ideal tool to test the proposed scenario, as it provides the possibility of impulsively increasing the effective electronic temperature and following the recovery to equilibrium. The nonequilibrium behavior of the Mott insulator, with the quasiparticle lifetime increasing with increasing temperature, should be found in the antinodal region. This can be witnessed in a TR-ARPES experiment by monitoring the single-particle lifetime. Moreover, the superconducting phase can be melted above a critical fluence of $\sim 70\,\mu\mathrm{J/cm^2}$, while the pseudogap is about three times more robust in terms of the fluence required to affect the gap [68]. This is critical to study the relation between pseudogap and superconductiv-

ity exploiting a nonequilibrium regime. Their interplay can in fact be studied by optically driving the system out of the superconducting phase, with a pump fluence low enough to grant the survival of the more robust pseudogap phase. The re-emergence of the superconducting condensate will take place in the presence of the pseudogap. Following the recovery of both gaps should help elucidating whether the pseudogap is a precursor of superconductivity or a competitor, in which case the pseudogap should close upon the emergence of the superconducting one. In particular, if the pseudogap exists because of the strong electronic correlations within the Cu $3d$ orbitals, an interesting question to clarify is what is the role of these interactions in the superconducting phase.

Several TR-ARPES studies were carried out on cuprates to explore these possibilities [218, 219][19]. However, the limited momentum range accessible to photoemission with probe photon energy up to 6 eV could not provide information on the antinodal dynamics. The energy resolution required to investigate such effects is rather high, since the superconducting gap in cuprates is of the order of few tens of meV, and thus most HHG setups offer either too coarse energy resolution or too low statistics to satisfactorily map the antinodal dynamics [220]. In this regard, the 10.8 eV photon source is a favorable option since it allows access to large k values with sufficient energy resolution and good statistics for the pump-probe experiment. The remainder of this section presents the results of this investigation.

6.1.2 Mapping the equilibrium Fermi surface of Bi2212

In order to test the capability of the 10.8 eV setup to map the full Brillouin zone of Bi2212, we measured its Fermi surface up to the Brillouin zone boundary (Fig. 6.2). The map was acquired at 110 K, hence in the pseudogap phase, rotating the azimuthal angle of the sample in steps of 0.5° and acquiring an E *vs.* k map for each angle. Since the angular acceptance of the analyzer slit is of 30°, mapping the whole k range from the Γ point to the antinode requires the measurement of two maps at different polar angle, one covering approximately up to $\sim 0.4\,\text{Å}^{-1}$ and the other the outer part. The two are subsequently merged to obtain the complete map shown in Fig. 6.2. The map displays a wealth of different features, which we assign according to the literature [221]. The near-nodal region is marked with a dashed white circle, while the antinodal region with a cyan one. The solid lines indicate the two main bands (named 1 and 2) that cross the Fermi level with $k_F \sim 0.4\,\text{Å}^{-1}$. Two black arrows highlight the presence of a splitting of band 1 away from the node. The main band is actually comprised of a bonding and an antibonding band that arise due to the presence of two Cu-O planes per unit cell [222]. For symmetry reasons the two bands are degenerate along the nodal direction, and are split away from it. This effect is known as bilayer splitting. The dotted line is a shadow band arising from the backfolding of the main structure along the mirror planes of the unit cell, and is well visible at the two extrema of the azimuthal scan. It originates from an incommensurate distortion of the tetragonal crystal structure [201] known as orthorhombic distortion, which is typical of cuprates. The dashed-dotted line is instead an *umklapp* band that arises from a slight lattice mismatch between the Bi-O and Cu-O planes that causes superstructure modulations and hence replicas of the electronic bands. The symmetry of the distortion is such that the *umklapp* bands only appear as replicas of the main band 2.

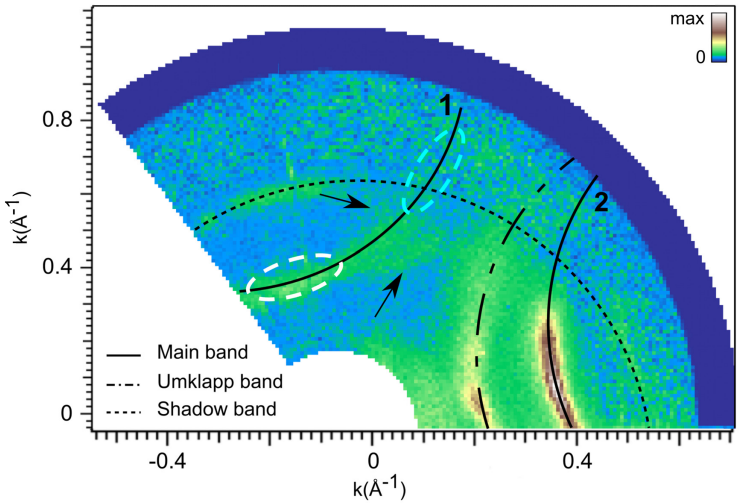

Figure 6.2: Map of the Fermi surface of optimally-doped Bi2212 measured at 100 K. The superimposed black lines are guides to the eye to clarify the assignment of the visible features (see main text): main bands (labelled 1 and 2, solid line), shadow band (dotted line), *umklapp* band (dotted-dashed line). The nodal region and the antinodal region are marked with dashed circles, in white and cyan respectively.

This overview shows that the matrix element effects at 10.8 eV photon energy are favorable to reveal most of the bands crossing E_F in Bi2212. Moreover, the high momentum resolution of the setup allows discerning also the finest details of the band structure, such as the bilayer splitting indicated by two arrows. However, the noise level in the outer region is higher than in the inner portion of the map. This is due to the presence of secondary electrons that increase further from normal emission due to the longer path required to escape from the sample surface. For this reason, the contrast of the features over the noise is less favorable and only allows distinguishing the prosecution of the main bands towards the Brillouin zone boundary and the existence of the shadow band, which in the lower part of the map falls in the outer region ($k \sim 0.55\,\text{Å}^{-1}$). This suggests that the photon energy of 10.8 eV is very close to the lower limit of photon energy for the feasibility of experiments extending far into the antinodal region. After having assessed the capability of the setup to measure photoelectrons from the antinodal region, we move to the exploration of its dynamics in comparison to the nodal case.

6.1.3 Pump-probe measurements close in the nodal and antinodal region

Figure 6.3(a) shows the equilibrium measurement performed at 110 K, hence in the pseudogap phase, along the nodal direction (see inset). The main band is visible as a sharp feature with k_F slightly smaller than $0.4\,\text{Å}^{-1}$. The presence of only one band means that the measurement is taken along the direction perpendicular to the *umklapp* replicas, *i.e.* we probe the band labelled as 1 in the Fermi surface map of Fig. 6.2. The effect of photoexcitation with $\sim 700\,\mu\text{J/cm}^2$ fluence is visible in the difference pump-probe map of

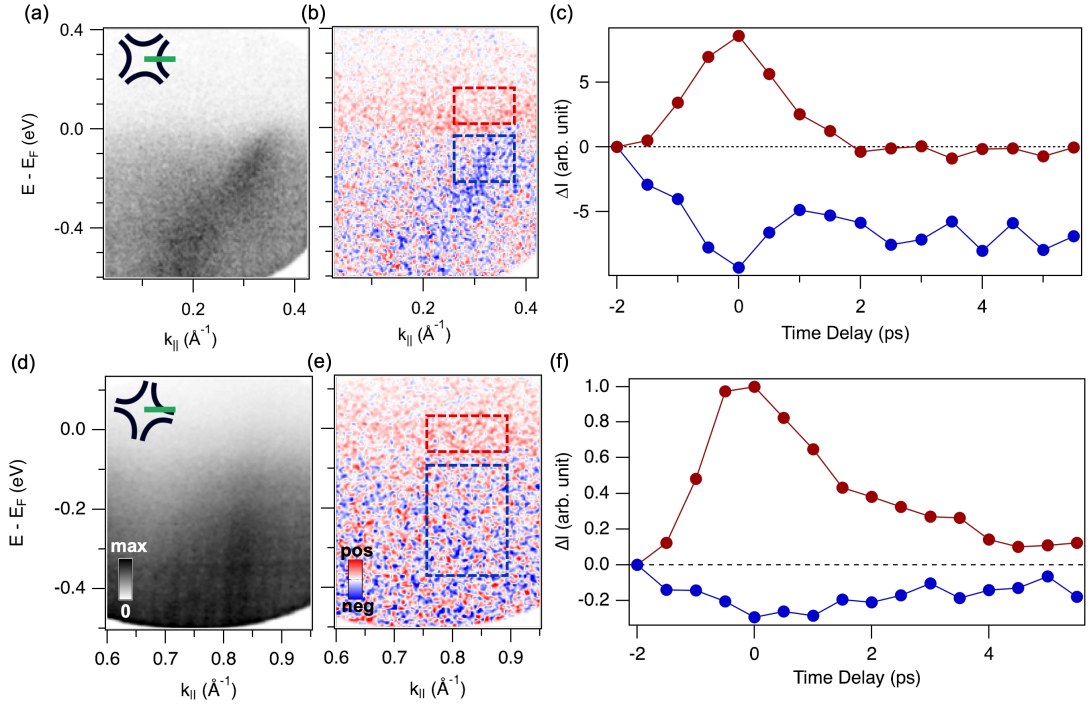

Figure 6.3: (a) Nodal dispersion measured at 110 K. The inset sketches the relative orientation of the analyzer slit (green line) and the main bands (black solid lines). In this case the analyzer slit is parallel to the nodal direction. (b) Difference pump-probe map. The pumped map is integrated 0.4 ps around time zero and the unpumped map is subtracted. (c) Intensity dynamics extracted in the boxes of corresponding color in panel (b). (d) Dispersion near the antinode at 120 K, in the geometry sketched by the inset: the sample azimuthal angle was rotated to reach a near-antinodal region. (e) Difference pump-probe map. The pumped map is integrated 0.4 ps around time zero and the unpumped map is subtracted. (f) Intensity dynamics extracted in the boxes of the corresponding color in panel (e).

panel (b), integrated 0.4 ps around time zero. There is a clear population above the Fermi level and a depopulation in correspondence to the nodal band. The intensity dynamics extracted in the red and blue boxes, above and below E_F respectively, are displayed in panel (c). The population above E_F shows a quasi-gaussian like temporal relaxation. This is a reasonable expectation for quasiparticles close to the node, where the pseudogap is zero and the relaxation is metallic-like, and hence fast with respect to the resolution of the setup. The population of the band below E_F instead shows a depletion close to time zero, but is followed by a plateau which lasts longer than the investigated time delay range. This might be due to charge redistribution towards other regions of the Brillouin zone, where the recombination is slower due to the presence of the gap [19].

Figure 6.3(d) shows the photoemission map acquired in the vicinity the antinodal region. This condition was obtained by starting from the nodal geometry shown in panel (a) and rotating the azimuthal angle of the sample. This approach has the major drawback that the analyzer slit is parallel to the direction of the bands, and hence the band spreads

across a large part of the analyzer slit aperture. A region with photoemission intensity significantly larger than the background is detected around $k_{||} \sim 0.8\text{Å}^{-1}$, close to the Brillouin zone boundary. The small population close to E_F stems for the presence of the pseudogap. The effect of photoexcitation, shown in the difference map of panel (e), is a distinct population below E_F down to -100 meV, while below this value the population decreases. This observation is also confirmed by the intensity dynamics of panel (f). The photoemission intensity difference is in absolute value larger in the red box than in the blue box, hinting at a redistribution of the hot electrons between different part of the Brillouin zone already close to time zero. Moreover, the red trace suggests the presence of longer dynamics, lasting at least 5 ps and thus, if modeled by a single exponential decay, of time constant of ∼1.5 ps. This is compatible with the presence of the gap that, limiting the phase space available for scattering, reduces the quasiparticle recombination rate and slows down the recovery [16]. The population decrease within the blue box is smaller and, at variance with the nodal case, shows and indication of recovery similar to the red trace.

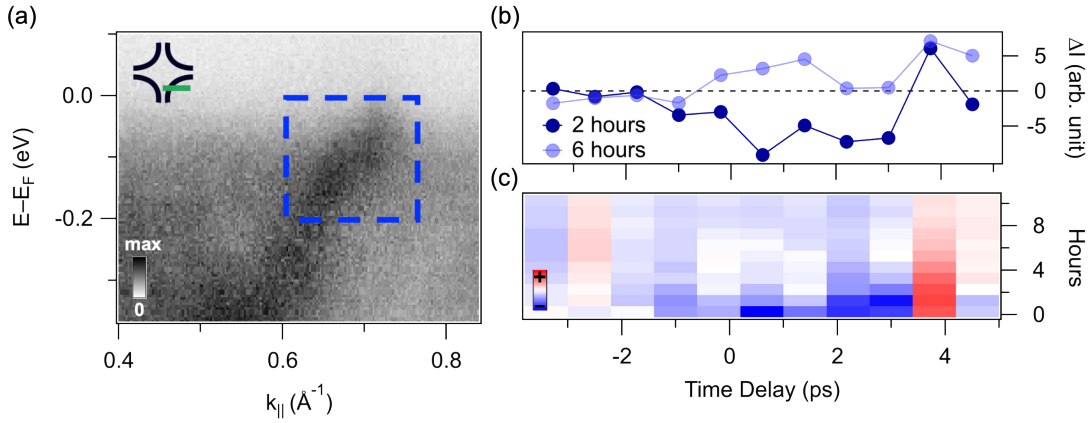

Figure 6.4: (a) Dispersion measured close to the antinodal region at 30 K. The sketch shows the relative orientation of main bands and analyzer slit, the latter being parallel to the antinodal direction. (b) Intensity dynamics extracted in the dark blue box of panel (a) at two different times as the measurement proceeds. The light blue curve shows a negative variation around time zero that is washed away in the dynamics acquired two hours later. (c) 2D plot of the traces as for panel (b), as function of time delay and of the integration time, *i.e.* the time elapsed in during the measurement.

Since the geometry of the measurement in Fig. 6.3 is not favorable to study the antinodal dynamics, as a next step we addressed the antinode under a different geometry. A more favorable strategy is to vary the manipulator tilt angle, with the antinodal direction parallel to the direction of the slit, as shown in the inset of Fig. 6.4(a). The capability of changing the tilt angle in our setup is limited to ±10° due to the construction of the manipulator, so the sample is placed on a special sample holder that is pre-tilted outside the chamber by 30° in order to reach large angles away from normal emission. The result of the photoemission experiment in an intermediate region between the node and the antinode is shown in Fig. 6.4(a). This measurement was performed at 30 K, hence in

the superconducting phase. Also in this case the small intensity in the close vicinity of E_F stems for the presence of the gap. The fluence employed was much smaller than in previous measurements, $\sim 20\,\mu\mathrm{J/cm^2}$, hence below the threshold to vaporize the superconducting phase. The transient intensity evolution extracted in the dark-blue dashed box are reported in panel (b). The dark blue curve, obtained by integrating the signal for two hours, shows a small effect close to time zero which might be indicative of photoinduced nonequilibrium dynamics. The signal is almost hidden in the noise, also due to the low fluence set. Nonequilibrium signals, however, should be detectable at fluences as small as $1\,\mu\mathrm{J/cm^2}$ [16]. The possibility of exploring higher fluences was hindered by a severe signal degradation that took place with the elapsing measurement time. As shown by the light-blue curve in Fig. 6.4(b), the signal was already fading away after six hours of integration. This evidence is even more striking in panel (c) where the intensity traces are shown in a map as a function of the time delay and of the total integration time of the trace itself, *i.e.* the time elapsed during the measurement. The signal, clearly present for the first two hours of the measurement, instead of emerging above the noise floor is washed away by integration in the subsequent measurements. Repeated attempts to perform the same measurement also in the pseudogap phase led to the same result.

We emphasize that the dynamics in the superconducting phase in this momentum region display a fast ($<$0.5 ps) and a slow component ($>$2 ps), smaller than the first [16]. The time resolution of our setup is too coarse to address the fast dynamics, which is lost in the noise, and hence the only nonequilibrium signal that can be detected is the small slow component of the relaxation, as proven by Fig. 6.4(b). This fact, in addition to the signal degradation effect, severely limits the extent of information that can be obtained on the antinodal dynamics in Bi2212 with the present configuration of the 10.8 eV setup.

6.2 TR-ARPES investigation of the O $2p$ dynamics

After having realized that measuring the antinodal dynamics in cuprates is challenging because of the technical parameters of the setup, we turn to the investigation of a related problem, namely the dynamics of the oxygen bands. The fact that different electronic states in cuprates are inextricably coupled has been shown in [223] where the low energy-scale phenomena, such as the superconducting gap and the pseudogap ($\lesssim$100 meV) were fund to be intertwined to the high energy excitations of these system ($\sim$1 eV). Hence we start from this evidence and tackle the problem of the O-band dynamics in cuprates. between low energy-scale phenomena, such as the superconducting gap and the pseudogap ($\lesssim$100 meV) and high energy excitations of these systems ($\sim$1 eV). This section introduces the topic of the high energy *charge-transfer* excitations and their relevance for cuprate physics. Since the O $2p$ states are involved in the charge transfer, we investigated the response of these bands upon the ultrafast redistribution of charges induced by the infrared pump.

6.2.1 Charge-transfer excitations in Bi-based cuprates

In order to understand the relevance of oxygen states for the low-energy physics of cuprates, it is useful to follow how the electronic structure close to the Fermi level evolves upon doping the system, when passing form the antiferromagnetic insulating phase to the superconducting or pseudogap one (see the phase diagram of Fig. 6.1(b)) [208]. A scheme of the low-energy electronic structure of the undoped compound is shown in Fig. 6.5(a). The large Coulomb repulsion experienced by the Cu $3d$ orbitals opens a correlation gap (U) which is larger than the bandwidth and would define the system as a Mott-Hubbard insulator. However, because of the large U, the states at the smallest energy from E_F are the O $2p$ ones, hence the first excitation of the system is the charge transfer across the gap of amplitude Δ among oxygen and copper states in the valence and conduction bands respectively [224, 225]. For this reason, the undoped compound is defined as a *charge transfer insulator* [226].

Upon doping, new states appear inside the gap at the down-shifted chemical potential (Fig. 6.5(a)) [228, 229], but the remaining structure is still reminiscent of the charge-transfer phase [223, 230, 231]. This is the origin of the intertwining of high-($1-10$ eV) and low-energy scales (<1 eV) typical of strongly-correlated systems in general [232–235] and also of cuprates [207, 236–239]. This picture suggests that also in the finite-doping phases the electron-electron repulsion and the charge transfer are the dominant interactions, thus influencing the low-energy physics of superconductivity and pseudogap, although these happen on an energy scale that is more than 10 times smaller.

Notwithstanding these evidences, the role of the high energy excitations in shaping the exotic properties of the gapped phases of cuprates is still an open question. We investigated the issue by addressing in the nonequilibrium regime both the O $2p$ valence-band states and the O $1s$ core levels, which provide access to different information on the same physics.

The dynamics of the O $2p$ states have been previously investigated by TR-ARPES by

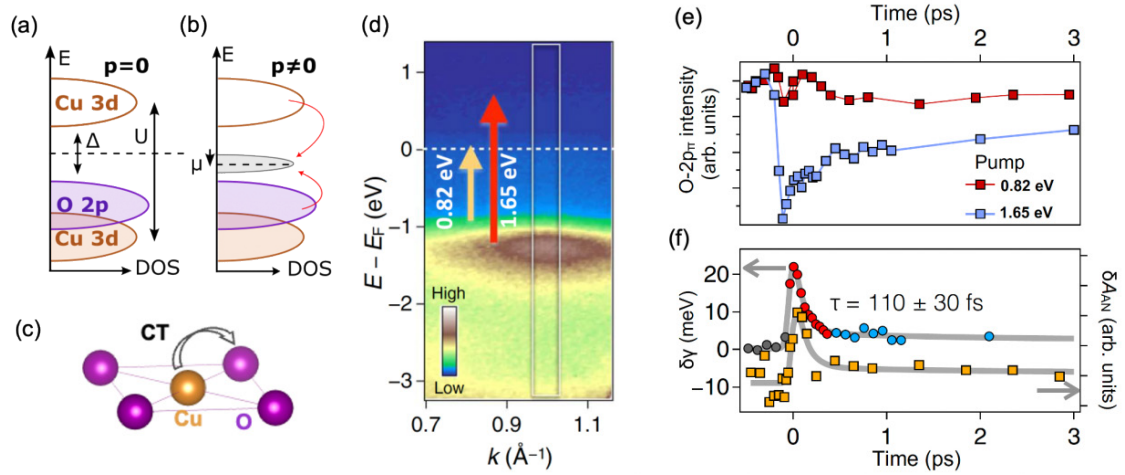

Figure 6.5: (a) Schematic of the density of states close to the chemical potential in an undoped charge-transfer insulator (p = 0). U Mott-Hubbard gap between Cu states, Δ charge-transfer gap, and μ chemical potential. (b) Same as (a) but for the doped conducting system (p ≠ 0) (c) Cu-O plane with the charge transfer process. (d) O 2p band measured by HHG, with the arrows schematizing the excitation pathway at two different photon energies. (e) Photoemission intensity dynamics of the O 2p states induced by two different pump photon energies. The absence of appreciable dynamics for the 0.82 eV pump signals the nonthermal nature of the effect. (f) Comparison between the time evolution of the O 2p band broadening ($\delta\gamma$) and the population dynamics within the gap at the antinode δA_{AN}, which show a similar timescale. (e),(f) are adapted from [227].

Cilento *et al.* [227]. The leading idea is that a laser pulse at $h\nu \sim 1.65$ eV can trigger an optical transition across the remnant charge-transfer structure. In fact, the dynamics of the O 2p states are relevant only if the photon energy is suitable to extract charges from the O 2p states (visible as a strong feature in Fig. 6.5)(d), and promoting them to empty states above E_F, which share a Cu-derived character. In this case, a decrease in the intensity of the O 2p peak is observed (blue trace in Fig. 6.5(d)). On the contrary, no appreciable dynamics are visible with a pump beam set to the photon energy of 0.82 eV (red trace in the same panel), which also proves that the effect of the pump is not purely thermal. In addition to a depopulation due to the pump-induced charge redistribution, the oxygen states also undergo an ultrafast broadening that the authors attribute to an inhomogeneous excess of holes in the oxygen bands.

Concomitantly to this, new electronic states are observed to appear inside the gap, as an effect of photoexcitation. Interestingly, the relaxation of the impulsive broadening of the oxygen band and of the intra-gap antinodal population are identical (Fig. 6.5(f)) hence indicating a close relation between the excess population inside the antinodal gap and the excess of holes created in the O 2p states.

These measurements were performed with an HHG source that provided an energy resolution of ∼250 meV for the measurement at the antinodes and ∼160 meV for the oxygen states. Such values prevented the authors from reconstructing the detailed dispersion of

the oxygen band, possibly hindering more details of its dynamics, which were masked by the resolution. Given that the maximum of the oxygen band is located ~ 1 eV below E_F and at $k_{||} \sim 1$ Å^{-1}, the 10.8 eV photon energy is not sufficient to perform a photoemission experiment. Motivated by this, we investigated the O $2p$ dynamics with the SPRINT HHG source (Sec. 3.2.1), that provides higher photon energy and is capable of sufficient energy resolution (below 30 meV) to resolve the dispersion of the oxygen states and reveal their dynamics.

6.2.2 Dispersion and dynamics of the O $2p$ states

The measurements were performed on an optimally-doped Bi2212 sample at room temperature. The probe photon energy was set to 26.4 eV and the pump photon energy to 1.2 eV, sufficient to remove electrons from the top of the oxygen bands and inject them close to the Fermi level. The pump fluence was set to $\sim 320\,\mu$J/cm^2, which is very close to that employed in [227].

Figure 6.6(a) shows the dispersion measured along the nodal direction from the Γ point up to the zone corner. This map is obtained by measuring the photoemission intensity in adjacent momentum regions, by changing the polar angle, and subsequently sticking the maps together. The vertical stripes of higher intensity are artifacts caused by this merging procedure.

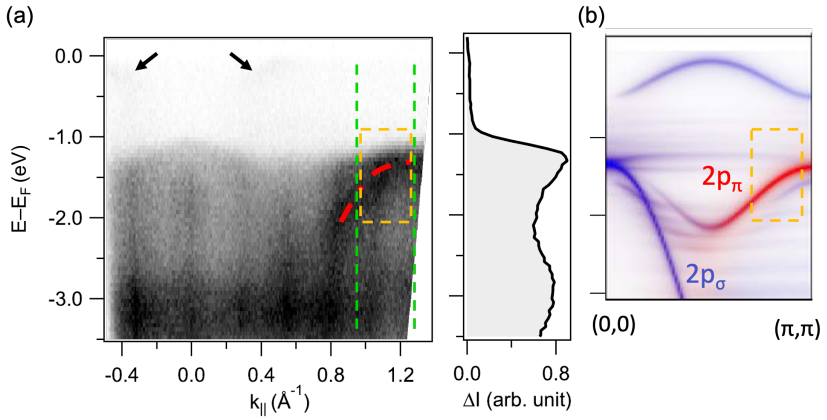

Figure 6.6: (a) Photoemission maps acquired on an optimally-doped Bi2212 sample at room temperature with 26.4 eV photons, along the nodal direction. Vertical lines of larger intensity arise due to the merging of maps acquired in adjacent momentum regions. The black arrows point at the main nodal bands. The red dashed-dotted line is a guide to the eye to emphasize the dispersion of the oxygen band. The yellow dashed box indicates the region where the ARPES intensity has been averaged (over momentum) in the time-resolved experiment (see main text). Side panel: EDC in the energy region marked by the green lines. (b) Projection of the calculated band structure of the valence band on the $2p_\sigma$ (blue) and $2p_\pi$ (red) oxygen orbitals. The energy and momentum axes are scaled according to panel (a). The yellow dashed square indicates the region of the pump-probe measurement. Adapted from [227].

The two black arrows point at a weak photoemission intensity close to E_F, indicative

of the main band nodal dispersion. The oxygen band is visible at higher energies and larger k, and evidenced by a red dotted-dashed line. The vertical-stripe artifact overlaps with the intensity coming from the oxygen band around $k_{||} = 0.8\,\text{Å}^{-1}$, however at larger k values its upward dispersion can be clearly distinguished. The band reaches its maximum around $k_{||} = 1.2\,\text{Å}^{-1}$. This dispersion qualitatively agrees with the one of the O $2p_\pi$ as predicted by the calculations and shown in red in panel (b) [227]. The large intensity ubiquitously present around 3 eV below E_F is attributable to the lower Cu $3d$ Hubbard band.

In both panels (a) and (b), a yellow box indicates the region where the pump-probe experiment was performed, integrating in its angular range. Due to technical constraints of the analyzer used for this experiment, a bias of +5 V had to be applied in order to push the electrons from the O $2p$ band to higher kinetic energies and allow their measurement with suitable values of kinetic and pass energy for the analyzer. Application of electric fields to the sample can in general lead to severe distortions to the photoelectron angular distribution, especially in this case where the whole sample holder is biased and the shape of the electric field around the sample is not uniform. For this reason, although the pump-probe measurement was nominally performed in the region enclosed by the yellow box, its location in the E *vs.* k space is just approximate.

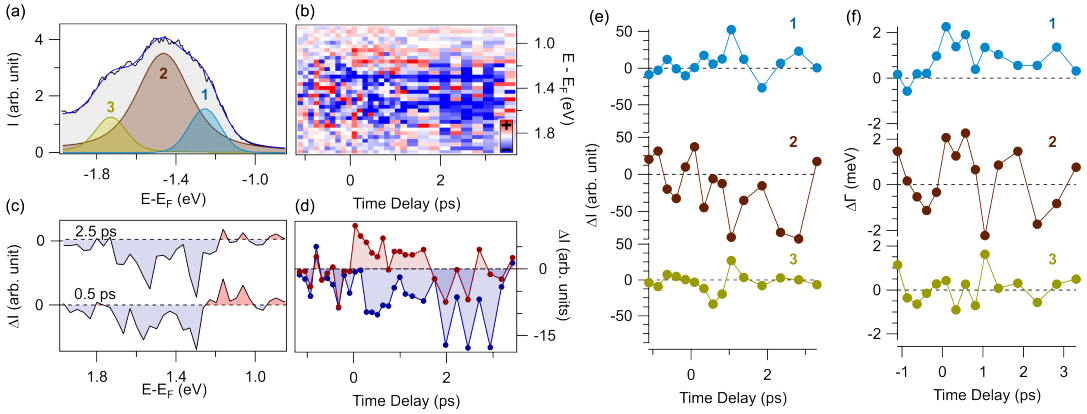

Figure 6.7: (a) EDC from the pump-probe measurement acquired before time zero. The blue line is the fit using the three peaks reported below. (b) Difference map showing the pump-probe spectra as a function of binding energy and time delay. (c) dEDCs extracted at 0.5 ps and 2.5 ps after time zero, evidencing that only the negative signal at larger binding energies survives longer. (d) Intensity dynamics extracted in the energy regions indicated in panel (a) with dashed lines of corresponding color. (e) Evolution of the amplitude of the three peaks, plotted as the difference with respect to the unpumped values. (f) Evolution of the width of the three peaks (difference with respect to the unpumped value).

Figure 6.7(a) shows the equilibrium EDC obtained in the pump-probe measurement before time zero. The position of the main peak confirms that this is the oxygen band identified in Figure 6.6(a). To satisfactorily fit the distribution, three Lorentzian peaks were employed. Also the calculation in panel (b) shows two weak p_σ bands at the zone boundary, above and below the strong p_π band.

The result of the pump-probe measurement is shown in the difference map of Fig. 6.7(b) as a function of binding energy and time delay. As also the dEDCs in panel (c) show, photoexcitation induces a positive signal around 1.2 eV below E_F, while a strong decrease in intensity is observed at higher binding energies. At later time delays, the positive signal is washed out while the strong negative signal is still present. This is indeed confirmed by the dynamics of the photoemission intensity shown in panel (d), extracted around -1.2 eV and -1.5 eV. The red trace goes to zero after ~ 2 ps while the blue one shows a persistent negative signal, although with a low signal-to-noise ratio.

To assign the pump-induced changes to a lineshape modification of the three components, we fit the EDCs at each time-delay and monitor the dynamics of the fitting parameters. Given the small signal-to-noise ratio of this measurement, it was not possible to fit the dynamics with all the peak parameters as free fitting parameters. We thus constrained the position of the peaks to be fixed, in view of the results commented from [227]. The model thus comprises three free amplitudes and three widths, for a total of six free parameters. The results are reported in Fig. 6.7(e) for the amplitudes and (f) for the widths. From the results, we learn that peaks 1 and 3 do not undergo significant changes in amplitude, while peak 2 shows a depletion at time zero which closely follows the intensity dynamics of the blue trace in panel (d). This means that the long negative signal observed is due to a depletion of peak 2, in agreement with [227]. The dynamics of the widths confirm the negligible role of peak 3, while peak 2 shows an indication of a broadening around time zero. Peak 1, instead, shows a clear broadening at time zero followed by a decay that is not recovering its equilibrium value within the $\sim$3 ps delay range of the measurement. This proves that the positive signal close to -1.2 eV commented above is due to a broadening of peak 1.

The signal-to-noise ratio of the measurement, while suffices providing the dispersion of the O $2p_\pi$ band up to the zone corner and indicating the depletion and broadening of two of the oxygen features, is not enough for the investigation of further finer details of the dynamics of these states. The presence of nonequilibrium effects on the oxygen bands nonetheless indicates that the photon energy of 1.2 eV, while being exactly in the middle between the two limiting cases exemplified in Fig. 6.5(e), suffices to induce a charge redistribution that involves the O $2p$ states. The compatibility of our results with the ones reported in [227], where the nonthermal nature of the excitation is proven, indicates that also the effect induced by a 1.2 eV pump is nonthermal.

6.3 Plane-dependent oxygen response to impulsive charge redistribution

A strong indication that the charge-transfer interaction dominates the response to photoexcitation can come from a comparison between the dynamics of the oxygens in different planes of the unit cell, since this interaction is localized in the Cu-O plane [224]. However, TR-ARPES is not a site-sensitive technique, and hence it cannot be applied to investigate this further point. As illustrated later in this section, site-specificity can be recovered by looking at the O $1s$ core levels by means of X-ray photoelectron spectroscopy (XPS). We therefore applied this technique integrated in a pump-probe scheme and it unveil the plane-dependent response of the oxygen atoms in Bi2212. Our measurements show that such an experiment is feasible on cuprates and unveils the prominent role of the planar oxygen in the response to photoexcitation.

6.3.1 Addressing the O $1s$ core levels

Although the fundamental properties of cuprates are mostly determined by the Cu-O planes, the presence of oxygen in other planes of the unit cell also plays a significant role, although with different consequences on the properties of the system. First, the extra oxygen content that dopes the Cu-O plane with holes resides in the *reservoir* layers [240, 241]. On the other hand, the phonons associated to the motion of the apical oxygen (Sr-O plane) have a dramatic impact on superconductivity [242–245]. Therefore, it is reasonable to expect that the different role of these oxygens in shaping the properties of cuprates is mapped into a distinct response to photoexcitation. In particular, since as discussed above an effect of photoexcitation at suitable photon energy is the redistribution of charges among states involved in the charge transfer interaction taking place in the Cu-O plane, this oxygen species is expected to play a peculiar role in the charge redistribution following photoexcitation.

In order to distinguish atoms occupying different planes of the unit cell, core levels must be addressed, since the coordination induces a chemical shift that is specific to each plane. For this reason, the cuprate compounds have been studied with XPS by means of both conventional [246–248] and synchrotron sources [240, 249]. As shown in Fig. 6.8(b), sufficient energy resolution ($\sim$150 meV) allows decomposing the O $1s$ core-level emission into three components. After long debate [250–256], the components have been univocally attributed to oxygens residing in specific planes of the unit cell, as depicted in Fig. 6.8(b): planar oxygens (Cu-O plane, violet), *reservoir*-layer oxygens (Bi-O plane, grey) and apical oxygens (Sr-O plane, green) [240].

The complete picture of the site-dependent oxygen dynamics in cuprates upon ultrafast charge redistribution can nowadays be achieved owing to the possibility, offered by free-electron lasers, to combine XPS into a pump-probe scheme and realize an ultrafast core-level spectroscopy (cf. Sec. 3.2.2). We thus performed the first time-resolved XPS study on a cuprate superconductor to unveil the response of the oxygen atoms in each layer of the unit cell upon photoexcitation with infrared light.

The experiment was performed at the PG2 beamline of the free-electron laser FLASH

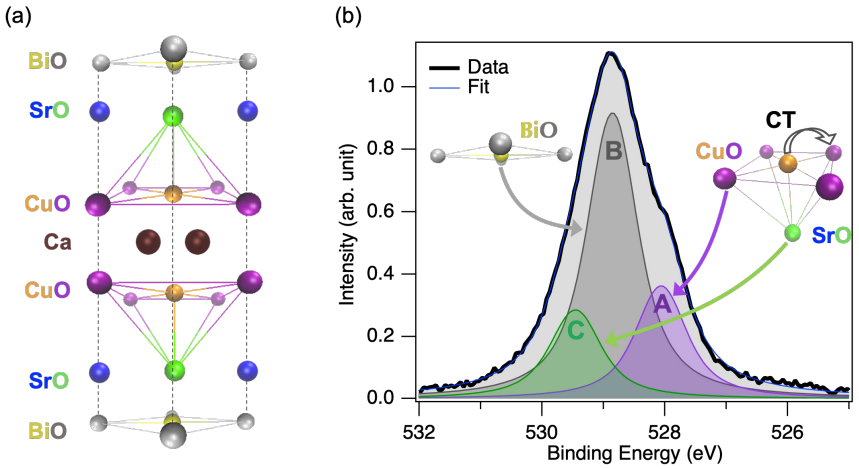

Figure 6.8: (a) Crystal structure of $Bi_2Sr_2CaCu_2O_8$ (Bi2212). (b) O1s line from an optimally-doped Bi2212 acquried at FLASH with 593 eV photons and 100 K temperature. The chemical shift is in induced by the different environment, which allows assigning each component to oxygen atoms in a specific layer of the unit cell: peak A (violet) to planar Cu-O oxygens, peak B (grey) to Bi-O oxygens, peak C (green) to apical Sr-O oxygens.

using the momentum microscope instrument described in Sec. 3.2.2. This allowed collecting the photoelectrons in the full emission solid angle above the sample surface. The sample used was an optimally-doped Bi2212 with transition temperature of about 91 K. Measurements were performed after cleaving the sample in ultra-high vacuum at a base temperature of 100 K in order to minimize thermal broadening effects in the photoemission spectra. To address the O 1s core levels, the FEL emission was set to 197 eV and the third harmonic at 592 eV was used. The spot sizes on the sample surface, estimated with the PEEM mode of the momentum microscope, were 50×200 wide (FEL probe) and 100×270 (laser pump). After correction for multi-photon emission effects [109], and having set the energy per pulse of the pump to 2.4 μJ, the pump fluence was $\sim 1\,\mathrm{mJ/cm^2}$, suitable to mitigate pump-induced space-charge effects and obtain a good signal-to-noise in the pump-probe measurement. The energy calibration of the instrument was performed with the methods reported in [108, 109, 114].

6.3.2 Dynamics of the O $1s$ core levels

Fig. 6.9(a) shows the intensity distribution of the O $1s$ peaks as a function of time delay and binding energy. The panel on the right shows the photoelectron distribution in a 0.2 ps-wide interval before time zero. As commented above, this structure comprises three components corresponding to different oxygen sites in the unit cell. We fit the spectra using symmetric Lorentzian peaks with three different widths, as also found in [251]. We convolve the sum of the peaks with a Gaussian to account for several sources of broadening, *i.e.* photon pulse and monochromator bandwidth, thermal broadening, and space charge. The Gaussian broadening amounts to ~0.54 eV. The other parameters

obtained for each peak are reported in Tab. 6.1 and show good agreement with the values available in literature [225, 250, 251].

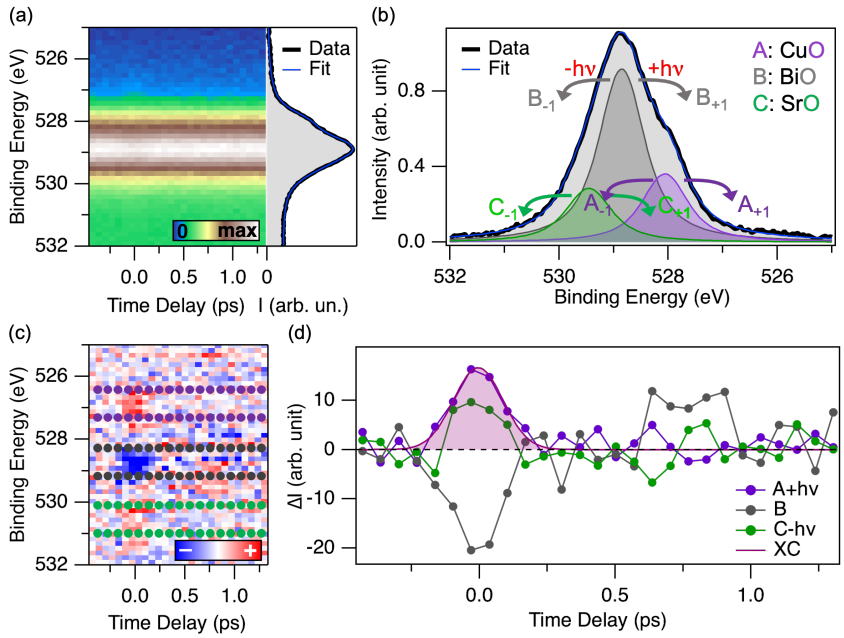

Figure 6.9: (a) Photoemission intensity of the O 1*s* emission plotted as a function of time delay and binding energy. The side panel reports the EDC integrated in a 0.2 ps-wide delay window before time zero. (b) Background-subtracted spectrum integrated in a window of 0.2 ps around time zero, schematizing the energetics of sideband generation and the nomenclature used in the analysis. (c) Difference between each spectrum of the map in panel (a) and the average of the spectra in the first 0.2 ps of the measurement. (d) Traces integrated in the regions denoted by the corresponding colored markers in panel (c). The curve superimposed to the violet trace is a gaussian fit yielding a FHWM of ∼0.2 ps.

Having interpreted the main parameters describing the O 1*s* core level as obtained by our experiment, we now turn to the analysis of pump-probe measurements. The presence of the pump pulse affects in several ways the photoelectron distribution. The evolution of the spectrum around time zero is dominated by the dressing of the photoelectrons with photons from the pump infrared field, a phenomenon known as Laser Assisted Photo-Emission (LAPE). In gas phase experiments, LAPE is a well-established technique to probe fundamental properties of the sample system or of the light pulses themselves [104, 257, 258]. Its exploration for solid sample systems is more recent and has been predominantly studied on metal surfaces [259, 260]. Fig. 6.9(b) schematizes the energetics of the process leading to LAPE in the framework of a phenomenological two-step approximation. In the first step, the probe photon photoemits the electron from the atomic core level into the continuum, and the interaction with the infrared light field is neglected. In the second step, the free photoelectron interacts with the infrared light field and undergoes absorption or stimulated emission of one or more photons. As a result, weaker replicas of the main peaks appear at a distance in the energy of one or more pump photons and are for

Component	**Assignment (plane)**	**Relative Amplitude to B**	**Binding Energy (eV)**	**Lorentzian FWHM (eV)**
A	Planar	0.17 ± 0.01	527.97 ± 0.01	0.48 ± 0.04
B	*Reservoir*	1.00 ± 0.05	528.84 ± 0.01	0.96 ± 0.03
C	Apical	0.14 ± 0.03	529.48 ± 0.04	0.66 ± 0.09

Table 6.1: Summary of the O 1*s* parameters extracted from the fit in Fig. 6.9a. Amplitudes are reported as a fraction of the amplitude of the B component. The errors on the values are derived from the fit uncertainties.

this reason called sidebands.

Sidebands in our measurement are easily distinguished in the difference map of Fig. 6.9(c), obtained by subtracting the equilibrium spectrum (side panel of Fig. 6.9(a)) from each of the spectra as a function of the time delay. The blue signal around 529 eV indicates that the main peaks are depleting due to the population of the sidebands, which in turn appear as a positive signal at a distance compatible with one pump photon energy. Only first-order sidebands, *i.e.* sidebands generated by one-photon interactions, are considered in the model since multiphoton effects are hidden in the noise floor.

Since it is based on the interaction between photoelectrons and pump photons, the existence of the sidebands is strictly related to the simultaneous presence of photons from the pump and from the probe at the sample position. The sideband dynamics can thus be used to determine the position of time zero and the cross-correlation FWHM. For this reason, we extracte difference intensity traces from the energy regions marked by round markers in the map of Fig. 6.9(b), and report them in Fig. 6.9(d). The dynamics of the photoemission intensity close to the sideband are well fit with a gaussian of full width at half maximum of 0.2 ps. The slight difference in the recovery of the three traces at later time delays indicates that the relaxation of the system back to equilibrium is not only due to the sideband disappearance, but dynamics with longer timescale are involved.

To rationalize the response of the system in terms of lineshape changes, we fit each spectrum of the time series with the same model used for the spectrum before time zero in Fig. 6.9(a). The results of this fit are used as initial parameters to fit the first spectrum of the series, and each subsequent spectrum is fit starting from the parameters obtained for the previous one. Each sideband is taken into account as an additional peak with the same lineshape as the corresponding main line, but with a smaller amplitude. Our model thus comprises three oxygen peaks, and two sidebands for each peak (at $\pm h\nu$). Since each peak has three defining parameters (amplitude, position, and Lorentzian width), this would yield a total of twenty seven parameters, a number that must be reduced also in view of the vicinity of the oxygen components with respect to their width and the signal-to-noise ration of the pump-probe measurement. The equal probability of absorption ($+h\nu$) and stimulated emission ($-h\nu$) allows constraining the amplitude of the upper and lower sidebands to be equal ($X_{+1} = X_{-1}$, $X = A, B, C$). The energy separation of the sidebands is also independent of the pump-probe delay, as it is defined by the pump photon energy. As also reported in literature [261] we fix the Gaussian broadening to its equilibrium value The capability of this model to fit the full structure around time zero is demonstrated by the fit reported in Fig. 6.9(b). In particular, it corroborates the

assumption we made in fitting the dynamics, and further confirms the correctness of the energy scale calibration for this region of the spectrum. In the time domain, the only constraint applied is on the sideband amplitudes, which are allowed to gain a finite value only for two cross-correlations around time zero. This yields a total of nine free parameters outside the sideband region (amplitude, position and Lorentzian width of the main peaks) and three additional sideband amplitudes around time zero.

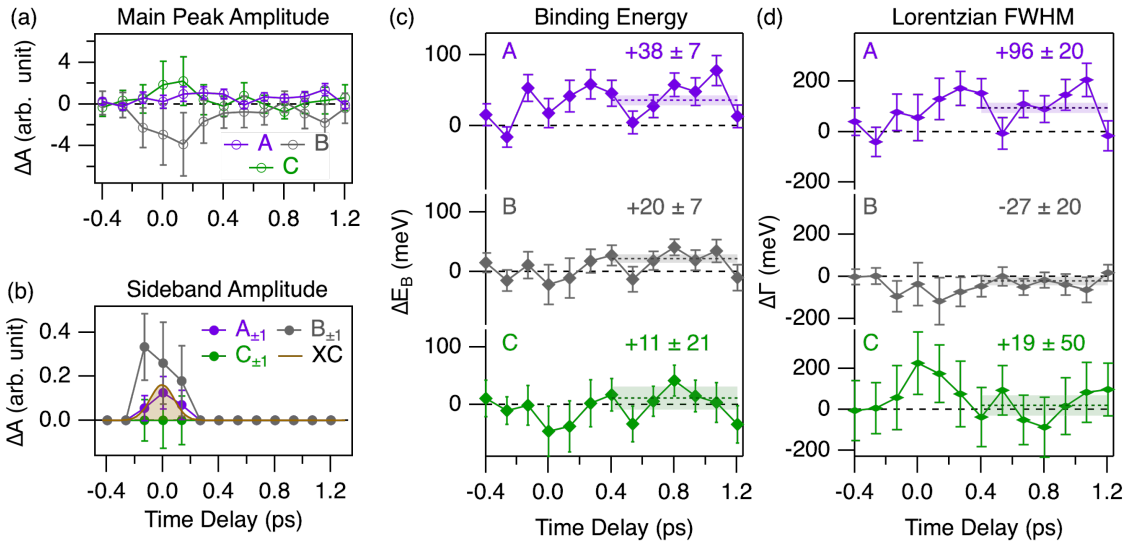

Figure 6.10: Dynamics of the fitting parameters describing the evolution of the O 1*s* components as a function of time delay. The traces indicate the difference with respect to the value before time zero. The color code indicates the O 1*s* component: A (violet, planar), B (grey, *reservoir*), C (green, apical). (a) Amplitude of the main emissions. (b) Amplitude of the sidebands, equal for upper and lower component and restricted to have finite values only around time zero. The brown curve is the cross-correlation extracted in Fig. 6.9d (FWHM ~ 0.2 ps). (c) Binding energy of the main emissions. The dashed lines are the average of the points after 0.4 ps and highlight nonequilibrium values of $+38 \pm 7$ meV (A), $+20 \pm 7$ meV (B) and $+11 \pm 21$ meV (C), the latter being compatible with zero. (d) Lorentzian FWHM reported as FWHM. Similarly to panel (c), numbers indicate the average value after 0.4 ps: $+96 \pm 20$ meV (A), -27 ± 20 meV (B) and $+19 \pm 50$ meV (C), the latter being again compatible with zero.

The dynamics of the fitting parameters are shown in Fig. 6.10. The amplitude of peak B (panel (a)) shows a depletion due to the generation of sidebands. The duration of the negative variation for more than the cross-correlation indicates that a change in spectral weight is occurring at time zero, and relaxes within half a picosecond. A decrease would also be expected at time zero for the other two peaks, due to sideband generation; at variance, the amplitude seems to be increasing, although still being compatible with zero within one standard deviation. A possible explanation is the presence of the sidebands of peak B ($B_{\pm1}$) which, being very close to the two peaks, partially mask their depletion. This correlation is also demonstrated by the somehow atypical behavior of the sideband amplitude $B_{\pm1}$ which, unlike $A_{\pm1}$, is only marginally compatible with the

expected gaussian-like behavior (grey and brown curves in Fig.6.10(b)). The small amplitude of peak C also causes its sidebands to be small and acquire error bars much larger than the observed variation. The maximum amplitude of $A_{\pm1}$ and $B_{\pm1}$, reached at time zero, is of $\sim 0.7\%$ relative to the main peak. After 0.4 ps, all three amplitudes have relaxed back to their equilibrium values. Remarkably, the dynamics of the position and width of the three (main) peaks show some important differences. Peak A is the most affected in both respects. It experiences a shift to higher binding energies and a broadening already at time zero. Both effects last for the whole delay range with an average respectively of $+38 \pm 7$ meV and $+96 \pm 20$ meV ($\sim 22\%$ broadening relative to the equilibrium value). The modifications of peak B are smaller, amounting to $+20 \pm 7$ meV and -27 ± 20 meV ($\sim 3\%$ relative to equilibrium). The changes of both the width and the position of peak C are compatible with zero in this delay range, signaling a faster relaxation back to equilibrium. At this stage of the analysis, it cannot be excluded that the small amplitude of peak C masks its dynamics, that are overwhelmed by the changes in peaks A and B.

6.3.3 Dynamics of the Sr $3d$ core level

Motivated by the small extent of the effects observed in the apical oxygen component, and given its importance in shaping the properties of cuprates, we complement the study by inspecting the dynamics of the Sr $3d$ doublet. Sr lies in the same plane of the apical oxygen only, and thus only one Sr $3d$ component is expected in the spectrum. The signal is free from contributions of neighboring components, offering an additional viewpoint on the role of the apical plane in the charge redistribution process.

Fig. 6.11(a) reports the photoemission intensity of the Sr $3d$ core level as a function of the time delay, with the right panel showing the integration over the first 0.4 ps. The equilibrium structure consists of a spin-orbit doublet (Sr $3d_{3/2}$ and Sr $3d_{5/2}$). Since these are metallic states, we fit the photoelectron spectra with a sum of Doniach-Sunjic (DS) peaks [262], allowing for asymmetric lineshapes, above a Shirley background [61]. The Sr $3d_{5/2}$ peak (D) is located at ~ 131.81 eV and the doublet splitting amounts to 1.71 eV. The ratio between the two peak areas (0.67 ± 0.01) is compatible with the theoretical prediction of $\frac{2}{3}$ for the $3d_{3/2}$-$3d_{5/2}$ doublet. An overall Gaussian broadening of ~ 0.5 eV results from the fit, in agreement with the value extracted for the O $1s$ components.

First-order sidebands are clearly visible in the map of Fig. 6.11(a). After integrating the spectrum around time zero (Fig. 6.11(b)), also the second-order sidebands can be discerned, at variance with the case of O $1s$. The differential map of Fig. 6.11(c) is thus integrated in the energy regions around the main and side peaks, leading to the evolution displayed in Fig. 6.11(d). The integration region and the resulting trace are indicated with the same marker type. The intensity dynamics in the sideband regions are well fit by a gaussian of FWHM 0.21 ± 0.01 ps for the first-order sideband and 0.22 ± 0.02 ps for the second-order one, both in good agreement with the cross-correlation extracted from O $1s$. The negative average of the blue signal at later time delays stems for an out-of-equilibrium effect beyond sideband generation.

As it is clear from Fig. 6.11(b) and (c), the fitting model needs to comprise one DS doublet for the main peaks, one for each of the first-order sidebands, and one each for the second-order sidebands. In agreement with what reported in the literature [261], in

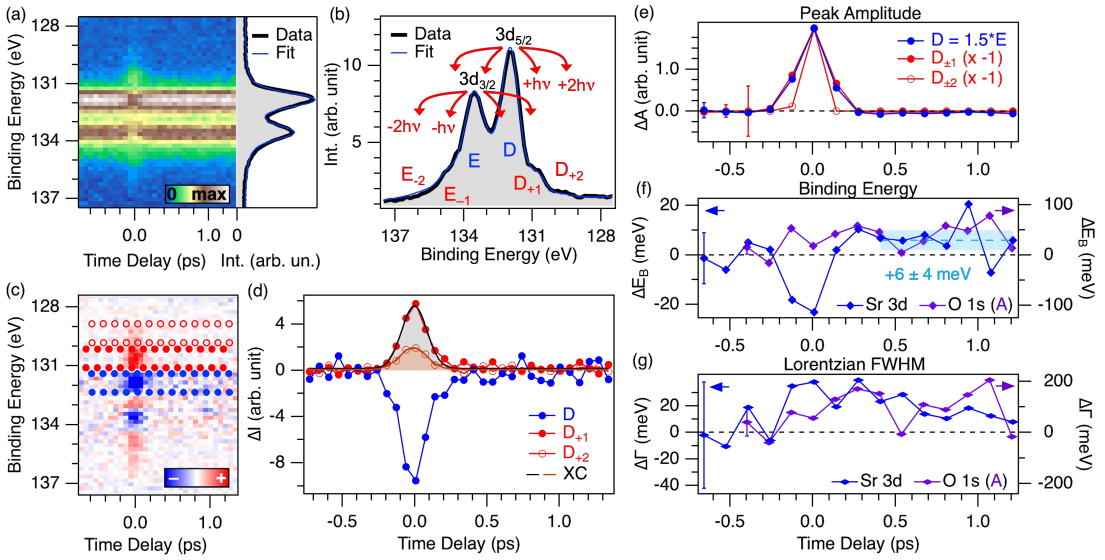

Figure 6.11: (a) Photoemission intensity of the Sr $3d$ doublet, and corresponding equilibrium spectrum fit as described in the main text (blue line). (b) Spectrum integrated around time zero in a 0.2 ps window, illustrating the energetics of sideband generation and the nomenclature used in the analysis. In this case, two orders of sidebands are visible. (c) Difference between each spectrum of the map in panel (a) and the equilibrium spectrum, as a function of the time delay. (d) Traces integrated in the region of the map in panel (c) denoted by the same marker type. Full blue circles, $3d_{5/2}$ main emission (D). Full red circles, upper first-order sideband (D_+1). Empty red circles, upper first-order sideband. Grey and orange lines are the gaussian fit of the photoemission intensity dynamics around the upper first- and second-order sidebands respectively. All the cases give a FWHM compatible with 0.2 ps. (e)-(g) Dynamics of the fit parameters for the spectra reported in panel (a) as a function of time delay. The traces indicate the difference with the value before time zero. The error bars are similar across the dynamics and are indicated only once in the first points. (e) Amplitude of main feature (filled blue circles), first- and second-order sidebands (filled and empty red circles). (f) Binding energy of the Sr $3d_{3/2}$ emission (blue, plotted against the vertical axis on the right) compared with the one of the A component of O $1s$ (violet, plotted against the vertical axis on the left). The average after 0.4 ps indicates a shift of $+6 \pm 4$ meV of the of Sr $3d$ doublet. (g) Lorentzian FWHM of the Sr $3d_{3/2}$ emission and of the oxygen A component, plotted as in panel (f).

addition to the Gaussian broadening, we assume that the internal structure of the doublet is not modified by the pump, so that the splitting and the ratio of the two DS peaks can be kept fixed in the time evolution. Similarly, the asymmetry is fixed to its equilibrium value. In this way, we monitor the time dependence of three parameters: amplitude, position and Lorentzian width. Similarly to oxygen, we impose the amplitude of the upper and the lower sideband to be equal for both orders ($X_{+1,+2} = X_{-1,-2}$, $X = D, E$) and finite only for two cross-correlations around time zero. The spacing of the sidebands is constrained by the pump photon energy. When fitting the complete dynamics in this framework, the number of free parameters is three outside the sideband region (amplitude, position and

Lorentzian width of the main DS doublet) and five in the sideband region (additional first- and second-order sideband amplitude). These constraints have been applied to fit the time-zero spectrum in Fig. 6.11(b), yielding a good agreement.

Fig. 6.11(e) shows the dynamics of main peak and sideband amplitudes, normalized to the maximum of the main peak to illustrate their similarity. The main doublet shows no significant variation except the depletion due to the sidebands, and in fact the dynamics are fully compatible with those of the first-order sideband. The finite amplitude of the second-order sideband has a shorter duration, but we ascribe this to a spurious effect of the fitting procedure, as the photoemission intensity variation at the second-order sideband position has the same duration as the first-order one (full and empty red circles in Fig. 6.11(d)). The amplitude ratio between the first-order sideband and the main peak is of $\sim 18\%$, 30 times larger than the case of oxygen. The position of the peak at time zero displays a shift of ~ 20 meV to lower binding energies, presumably of ponderomotive origin (Fig. 6.11(f)) [263]. Comparison with the planar O $1s$ component, reported on the same panel against the opposite vertical axis, shows that the two effects have the same sign, but the shift of the Sr $3d$ line is one order of magnitude smaller. The width of the peak, although affected by large error bars, also displays a larger change at time zero, which seems to relax in the subsequent dynamics. It is not possible to extract the timescale of this relaxation, since the width has not recovered its equilibrium value within the measured delay range. Based on the available data, a single-exponential decay would give a time-constant of at least 1 ps. This is qualitatively different from the dynamics of the width of the O $1s$ planar component, where no indication of relaxation is found within the measured delay range.

6.3.4 Comparison of O $1s$ and Sr $3d$ dynamics

Our measurements prove that a charge redistribution in the valence band of Bi2212 induces detectable changes in both O $1s$ and Sr $3d$ core levels. In the first place, the efficiency of sideband generation is markedly different for the two atomic species. Since second-order sideband generation involves the absorption or emission of two photons, its relative efficiency will scale as the square of the first-order one. In O $1s$ the latter is about 30 times smaller than in Sr $3d$, so second-order sidebands are expected to be ~ 1000 times weaker. This rationalizes the absence of second-order sidebands in the O $1s$ spectra around time zero.

More importantly, our measurements prove the capability of detecting the chemical environment-dependent dynamics of the oxygen states in Bi2212. In particular, the response of the three oxygen components to photoexcitation is quantitatively different. The largest changes are witnessed by the oxygen in the Cu-O plane, which undergoes a shift and a broadening of almost 40 meV and 100 meV respectively. The nonequilibrium effects experienced by the apical oxygen are instead null. This might be due to the presence of the neighboring components which, being much larger in amplitude, mask its dynamics. This fact surely contributes to the cause of the large uncertainty in the fitting parameters (see error bars in the green curves of Fig. 6.11). An indirect proof that the changes in the apical oxygen are actually small compared to the ones experienced by the planar oxygen comes from the inspection of the Sr $3d$ line. The lineshape modifications are one order of magnitude smaller than those observed in the planar oxygen. We stress the fact that the

sign of the binding energy shift is the same for Sr $3d$ and O $1s$. This allows to rule out pump-induced space-charge as an origin, since an opposite sign would be expected [57, 72]. Although it is possible that different species in the same plane experience different nonequilibrium changes, the evidence points to the fact that the Sr-O plane, and thus also the apical oxygen, is only marginally involved in the charge redistribution induced by the pump.

Taken together, these evidences indicate that the response to the photoinduced charge redistribution from the O $2p$ states in the valence band involves predominantly the Cu-O plane. This is also where the charge-transfer interaction takes place, thus further confirming that this interaction dominates the relaxation dynamics after impulsive photoexcitation.

6.4 Conclusions

Our study on optimally-doped Bi2212 has tackled two of the open questions in the field of cuprates. The first concerns the information that can be gained from the nodal-antinodal dichotomy on the origin and interplay of the superconducting and pseudogap phase. The second, but not independent, question regards the role of high energy excitations in defining the low-energy physics of cuprates, and therefore also the peculiar nature of the aforementioned gapped phases.

We performed TR-ARPES measurements with the 10.8 eV setup, both in the nodal and in the antinodal region. While at high excitation fluences the dynamics in the nodal and antinodal region could be detected, and qualitatively agree with the expectations, the dynamics at low fluence ($\sim$20 μJ/cm^2) could not be clearly resolved. Both the small signal-to-noise ratio and a signal degradation issue have impeded further investigation. This suggests that the 10.8 eV source, while capable of equilibrium photoemission at the antinode, is in the present configuration not suitable for providing the detailed information that such scientific questions require. In particular, the time resolution seems to be the limiting factor.

The second question has been addressed by inspection of both valence bands and core level dynamics. We directly studied the dispersion and dynamics of the O $2p$ states in the valence band. These states are directly influenced by the charge redistribution induced by the 1.2 eV pump photons employed, and also participate in the charge-transfer interaction between Cu and O. The photon energy required to reach these states is higher than 10.8 eV. For this reason, the measurement was performed with the HHG setup at SPRINT (see Sec.3.2.1) at 26.4 eV photon energy. The signal-to-noise ratio also in this case is rather poor, but evidences a clear band broadening and depletion, in accordance with the results from the literature, which also prove that the effect is nonthermal. These measurements, while not providing additional details on the oxygen dynamics in the valence band, demonstrate that photoexcitation at 1.2 eV, used also for the antinodal measurements as well as for the core-level investigation, indeed excites carriers from the O $2p$ states hence triggering the charge-transfer type interaction.

We further investigated the response of the oxygen states upon ultrafast charge redis-

tribution by inspecting the O 1*s* dynamics. This was done by using the free-electron laser FLASH as a source of 593 eV photons for the TR-XPS experiment. The dynamics of the three chemically-shifted components of the O 1*s* emission (planar, apical and *reservoir*) can be distinguished and are quantitatively different. While the planar oxygens are the most affected by the photoexcitation, the apical component undergoes negligible changes. The comparably small size of changes experienced by the Sr 3*d* core level confirms that the apical oxygen is the least affected by photoexcitation. This confirms that the Cu-O plane plays a dominant role in the response of the system to impulsive charge redistribution and point to a dominant role of the Cu-O charge transfer interaction shaping the relaxation dynamics.

One last conclusion regards the pump photon energy used in these experiments. A vast number of previous studies on cuprates employed a 1.5 eV pump (fundamental of Ti:Sapphire laser systems), while in the three experiments reported here we used a 1.2 eV pump (the fundamental of Yb-based laser systems). The nonequilibrium signal collected on the O 2*p* bands indeed proves that this photon energy is above the threshold to address this kind of physics. Nonetheless, the low signal-to-noise ratio common to all of the measurements reported in this chapter suggests that this photon energy might still be small and hence have a small efficiency in triggering the nonequilibrium conditions normally met with the 1.2 eV pump. This statement should be validated in the future by similar experiments performed with larger pump photon energy, *e. g.* the second harmonic of the 1.2 eV or the output of an OPA.

Chapter 7

Conclusions and perspectives

The study of the ultrafast dynamics in complex materials is a powerful method to unveil the fundamental processes that determine their physical properties, in addition to exploring nonequilibrium conditions that can exceed the possibilities attainable at equilibrium. TR-ARPES, providing information on the dynamics of the band structure, can unveil the microscopic mechanisms that drive the system response and relaxation. The extension of ARPES to the time domain finds in the time and energy resolution and in the measurement statistics the most important quantities that need to be optimized depending on the science case under scrutiny. The quest for overcoming these limitations has to deal with the properties of the photon source, and in particular of the probe source. In this work we show how third harmonic generation in gas is a viable method to advance the limitations in some of the parameters by discussing the operation and application of a novel setup for TR-ARPES at 10.8 eV photon energy [95]. In the operation conditions of the measurement presented in the previous chapters, the energy and time resolution resulted to be ∼80 meV and ∼1.3 ps. The setup can operate at repetition rate up to 1 MHz in a space-charge free régime.

The application of this source to three different scientific cases showcases the benefits that the capabilities of this setup offer to the investigation of quantum materials by TR-ARPES, along with pointing out possible developments of the source itself.

As a first example, we investigated the role of SOC in defining the dispersion of the surface state in the topological insulator Bi_2Se_3. Since semi-empirical models account for the hexagonal deformation of the constant energy surfaces of TSS in terms of SOC-dependent terms in the modeling of the *E vs. k* dispersion, we applied one-step *ab-initio* calculations of the photoemission from Bi_2Se_3 at 10.8 eV upon varying the SOC strength of the Bi atoms in the first 20 layers from the surface down to 50 % of its full atomic value. Higher values of SOC induce a larger warping close to the Fermi level by strongly deforming the dispersion along ΓM, while the one along ΓK remains linear, hence accounting for the hexagonal symmetry of the deformation. In order to benchmark the SOC dependent calculations, we compare them with equilibrium and non-equilibrium ARPES measurements performed at 10.8 eV, that can show the dispersion of the surface state well above the Fermi level in a single measurement. The strong deformation induced by the

100 % SOC at the Dirac point is not compatible with what observed in the experiment, and also the warping strength along ΓM is in excess of the measurement. The nonequilibrium measurements, performed to access the region above the Fermi level, show that the warping is compatible with a SOC of at least 70 %. We thus conclude that the effective SOC interaction is transferred to the surface for a fraction between 70 % and 85 % of its full atomic value.

Given the ubiquity of the hexagonal and snowflake warping of the surface state among topological insulators, our results on the dependence of the TSS dispersion on SOC are likely transferable to other similar systems. Application of the same SOC-dependent calculations to other topological insulators (Bi_2Te_3 and Sb_2Te_3 as first examples) would not only give further insights in the physics of these systems, but also provide a means of comparison to the reported case of Bi_2Se_3. Since we propose an effective SOC reduction at the surface based on a general mechanism, thus valid for all the TSS, we foresee that also for these systems the effective SOC transferred at the surface would be less than 100 %, although the exact fraction might vary depending on the details of the interaction among TSS, SRS and bulk bands. In particular, although displaying a Dirac point buried in the bulk valence band, the case of Bi_2Te_3 would be of particular relevance since the strength of the warping is larger [142] and thus the changes with the SOC could be more noticeable even below E_F.

The extended k-space range accessible by 10.8 eV photons is advantageous also to investigate the class of kagome systems, which recently got much interest due to their exotic properties arising from the coexistence of topology and correlation-induced phenomena. Purpose of the work presented in this thesis was to study the response of flat bands in the kagome metal CoSn to ultrafast optical excitation. Flat bands in kagome systems arise from the enhancement of the effect of correlations due to the peculiar geometry of the lattice, that forces localization of the electrons in real space. We investigated the response of the system to impulsive excitation by monitoring the dispersion of the flat bands, that encodes information on the electronic localization. The use of 10.8 eV as photon energy is in this case essential as it allows to measure the small CoSn samples (<0.8 mm) with negligible effects of the fringing fields from the sample edges on the photoelectron distribution, that would be disrupted at lower photoelectron kinetic energies. The matrix element at 10.8 eV turns out to be favorable for selectively probing only the flat bands. These disperse away from each other at large k values, and hence the 10.8 eV photon energy is also beneficial to reach this region and investigate the two independently. The two flat bands show an ultrafast renormalization in terms of energy and position, that lasts for one cross-correlation, and a small broadening that lasts for more than 6 ps. We ascribe these effects to a delocalization of the electrons induced by the pump pulse. The effects are small and suggest a robustness of the localization mechanism to infrared photoexcitation.

As a third example system, we reported investigations performed on the copper-based high-temperature superconductor Bi2212, giving an example for a well-studied system that still presents open research questions. Addressing these questions requires further development of adequate photon sources. For this reason, we show the results of the application of three state-of-the-art sources for time-resolved photoemission to tackle in-

tertwined questions on the physics of cuprates. In particular, the measurements conducted at 10.8 eV show that it is possible to reach the Brillouin zone boundary (hence the antinodal region), where the interplay between pseudogap and superconductivity can be studied by TR-ARPES. The dynamics at high fluence in the pseudogap phase show relaxation dynamics that are fast at the node and slower at the antinode. The attempt to investigate the antinodal dynamics in the superconducting phase is hindered by a degradation in the nonequilibrium signal, which on the other hand is small and shows no trace of fast dynamics close to time zero, as it would be expected. This points at the conclusion that the time resolution of the setup is too coarse to extract detailed information on the band structure at the antinode, which also at 10.8 eV requires a considerably off-normal emission geometry and hence suffers from a large background of secondary electrons.

Since in cuprates the charge-transfer excitations ($\sim$1 eV) between copper and oxygen in the Cu-O plane are believed to shape the properties of the gapped phases by intertwining different energy scales typical of cuprates, we investigated the dynamics of the oxygen states both in the valence band (O $2p$) and in the core levels (O $1s$) upon infrared photoexcitation, which directly redistributes charges from the O $2p$ states. The valence band measurements were performed with an HHG source, since they lie at the corner of the Brillouin zone and $\sim$1 eV below E_F. Despite the low signal-to-noise ratio, the measurement displays results in agreement with [227], *i.e.* a depopulation and a long-lived broadening. The investigation of the O $1s$ core levels was instead performed at the FLASH free-electron laser facility by TR-XPS. The technique allows distinguishing the oxygens residing in different planes of the unit cell, including the ones in the Cu-O plane, that are also involved in the charge-transfer interaction with Cu. Our measurements prove the possibility of inducing a charge redistribution in the valence band of Bi2212 and detect its effect by looking at the O $1s$ core levels. The three oxygen components (planar, apical, and reservoir) display quantitatively different response to photoexcitation. In particular, the planar oxygen is the most affected, undergoing a shift and a broadening, and revealing that the charge-transfer interaction plays a role in the relaxation of the system upon ultrafast charge redistribution. The fact that the response of the apical oxygen is small is also confirmed by the analysis of the Sr $3d$ line, which lies in the same plane, and likewise undergoes effects a factor 10 smaller than for the planar oxygen.

As commented in Sec. 3.3, the major limitation of the 10.8 eV setup is represented by the picosecond time resolution. In fact, the dynamics of the flat bands in CoSn in the first picosecond around time zero are resolution-limited, hence the details of the response to photoexcitation at small delays cannot be accessed. Also the electron dynamics at the antinodes of Bi2212 are hardly accessible in the present experimental configuration, mostly because of the time resolution of the setup. The 10.8 eV setup is expected to gain in time resolution by modification of the refocussing chamber, where the probe pulse elongates due to the presence of the wedged window. As proven by another implementation of a similar scheme [115], use of a grating should be beneficial for reducing the probe pulse duration after the refocussing stage. This upgrade would bring the time resolution closer to the state-of-the-art of the other ultrafast sources for TR-ARPES, while offering complementary capabilities with respect to those, hence advancing the possibilities of investigating quantum materials by TR-ARPES. The case of CoSn also shows how a

small spot size can be beneficial to study samples with limited lateral size, a condition that can be reached by improving the beam focusing at the sample position.

On the side of the pump beam, the high 10.8 eV generation efficiency demonstrated in Sec. 3.1.5 leaves much power to be employed on the pump path. A first step towards the pump photon energy tunability would be to employ a BBO for SHG, hence adding the capability of using a 2.4 eV pump to excite the sample. Another possibility, technically more challenging, is to install an OPA on the pump path, hence gaining continuous tunability of the pump in the visible and near-IR, and allowing for the study of resonant transitions triggered by a precise pump photon energy. Also for the pump, the study of CoSn shows how a more tightly focussed beam can help minimizing spurious photoelectrons form the edges in case of small samples.

The following paragraphs discuss possible future directions for the scientific cases presented in the last three chapters, also in view of the improvements on the 10.8 eV source that these studies call for.

Given the ubiquity of the hexagonal and snowflake warping of the surface state among topological insulators, our results on the dependence of the Bi_2Se_3 TSS dispersion on SOC are likely transferable to other similar systems. Application of the same SOC-dependent calculations to other topological insulators (Bi_2Te_3 and Sb_2Te_3 as first examples) would not only give further insights in the physics of these systems, but also provide a means of comparison to the reported case of Bi_2Se_3. Since we propose an effective SOC reduction at the surface based on a general mechanism, thus valid for all the TSS, we foresee that also for these systems the effective SOC transferred at the surface would be less than 100 %, although the exact fraction might vary depending on the details of the interaction among TSS, SRS and bulk bands. In particular, although displaying a Dirac point buried in the bulk valence band, the case of Bi_2Te_3 would be of particular relevance since the strength of the warping is larger [142] and thus the changes with the SOC could be more noticeable also below E_F.

To date, the application of TR-ARPES to kagome systems reported in literature is limited to one example [197]. This is due on one hand to the recent discovery of samples with properties close to the ideal kagome model, and on the other to technical challenges related to sample fabrication and measurement, as the reported example of CoSn shows. Given the fast growth of this research line in the condensed matter community, it is foreseeable that application of time resolved techniques, and photoemission in particular, will experience a rise in the near future, especially given the fact that many physical phenomena pertaining to kagome physics (topologically nontrivial phases, electronic correlations, charge-density instabilities) are routinely studied in other systems by TR-ARPES. Regarding the flat band dynamics, exploration of the sub-picosecond response close to time zero, where our study shows resolution-limited effects, can further elucidate the nature and timescales of the processes triggered by the pump. Larger samples (or sufficiently small pump lateral size) would allow increasing the excitation density with a minimum number of spurious photoelectrons due to the pump hitting the edges. In addition to monitoring the dependence of the response on the excitation density, this possibility would grant access to a regime where the perturbation is stronger and possibly a different relaxation mechanism sets in.

The dynamics on CoSn reported in this thesis show no population redistribution from the flat band. This might be due to a lack of suitable states coupled to the flat band by one pump photon, in our case at 1.2 eV. Changing the photon energy could allow coupling to states above E_F and thus induce a non-thermal depopulation of the flat band, with potentially intriguing consequences on its dispersion modification. This could be performed at low pump fluences, to minimize thermal effects and obtain a predominance of the nonthermal excitation pathway. Direct visualization of the populated states above E_F can be obtained with two-photon photoemission.

An improved time resolution, together with the proven possibility of reaching large k values at 10.8 eV photon energy, would allow extending into the antinodal region the wealth of reported studies on the doping and temperature dependence of the electron dynamics in Bi2212. In the present configuration, the 10.8 eV setup employs 1.2 eV photons as a pump. Since a major part of the existing studies is conducted with a pump photon energy of about 1.5 eV, a higher photon energy would likely be beneficial for the size of the measured nonequilibrium effects and the comparability with previous experimental evidences closer to the node. Moreover, it is well known that specific photon energies can trigger highly unconventional phenomena in cuprates, as showcased by the signatures of light-induced superconductivity upon mid-infrared pumping [264]. The application of ARPES as a probe for the mechanisms responsible of these phenomena remains an unprecedented attempt, largely due to the technical challenge of generating the mid-infrared light, which requires large energy per pulse as input of an OPA, and transporting it to the photoemission chamber. Nonetheless, the possibility offered by TR-ARPES to access both the population and the band structure dynamics [19], in particular the gap dynamics up to the antinode, would give a decisive contribution to the understanding of the physical processes involved.

TR-XPS has proven effective with the reported measurements on the O $1s$ core level of Bi2212, but the technique presents wide regions of further applicability, even within the field of cuprates. Since our measurements reveal a prominent role of the planar oxygen in the charge redistribution, the response of the Cu-O plane would be completely mapped by inspection of the Cu $2p$ core level dynamics. This would also help assigning the observed response of the oxygen to specific intra-plane dynamics, where the charge-transfer interaction occurs. The Cu $2p$ core level lies at $\sim$930 eV binding energy, thus requiring almost 1 keV photon energy to be reached. Furthermore, our study was performed above the superconducting critical temperature. More underdoped samples would allow for a larger range of temperatures in which the pseudogap is observed, and a doping- and temperature-dependent study would allow verifying how the charge redistribution changes in the presence of different phases, namely the superconducting, the pseudogap and, in the heavily underdoped regime, the antiferromagnetic ordering. Also in this case, studying the dependence of the response as a function of the pump photon energy is expected to provide valuable insights in the transitions involved in cuprate nonequilibrium physics.

In conclusion, it was shown that the table-top 10.8 eV photon source is capable of significantly contributing to tackle open research questions regarding quantum materials of relevant interest, including topological insulators, kagome metals and high-temperature superconductors. The relevance of this source for the investigation of edge-cutting scientific

cases is expected to increase with the improvement of the time resolution and of the pump photon energy flexibility. Given the large applicability of TR-ARPES, the photon energy and the repetition rate provided by our novel source are applicable to several classes of quantum materials much beyond the ones explored in this thesis.

Appendix A

Determination of the Dirac point position in Bi_2Se_3

Figure A.1(a) shows the measurement along ΓM with *s*-polarized photons. In order to identify the Dirac point position in energy, we fit the dispersion of selected MDC cuts (10 meV integration window) above and below it. These can can be modeled with a single Lorentzian peak due to the convergence of the two TSS branches (Fig. A.1(b)). The Dirac point is assumed to be located at the energy where the MDC has the minimum FWHM (Fig. A.1(c)). In this way the theoretical and experimental energy scales are aligned and the dispersions can be compared. In the experimental data, the value of the Fermi level is extracted by fitting an oblique EDC cut along the TSS as prescribed in [265] (Fig. A.1(d)). The fitting function is composed by the Fermi-Dirac distribution convoluted with a Gaussian to account for the experimental resolution of ~ 80 meV.

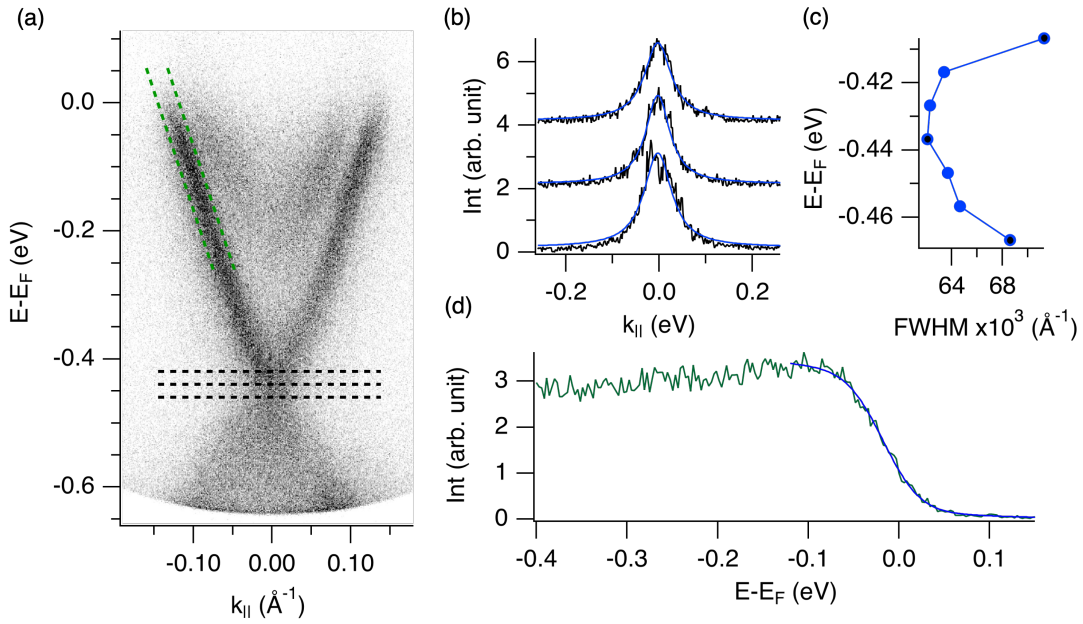

Figure A.1: (a) Dispersion measured along ΓM with *s*-polarized photons. (b) Selected MDC cuts taken in correspondence of the black dashed lines in panel (a). The blue line is the fit conducted as specified in the main text. (c) Lorentzian width of the MDC cuts as extracted from the fit. The examples reported in panel (b) are marked in black; the curve with lowest FWHM is among them and its energy is taken as the location of the Dirac point. (b) EDC integrated along the oblique path indicated with green dashed lines in panel (a), with superimposed the fit to extract the Fermi level (see main text).

Bibliography

[1] F. Giustino, J. H. Lee, F. Trier, M. Bibes, S. M. Winter, R. Valentí, Y.-W. Son, L. Taillefer, C. Heil, A. I. Figueroa, B. Plaçais, Q. Wu, O. V. Yazyev, E. P. A. M. Bakkers, J. Nygård, P. Forn-Díaz, S. D. Franceschi, J. W. McIver, L. E. F. F. Torres, T. Low, A. Kumar, R. Galceran, S. O. Valenzuela, M. V. Costache, A. Manchon, E.-A. Kim, G. R. Schleder, A. Fazzio, and S. Roche. "The 2021 quantum materials roadmap". In: *Journal of Physics: Materials* 3.4 (2020), p. 042006. DOI: 10.1088/2515-7639/abb74e (cit. on p. 1).

[2] B. Keimer and J. E. Moore. "The physics of quantum materials". In: *Nature Physics* 13.11 (2017), pp. 1045–1055. DOI: 10.1038/nphys4302 (cit. on p. 1).

[3] A. Damascelli, Z. Hussain, and Z.-X. Shen. "Angle-resolved photoemission studies of the cuprate superconductors". In: *Reviews of Modern Physics* 75.2 (2003), pp. 473–541. DOI: 10.1103/revmodphys.75.473 (cit. on pp. 1–2, 7–8, 10, 13, 69).

[4] S. Trebst and C. Hickey. "Kitaev materials". In: *Physics Reports* 950 (2022), pp. 1–37. DOI: 10.1016/j.physrep.2021.11.003 (cit. on p. 1).

[5] M. Z. Hasan and C. L. Kane. "*Colloquium*: Topological insulators". In: *Reviews of Modern Physics* 82.4 (2010), pp. 3045–3067. DOI: 10.1103/revmodphys.82.3045 (cit. on pp. 1, 39–40).

[6] T. Chowdhury, E. C. Sadler, and T. J. Kempa. "Progress and Prospects in Transition-Metal Dichalcogenide Research Beyond 2D". In: *Chemical Reviews* 120.22 (2020), pp. 12563–12591. DOI: 10.1021/acs.chemrev.0c00505 (cit. on p. 1).

[7] R. Cava, N. de Leon, and W. Xie. "Introduction: Quantum Materials". In: *Chemical Reviews* 121.5 (2021), pp. 2777–2779. DOI: 10.1021/acs.chemrev.0c01322 (cit. on p. 1).

[8] D. N. Basov, R. D. Averitt, and D. Hsieh. "Towards properties on demand in quantum materials". In: *Nature Materials* 16.11 (2017), pp. 1077–1088. DOI: 10.1038/nmat5017 (cit. on p. 1).

[9] W. Zhang, C. Hwang, C. L. Smallwood, T. L. Miller, G. Affeldt, K. Kurashima, C. Jozwiak, H. Eisaki, T. Adachi, Y. Koike, D.-H. Lee, and A. Lanzara. "Ultrafast quenching of electron–boson interaction and superconducting gap in a cuprate superconductor". In: *Nature Communications* 5.1 (2014). DOI: 10.1038/ncomms5959 (cit. on p. 2).

[10] G. Dresselhaus. "Spin-Orbit Coupling Effects in Zinc Blende Structures". In: *Physical Review* 100.2 (1955), pp. 580–586. DOI: 10.1103/physrev.100.580 (cit. on pp. 2, 44).

[11] R. Comin and A. Damascelli. "ARPES: A Probe of Electronic Correlations". In: *Strongly Correlated Systems: Experimental Techniques*. Ed. by A. Avella and F. Mancini. Berlin, Heidelberg: Springer Berlin Heidelberg, 2015, pp. 31–71. ISBN: 978-3-662-44133-6. DOI: 10.1007/978-3-662-44133-6_2. URL: https://doi.org/10.1007/978-3-662-44133-6_2 (cit. on pp. 2, 9).

[12] J. A. Sobota, Y. He, and Z.-X. Shen. "Angle-resolved photoemission studies of quantum materials". In: *Reviews of Modern Physics* 93.2 (2021), p. 025006. DOI: 10.1103/revmodphys.93.025006 (cit. on pp. 2, 7, 10–13).

[13] H. Zhang, T. Pincelli, C. Jozwiak, T. Kondo, R. Ernstorfer, T. Sato, and S. Zhou. "Angle-resolved photoemission spectroscopy". In: *Nature Reviews Methods Primers* 2.1 (2022). DOI: 10.1038/s43586-022-00133-7 (cit. on pp. 2, 7, 10–11, 15).

[14] C. Giannetti, M. Capone, D. Fausti, M. Fabrizio, F. Parmigiani, and D. Mihailovic. "Ultrafast optical spectroscopy of strongly correlated materials and high-temperature superconductors: a non-equilibrium approach". In: *Advances in Physics* 65.2 (2016), pp. 58–238. DOI: 10.1080/00018732.2016.1194044 (cit. on p. 2).

[15] K. Iwaya, M. Yokota, H. Hanada, H. Mogi, S. Yoshida, O. Takeuchi, Y. Miyatake, and H. Shigekawa. "Externally-triggerable optical pump-probe scanning tunneling microscopy with a time resolution of tens-picosecond". In: *Scientific Reports* 13.1 (2023). DOI: 10.1038/s41598-023-27383-z (cit. on p. 2).

[16] C. L. Smallwood, R. A. Kaindl, and A. Lanzara. "Ultrafast angle-resolved photoemission spectroscopy of quantum materials". In: *EPL (Europhysics Letters)* 115.2 (2016), p. 27001. DOI: 10.1209/0295-5075/115/27001 (cit. on pp. 2, 18, 75–76).

[17] S. Ponzoni, F. Paßlack, M. Stupar, D. M. Janas, G. Zamborlini, and M. Cinchetti. "Dirac Bands in the Topological Insulator Bi_2Se_3 Mapped by Time-Resolved Momentum Microscopy". In: *Advanced Physics Research* (2023), p. 2200016. DOI: 10.1002/apxr.202200016 (cit. on pp. 2, 42, 44, 52).

[18] M. X. Na, F. Boschini, A. K. Mills, M. Michiardi, R. P. Day, B. Zwartsenberg, G. Levy, S. Zhdanovich, A. F. Kemper, D. J. Jones, and A. Damascelli. "Establishing nonthermal regimes in pump-probe electron relaxation dynamics". In: *Physical Review B* 102.18 (2020), p. 184307. DOI: 10.1103/physrevb.102.184307 (cit. on p. 2).

[19] C. L. Smallwood, W. Zhang, T. L. Miller, G. Affeldt, K. Kurashima, C. Jozwiak, T. Noji, Y. Koike, H. Eisaki, D.-H. Lee, R. A. Kaindl, and A. Lanzara. "Influence of optically quenched superconductivity on quasiparticle relaxation rates in $Bi_2Sr_2CaCu_2O_{8+\delta}$". In: *Physical Review B* 92.16 (2015), p. 161102. DOI: 10.1103/physrevb.92.161102 (cit. on pp. 2, 72, 74, 97).

[20] X. Zhou, S. He, G. Liu, L. Zhao, L. Yu, and W. Zhang. "New developments in laser-based photoemission spectroscopy and its scientific applications: a key issues review". In: *Reports on Progress in Physics* 81.6 (2018), p. 062101. DOI: 10.1088/1361-6633/aab0cc (cit. on pp. 3, 11, 22–23).

[21] A. Gauthier, J. A. Sobota, N. Gauthier, K.-J. Xu, H. Pfau, C. R. Rotundu, Z.-X. Shen, and P. S. Kirchmann. "Tuning time and energy resolution in time-resolved photoemission spectroscopy with nonlinear crystals". In: *Journal of Applied Physics* 128.9 (2020), p. 093101. DOI: 10.1063/5.0018834 (cit. on pp. 3, 22, 34–35).

[22] H.-H. Jia, T.-T. Yeh, C.-M. Cheng, C.-W. Luo, M.-C. Chen, and P.-H. Lin. "Enhance high harmonic generation (HHG) efficiency via compact multi-plate continuum post-compression for time-resolved angle-resolved photoemission spectroscopy". In: *Review of Scientific Instruments* 94.5 (2023). DOI: 10.1063/5.0143089 (cit. on pp. 3, 34).

[23] D. Kutnyakhov, R. P. Xian, M. Dendzik, M. Heber, F. Pressacco, S. Y. Agustsson, L. Wenthaus, H. Meyer, S. Gieschen, G. Mercurio, A. Benz, K. Bühlman, S. Däster, R. Gort, D. Curcio, K. Volckaert, M. Bianchi, C. Sanders, J. A. Miwa, S. Ulstrup, A. Oelsner, C. Tusche, Y.-J. Chen, D. Vasilyev, K. Medjanik, G. Brenner, S. Dziarzhytski, H. Redlin, B. Manschwetus, S. Dong, J. Hauer, L. Rettig, F. Diekmann, K. Rossnagel, J. Demsar, H.-J. Elmers, P. Hofmann, R. Ernstorfer, G. Schönhense, Y. Acremann, and W. Wurth. "Time- and momentum-resolved photoemission studies using time-of-flight momentum microscopy at a free-electron laser". In: *Review of Scientific Instruments* 91.1 (2020), p. 013109. DOI: 10.1063/1.5118777 (cit. on pp. 3, 37).

[24] H. Hertz. "Ueber einen Einfluss des ultravioletten Lichtes auf die electrische Entladung". In: *Annalen der Physik und Chemie* 267.8 (1887), pp. 983–1000. DOI: 10.1002/andp.18872670827 (cit. on p. 5).

[25] A. Einstein. "Üer einen die Erzeugung und Verwandlung des Lichtes betreffenden heuristischen Gesichtspunkt". In: *Annalen der Physik* 322.6 (1905), pp. 132–148. DOI: 10.1002/andp.19053220607 (cit. on p. 5).

[26] S. Hüfner. *Photoelectron Spectroscopy*. Springer Berlin Heidelberg, 2003. DOI: 10.1007/978-3-662-09280-4 (cit. on pp. 5–7).

[27] M. Scholz. "Spin polarization, circular dichroism and robustness of topological surface states: a photoemission study". PhD thesis. Universität Potsdam, 2012 (cit. on p. 6).

[28] H. Iwasawa. "High-resolution angle-resolved photoemission spectroscopy and microscopy". In: *Electronic Structure* 2.4 (2020), p. 043001. DOI: 10.1088/2516-1075/abb379 (cit. on p. 6).

[29] J. B. Pendry. "The application of pseudopotentials to low-energy electron diffraction I. Calculation of the potential and 'inner potential'". In: *Journal of Physics C: Solid State Physics* 2.7 (1969), pp. 1215–1221. DOI: 10.1088/0022-3719/2/7/314 (cit. on p. 6).

[30] F. Himpsel. "Angle-resolved measurements of the photoemission of electrons in the study of solids". In: *Advances in Physics* 32.1 (1983), pp. 1–51. DOI: 10.1080/00018738300101521 (cit. on p. 6).

[31] N. W. Ashcroft and N. D. Mermin. *Solid State Physics*. Holt-Saunders, 1976 (cit. on p. 7).

[32] H. Li, X. Zhou, S. Parham, T. J. Reber, H. Berger, G. B. Arnold, and D. S. Dessau. "Coherent organization of electronic correlations as a mechanism to enhance and stabilize high-T_C cuprate superconductivity". In: *Nature Communications* 9.1 (2018). DOI: 10.1038/s41467-017-02422-2 (cit. on pp. 7–9).

[33] W. L. Schaich and N. W. Ashcroft. "Model Calculations in the Theory of Photoemission". In: *Physical Review B* 3.8 (1971), pp. 2452–2465. DOI: 10.1103/physrevb.3.2452 (cit. on p. 7).

[34] M. P. Seah and W. A. Dench. "Quantitative electron spectroscopy of surfaces: A standard data base for electron inelastic mean free paths in solids". In: *Surface and Interface Analysis* 1.1 (1979), pp. 2–11. DOI: 10.1002/sia.740010103 (cit. on p. 8).

[35] A. Damascelli. "Probing the Electronic Structure of Complex Systems by ARPES". In: *Physica Scripta* T109 (2004), p. 61. DOI: 10.1238/physica.topical.109a00061 (cit. on p. 8).

[36] Y. Cao, J. A. Waugh, X.-W. Zhang, J.-W. Luo, Q. Wang, T. J. Reber, S. K. Mo, Z. Xu, A. Yang, J. Schneeloch, G. D. Gu, M. Brahlek, N. Bansal, S. Oh, A. Zunger, and D. S. Dessau. "Mapping the orbital wavefunction of the surface states in three-dimensional topological insulators". In: *Nature Physics* 9.8 (2013), pp. 499–504. DOI: 10.1038/nphys2685 (cit. on pp. 8, 41, 46).

[37] J. K. Freericks, H. R. Krishnamurthy, and T. Pruschke. "Theoretical Description of Time-Resolved Photoemission Spectroscopy: Application to Pump-Probe Experiments". In: *Physical Review Letters* 102.13 (Mar. 30, 2009), p. 136401. DOI: 10.1103/physrevlett.102.136401 (cit. on pp. 9, 17).

[38] S. Doniach and E. H. Sondheimer. *Green's Functions for Solid State Physicists*. Published by Imperial College Press and distributed by World Scientific Publishing Co., 1998. DOI: 10.1142/p067 (cit. on p. 9).

[39] A. Altland and B. D. Simons. *Condensed Matter Field Theory*. Cambridge University Press, 2010. DOI: 10.1017/cbo9780511789984 (cit. on p. 9).

[40] L. D. Landau. "The Theory of a Fermi Liquid". In: *Zh. Eksp. Teor. Fiz.* 30.6 (1956), p. 1058 (cit. on p. 9).

[41] S. Suga, A. Sekiyama, G. Funabashi, J. Yamaguchi, M. Kimura, M. Tsujibayashi, T. Uyama, H. Sugiyama, Y. Tomida, G. Kuwahara, S. Kitayama, K. Fukushima, K. Kimura, T. Yokoi, K. Murakami, H. Fujiwara, Y. Saitoh, L. Plucinski, and C. M. Schneider. "High resolution, low hν photoelectron spectroscopy with the use of a microwave excited rare gas lamp and ionic crystal filters". In: *Review of Scientific Instruments* 81.10 (2010), p. 105111. DOI: 10.1063/1.3488367 (cit. on p. 10).

[42] F. Reinert and S. Hüner. "Photoemission spectroscopy - from early days to recent applications". In: *New Journal of Physics* 7 (2005), pp. 97–97. DOI: 10.1088/1367-2630/7/1/097 (cit. on p. 10).

[43] Y. Ishida, T. Otsu, A. Ozawa, K. Yaji, S. Tani, S. Shin, and Y. Kobayashi. "High repetition pump-and-probe photoemission spectroscopy based on a compact fiber laser system". In: *Review of Scientific Instruments* 87.12 (2016), p. 123902. DOI: 10.1063/1.4969053 (cit. on p. 11).

[44] Y. He, I. M. Vishik, M. Yi, S. Yang, Z. Liu, J. J. Lee, S. Chen, S. N. Rebec, D. Leuenberger, A. Zong, C. M. Jefferson, R. G. Moore, P. S. Kirchmann, A. J. Merriam, and Z.-X. Shen. "Invited Article: High resolution angle resolved photoemission with tabletop 11 eV laser". In: *Review of Scientific Instruments* 87.1 (2016), p. 011301. DOI: 10.1063/1.4939759 (cit. on p. 11).

[45] Y. Fu, K. Nishimura, R. Shao, A. Suda, K. Midorikawa, P. Lan, and E. J. Takahashi. "High efficiency ultrafast water-window harmonic generation for single-shot soft X-ray spectroscopy". In: *Communications Physics* 3.1 (2020). DOI: 10.1038/s42005-020-0355-x (cit. on p. 11).

[46] M. Kang, S. Fang, L. Ye, H. C. Po, J. Denlinger, C. Jozwiak, A. Bostwick, E. Rotenberg, E. Kaxiras, J. G. Checkelsky, and R. Comin. "Topological flat bands in frustrated kagome lattice CoSn". In: *Nature Communications* 11.1 (2020), p. 4004. DOI: 10.1038/s41467-020-17465-1 (cit. on pp. 11–12, 59–61, 63, 67).

[47] X. Sun, W.-T. Zhang, L. Zhao, G.-D. Liu, G.-D. Gu, Q.-J. Peng, Z.-M. Wang, S.-J. Zhang, F. Yang, C.-T. Chen, Z.-Y. Xu, and X.-J. Zhou. "Temperature Evolution of Energy Gap and Band Structure in the Superconducting and Pseudogap States of $Bi_2Sr_2CaCu_2O_{8+\delta}$ Superconductor Revealed by Laser-Based Angle-Resolved Photoemission Spectroscopy". In: *Chinese Physics Letters* 35.1 (2018), p. 017401. DOI: 10.1088/0256-307x/35/1/017401 (cit. on p. 12).

[48] H. Fellner-Feldegg, U. Gelius, B. Wannberg, A. Nilsson, E. Basilier, and K. Siegbahn. "New developments in ESCA-instrumentation". In: *Journal of Electron Spectroscopy and Related Phenomena* 5.1 (1974), pp. 643–689. DOI: 10.1016/0368-2048(74)85045-0 (cit. on p. 12).

[49] N. Mårtensson, P. Baltzer, P. Brühwiler, J.-O. Forsell, A. Nilsson, A. Stenborg, and B. Wannberg. "A very high resolution electron spectrometer". In: *Journal of Electron Spectroscopy and Related Phenomena* 70.2 (1994), pp. 117–128. DOI: 10.1016/0368-2048(94)02224-n (cit. on p. 12).

[50] A. Oelsner, M. Rohmer, C. Schneider, D. Bayer, G. Schöhense, and M. Aeschlimann. "Time- and energy resolved photoemission electron microscopy-imaging of photoelectron time-of-flight analysis by means of pulsed excitations". In: *Journal of Electron Spectroscopy and Related Phenomena* 178-179 (2010), pp. 317–330. DOI: 10.1016/j.elspec.2009.10.008 (cit. on p. 12).

[51] P. Kirchmann, L. Rettig, D. Nandi, U. Lipowski, M. Wolf, and U. Bovensiepen. "A time-of-flight spectrometer for angle-resolved detection of low energy electrons in two dimensions". In: *Applied Physics A* 91.2 (2008), pp. 211–217. DOI: 10.1007/s00339-008-4422-5 (cit. on p. 13).

[52] R. Ovsyannikov, P. Karlsson, M. Lundqvist, C. Lupulescu, W. Eberhardt, A. Föhlisch, S. Svensson, and N. Mårtensson. "Principles and operation of a new type of electron spectrometer-ArTOF". In: *Journal of Electron Spectroscopy and Related Phenomena* 191 (2013), pp. 92–103. DOI: 10.1016/j.elspec.2013.08.005 (cit. on p. 13).

[53] G. Schönhense, D. Kutnyakhov, F. Pressacco, M. Heber, N. Wind, S. Y. Agustsson, S. Babenkov, D. Vasilyev, O. Fedchenko, S. Chernov, L. Rettig, B. Schönhense, L. Wenthaus, G. Brenner, S. Dziarzhytski, S. Palutke, S. K. Mahatha, N. Schirmel, H. Redlin, B. Manschwetus, I. Hartl, Y. Matveyev, A. Gloskovskii, C. Schlueter, V. Shokeen, H. Duerr, T. K. Allison, M. Beye, K. Rossnagel, H. J. Elmers, and K. Medjanik. "Suppression of the vacuum space-charge effect in fs-photoemission by a retarding electrostatic front lens". In: *Review of Scientific Instruments* 92.5 (2021), p. 053703. ISSN: 0034-6748. DOI: 10.1063/5.0046567. URL: https://aip.scitation.org/doi/abs/10.1063/5.0046567 (cit. on pp. 13–14).

[54] G. Schöhense, A. Oelsner, O. Schmidt, G. H. Fecher, V. Mergel, O. Jagutzki, and H. Schmidt-Böking. "Time-of-flight photoemission electron microscopy a new way to chemical surface analysis". In: *Surface Science* 480.3 (2001), pp. 180–187. DOI: 10.1016/s0039-6028(01)00833-0 (cit. on p. 13).

[55] O. Karni, I. Esin, and K. M. Dani. "Through the Lens of a Momentum Microscope: Viewing Light-Induced Quantum Phenomena in 2D Materials". In: *Advanced Materials* (2022), p. 2204120. DOI: 10.1002/adma.202204120 (cit. on p. 14).

[56] S. Hellmann, K. Rossnagel, M. Marczynski-Bülow, and L. Kipp. "Vacuum space-charge effects in solid-state photoemission". In: *Physical Review B* 79.3 (2009), p. 035402. DOI: 10.1103/physrevb.79.035402 (cit. on p. 14).

[57] M. Dell'Angela, T. Anniyev, M. Beye, R. Coffee, A. Föhlisch, J. Gladh, S. Kaya, T. Katayama, O. Krupin, A. Nilsson, D. Nordlund, W. F. Schlotter, J. A. Sellberg, F. Sorgenfrei, J. J. Turner, H. Öström, H. Ogasawara, M. Wolf, and W. Wurth. "Vacuum space charge effects in sub-picosecond soft X-ray photoemission on a molecular adsorbate layer". In: *Structural Dynamics* 2.2 (2015), p. 025101. DOI: 10.1063/1.4914892 (cit. on pp. 14, 19, 37, 90).

[58] J. Maklar, S. Dong, S. Beaulieu, T. Pincelli, M. Dendzik, Y. W. Windsor, R. P. Xian, M. Wolf, R. Ernstorfer, and L. Rettig. "A quantitative comparison of time-of-flight momentum microscopes and hemispherical analyzers for time- and angle-resolved photoemission spectroscopy experiments". In: *Review of Scientific Instruments* 91.12 (2020), p. 123112. DOI: 10.1063/5.0024493 (cit. on pp. 14–15).

[59] G. Schönhense and H.-J. Elmers. "Spin- and time-resolved photoelectron spectroscopy and diffraction studies using time-of-flight momentum microscopes". In: *Journal of Vacuum Science & Technology A* 40.2 (2022), p. 020802. DOI: 10.1116/6.0001500 (cit. on p. 15).

[60] G. Schönhense, K. Medjanik, C. Tusche, M. de Loos, B. van der Geer, M. Scholz, F. Hieke, N. Gerken, J. Kirschner, and W. Wurth. "Correction of the deterministic part of space-charge interaction in momentum microscopy of charged particles". In: *Ultramicroscopy* 159 (2015), pp. 488–496. DOI: 10.1016/j.ultramic.2015.05.015 (cit. on p. 15).

[61] D. A. Shirley. "High-Resolution X-Ray Photoemission Spectrum of the Valence Bands of Gold". In: *Physical Review B* 5.12 (1972), pp. 4709–4714. DOI: 10.1103/physrevb.5.4709 (cit. on pp. 15, 87).

[62] A. F. Kemper, M. A. Sentef, B. Moritz, J. K. Freericks, and T. P. Devereaux. "Effect of dynamical spectral weight redistribution on effective interactions in time-resolved spectroscopy". In: *Physical Review B* 90.7 (Aug. 14, 2014), p. 075126. DOI: 10.1103/physrevb.90.075126 (cit. on p. 17).

[63] J. Freericks and A. F. Kemper. "What do the two times in two-time correlation functions mean for interpreting tr-ARPES?" In: *Journal of Electron Spectroscopy and Related Phenomena* 251 (July 24, 2021), p. 147104. DOI: 10.1016/j.elspec.2021.147104 (cit. on p. 17).

[64] J. A. Sobota, S.-L. Yang, D. Leuenberger, A. Kemper, J. Analytis, I. Fisher, P. S. Kirchmann, T. P. Devereaux, and Z.-X. Shen. "Distinguishing Bulk and Surface Electron-Phonon Coupling in the Topological Insulator Bi_2Se_3 Using Time-Resolved Photoemission Spectroscopy". In: *Physical Review Letters* 113.15 (2014), p. 157401. DOI: 10.1103/physrevlett.113.157401 (cit. on p. 18).

[65] I. Avigo, R. Cortés, L. Rettig, S. Thirupathaiah, H. S. Jeevan, P. Gegenwart, T. Wolf, M. Ligges, M. Wolf, J. Fink, and U. Bovensiepen. "Coherent excitations and electron-phonon coupling in $Ba/EuFe_2As_2$ compounds investigated by femtosecond time- and angle-resolved photoemission spectroscopy". In: *Journal of Physics: Condensed Matter* 25.9 (2013), p. 094003. DOI: 10.1088/0953-8984/25/9/094003 (cit. on p. 18).

[66] F. Boschini, E. H. da Silva Neto, E. Razzoli, M. Zonno, S. Peli, R. P. Day, M. Michiardi, M. Schneider, B. Zwartsenberg, P. Nigge, R. D. Zhong, J. Schneeloch, G. D. Gu, S. Zhdanovich, A. K. Mills, G. Levy, D. J. Jones, C. Giannetti, and A. Damascelli. "Collapse of superconductivity in cuprates via ultrafast quenching of phase coherence". In: *Nature Materials* 17.5 (2018), pp. 416–420. DOI: 10.1038/s41563-018-0045-1 (cit. on p. 18).

[67] F. Schmitt, P. S. Kirchmann, U. Bovensiepen, R. G. Moore, L. Rettig, M. Krenz, J.-H. Chu, N. Ru, L. Perfetti, D. H. Lu, M. Wolf, I. R. Fisher, and Z.-X. Shen. "Transient Electronic Structure and Melting of a Charge Density Wave in $TbTe_3$". In: *Science* 321.5896 (2008), pp. 1649–1652. DOI: 10.1126/science.1160778 (cit. on p. 18).

[68] C. Giannetti, G. Coslovich, F. Cilento, G. Ferrini, H. Eisaki, N. Kaneko, M. Greven, and F. Parmigiani. "Discontinuity of the ultrafast electronic response of underdoped superconducting $Bi_2Sr_2CaCu_2O_{8+\delta}$ strongly excited by ultrashort light pulses". In: *Physical Review B* 79.22 (2009), p. 224502. DOI: 10.1103/physrevb.79.224502 (cit. on pp. 18, 71).

[69] V. R. Morrison, R. P. Chatelain, K. L. Tiwari, A. Hendaoui, A. Bruhács, M. Chaker, and B. J. Siwick. "A photoinduced metal-like phase of monoclinic VO_2 revealed by ultrafast electron diffraction". In: *Science* 346.6208 (2014), pp. 445–448. DOI: 10.1126/science.1253779 (cit. on p. 18).

[70] F. Boschini, D. Bugini, M. Zonno, M. Michiardi, R. P. Day, E. Razzoli, B. Zwartsenberg, M. Schneider, E. H. da Silva Neto, S. dal Conte, S. K. Kushwaha, R. J. Cava, S. Zhdanovich, A. K. Mills, G. Levy, E. Carpene, C. Dallera, C. Giannetti, D. J. Jones, G. Cerullo, and A. Damascelli. "Role of matrix elements in the time-resolved photoemission signal". In: *New Journal of Physics* 22.2 (2020), p. 023031. DOI: 10.1088/1367-2630/ab6eb1 (cit. on pp. 18, 52).

[71] C. Rullière, ed. *Femtosecond Laser Pulses*. Springer Berlin Heidelberg, 1998. DOI: 10.1007/978-3-662-03682-2 (cit. on p. 19).

[72] L.-P. Oloff, M Oura, K Rossnagel, A Chainani, M Matsunami, R Eguchi, T Kiss, Y Nakatani, T Yamaguchi, J Miyawaki, M Taguchi, K Yamagami, T Togashi, T Katayama, K Ogawa, M Yabashi, and T Ishikawa. "Time-resolved HAXPES at SACLA: probe and pump pulse-induced space-charge effects". In: *New Journal of Physics* 16.12 (2014), p. 123045. DOI: 10.1088/1367-2630/16/12/123045 (cit. on pp. 19, 90).

[73] S Hellmann, C Sohrt, M Beye, T Rohwer, F Sorgenfrei, M Marczynski-Bühlow, M Kalläne, H Redlin, F Hennies, M Bauer, A Fölisch, L Kipp, W Wurth, and K Rossnagel. "Time-resolved x-ray photoelectron spectroscopy at FLASH". In: *New Journal of Physics* 14.1 (Jan. 30, 2012), p. 013062. DOI: 10.1088/1367-2630/14/1/013062 (cit. on pp. 19, 35–36).

[74] G. P. Segre, N. Gedik, J. Orenstein, D. A. Bonn, R. Liang, and W. N. Hardy. "Photoinduced Changes of Reflectivity in Single Crystals of $YBa_2Cu_3O_{6.5}$ (Ortho II)". In: *Physical Review Letters* 88.13 (2002), p. 137001. DOI: 10.1103/physrevlett.88.137001 (cit. on p. 20).

[75] N. Gedik, P. Blake, R. C. Spitzer, J. Orenstein, R. Liang, D. A. Bonn, and W. N. Hardy. "Single-quasiparticle stability and quasiparticle-pair decay in $YBa_2Cu_3O_{6.5}$". In: *Physical Review B* 70.1 (2004), p. 014504. DOI: 10.1103/physrevb.70.014504 (cit. on p. 20).

[76] A. Rothwarf and B. N. Taylor. "Measurement of Recombination Lifetimes in Superconductors". In: *Physical Review Letters* 19.1 (1967), pp. 27–30. DOI: 10.1103/physrevlett.19.27 (cit. on p. 20).

[77] A. Crepaldi, B. Ressel, F. Cilento, M. Zacchigna, C. Grazioli, H. Berger, P. Bugnon, K. Kern, M. Grioni, and F. Parmigiani. "Ultrafast photodoping and effective Fermi-Dirac distribution of the Dirac particles in Bi_2Se_3". In: *Physical Review B* 86.20 (2012), p. 205133. DOI: 10.1103/physrevb.86.205133 (cit. on pp. 20, 52, 58).

[78] A. Yariv and P. Yeh. *Optical Waves in Crystals. Propagation and Control of Laser Radiation (Wiley Series in Pure and Applied Optics)*. Wiley-Interscience, 2002, p. 608. ISBN: 978-0-471-43081-0 (cit. on pp. 21–22).

[79] R. W. Boyd. *Nonlinear optics*. Academic Press, 2008, p. 613. ISBN: 9780123694706 (cit. on pp. 21–22, 28).

[80] G. Tamosauskas, G. Beresnevicius, D. Gadonas, and A. Dubietis. "Transmittance and phase matching of BBO crystal in the 3-5 μm range and its application for the characterization of mid-infrared laser pulses". In: *Optical Materials Express* 8.6 (2018), p. 1410. DOI: 10.1364/ome.8.001410 (cit. on p. 22).

[81] F. Reintjes. *Nonlinear optical parametric processes in liquids and gases*. Elsevier Science And Technology Books, 1984. ISBN: 9780323148900 (cit. on pp. 23–25).

[82] L. Zych and J. Young. "Limitation of 3547 to 1182 Å conversion efficiency in Xe". In: *Institute of Electrical and Electronics Engineers (IEEE)* 14.3 (1978), pp. 147–149. DOI: 10.1109/jqe.1978.1069763 (cit. on pp. 23–25).

[83] G. Bjorklund. "Effects of focusing on third-order nonlinear processes in isotropic media". In: *IEEE Journal of Quantum Electronics* 11.6 (1975), pp. 287–296. DOI: 10.1109/jqe.1975.1068619 (cit. on p. 23).

[84] J. Kutzner, G. Tsilimis, and H. Zacharias. "Harmonic generation in the discrete spectral region of xenon using broadband femtosecond laser pulses". In: *Applied Physics B* 80.2 (2005), pp. 203–210. DOI: 10.1007/s00340-004-1709-x (cit. on p. 24).

[85] Z. Zhao and Y. Kobayashi. "Realization of a mW-level 10.7-eV (λ = 115.6 nm) laser by cascaded third harmonic generation of a Yb:fiber CPA laser at 1-MHz". In: *Opt. Express* 25.12 (2017), pp. 13517–13526. DOI: 10.1364/OE.25.013517 (cit. on pp. 24, 28).

[86] S. Hädrich, M. Krebs, A. Hoffmann, A. Klenke, J. Rothhardt, J. Limpert, and A. Tünnermann. "Exploring new avenues in high repetition rate table-top coherent extreme ultraviolet sources". In: *Light: Science & Applications* 4.8 (2015), e320–e320. DOI: 10.1038/lsa.2015.93 (cit. on p. 24).

[87] T. Munakata, T. Masuda, N. Ueno, A. Abdureyim, and Y. Sonoda. "Time-resolved photoemission microspectroscopy based on fs-VUV laser light". In: *Surface Science* 507-510 (2002), pp. 434–440. DOI: 10.1016/s0039-6028(02)01282-7 (cit. on p. 24).

[88] M. H. Berntsen, O. Götberg, and O. Tjernberg. "An experimental setup for high resolution 10.5 eV laser-based angle-resolved photoelectron spectroscopy using a time-of-flight electron analyzer". In: *Review of Scientific Instruments* 82.9 (2011), p. 095113. DOI: 10.1063/1.3637464 (cit. on pp. 24, 28).

[89] R. Mahon, T. McIlrath, V. Myerscough, and D. Koopman. "Third-harmonic generation in argon, krypton, and xenon: Bandwidth limitations in the vicinity of Lyman-α". In: *IEEE Journal of Quantum Electronics* 15.6 (1979), pp. 444–451. DOI: 10.1109/jqe.1979.1070036 (cit. on pp. 25–26).

[90] F. Cilento, A. Crepaldi, G. Manzoni, A. Sterzi, M. Zacchigna, P. Bugnon, H. Berger, and F. Parmigiani. "Advancing non-equilibrium ARPES experiments by a 9.3 eV coherent ultrafast photon source". In: *Journal of Electron Spectroscopy and Related Phenomena* 207 (2016), pp. 7–13. DOI: 10.1016/j.elspec.2015.12.002 (cit. on p. 25).

[91] J. Kutzner and H. Zacharias. "VUV generation by frequency tripling the third harmonic of a picosecond kHz Nd:YLF laser in xenon and mercury vapour". In: *Applied Physics B* 66.5 (1998), pp. 571–577. DOI: 10.1007/s003400050437 (cit. on p. 25).

[92] H. Iwasawa, H. Takita, K. Goto, W. Mansuer, T. Miyashita, E. F. Schwier, A. Ino, K. Shimada, and Y. Aiura. "Accurate and efficient data acquisition methods for high-resolution angle-resolved photoemission microscopy". In: *Scientific Reports* 8.1 (2018). DOI: 10.1038/s41598-018-34894-7 (cit. on p. 27).

[93] K. Kawaguchi, K. Kuroda, Z. Zhao, S. Tani, A. Harasawa, Y. Fukushima, H. Tanaka, R. Noguchi, T. Iimori, K. Yaji, M. Fujisawa, S. Shin, F. Komori, Y. Kobayashi, and T. Kondo. *Time-, spin-, and angle-resolved photoemission spectroscopy with a 1-MHz 10.7-eV pulse laser*. 2023. DOI: 10.48550/ARXIV.2303.16466 (cit. on pp. 29, 33, 38).

[94] F. Cilento, S. D. Conte, G. Coslovich, S. Peli, N. Nembrini, S. Mor, F. Banfi, G. Ferrini, H. Eisaki, M. K. Chan, C. J. Dorow, M. J. Veit, M. Greven, D. van der Marel, R. Comin, A. Damascelli, L. Rettig, U. Bovensiepen, M. Capone, C. Giannetti, and F. Parmigiani. "Photo-enhanced antinodal conductivity in the pseudogap state of high-T_c cuprates". In: *Nature Communications* 5.1 (2014). DOI: 10.1038/ncomms5353 (cit. on pp. 30, 70–71).

[95] S. Peli, D. Puntel, D. Kopic, B. Sockol, F. Parmigiani, and F. Cilento. "Time-resolved VUV ARPES at 10.8 eV photon energy and MHz repetition rate". In: *Journal of Electron Spectroscopy and Related Phenomena* 243 (2020), p. 146978. DOI: 10.1016/j.elspec.2020.146978 (cit. on pp. 31–32, 38, 93).

[96] Y. Xu, R. Wang, S. Ma, L. Zhou, Y. R. Shen, and C. Tian. "Theoretical analysis and simulation of pulsed laser heating at interface". In: *Journal of Applied Physics* 123.2 (2018), p. 025301. DOI: 10.1063/1.5008963 (cit. on p. 31).

[97] P. B. Corkum. "Plasma perspective on strong field multiphoton ionization". In: *Physical Review Letters* 71.13 (1993), pp. 1994–1997. DOI: 10.1103/physrevlett.71.1994 (cit. on p. 33).

[98] R. Cucini, T. Pincelli, G. Panaccione, D. Kopic, F. Frassetto, P. Miotti, G. M. Pierantozzi, S. Peli, A. Fondacaro, A. D. Luisa, A. D. Vita, P. Carrara, D. Krizmancic, D. T. Payne, F. Salvador, A. Sterzi, L. Poletto, F. Parmigiani, G. Rossi, and F. Cilento. "Coherent narrowband light source for ultrafast photoelectron spectroscopy in the 17–31 eV photon energy range". In: *Structural Dynamics* 7.1 (2020), p. 014303. DOI: 10.1063/1.5131216 (cit. on p. 34).

[99] A. K. Mills, T. J. Hammond, M. H. C. Lam, and D. J. Jones. "XUV frequency combs via femtosecond enhancement cavities". In: *Journal of Physics B: Atomic, Molecular and Optical Physics* 45.14 (July 4, 2012), p. 142001. DOI: 10.1088/0953-4075/45/14/142001 (cit. on p. 34).

[100] Z. Chang. *Fundamentals of Attosecond Optics*. CRC Press, 2016. DOI: 10.1201/b10402 (cit. on p. 34).

[101] M. Puppin, Y. Deng, C. W. Nicholson, J. Feldl, N. B. M. Schröter, H. Vita, P. S. Kirchmann, C. Monney, L. Rettig, M. Wolf, and R. Ernstorfer. "Time- and angle-resolved photoemission spectroscopy of solids in the extreme ultraviolet at 500 kHz repetition rate". In: *Review of Scientific Instruments* 90.2 (Feb. 12, 2019), p. 023104. DOI: 10.1063/1.5081938 (cit. on p. 34).

[102] C. Steier, P. Heimann, S. Marks, D. Robin, R. Schoenlein, W. Wan, and W. Wittmer. "Successful completion of the femtosecond slicing upgrade at the ALS". In: *2007 IEEE Particle Accelerator Conference (PAC)*. IEEE, 2007. DOI: 10.1109/pac.2007.4441027 (cit. on pp. 35–36).

[103] E. L. Saldin, E. A. Schneidmiller, and M. V. Yurkov. *The Physics of Free Electron Lasers*. Springer Berlin Heidelberg, 2000. DOI: 10.1007/978-3-662-04066-9 (cit. on p. 35).

[104] P. K. Maroju, C. Grazioli, M. D. Fraia, M. Moioli, D. Ertel, H. Ahmadi, O. Plekan, P. Finetti, E. Allaria, L. Giannessi, G. D. Ninno, C. Spezzani, G. Penco, S. Spampinati, A. Demidovich, M. B. Danailov, R. Borghes, G. Kourousias, C. E. S. D. Reis, F. Billé, A. A. Lutman, R. J. Squibb, R. Feifel, P. Carpeggiani, M. Reduzzi, T. Mazza, M. Meyer, S. Bengtsson, N. Ibrakovic, E. R. Simpson, J. Mauritsson, T. Csizmadia, M. Dumergue, S. Kühn, H. N. Gopalakrishna, D. You, K. Ueda, M. Labeye, J. E. Bækhøj, K. J. Schafer, E. V. Gryzlova, A. N. Grum-Grzhimailo, K. C. Prince, C. Callegari, and G. Sansone. "Attosecond pulse shaping using a seeded free-electron laser". In: *Nature* 578.7795 (2020), pp. 386–391. DOI: 10.1038/s41586-020-2005-6 (cit. on pp. 36, 84).

[105] L. Wenthaus. *Laser-Assisted Photoemission from Solids with Free Electron Lasers*. Verlag Dr. Hut, 2018. ISBN: ISBN 978-3-843 -3803-7 (cit. on p. 36).

[106] S. Kunisada, S. Isono, Y. Kohama, S. Sakai, C. Bareille, S. Sakuragi, R. Noguchi, K. Kurokawa, K. Kuroda, Y. Ishida, S. Adachi, R. Sekine, T. K. Kim, C. Cacho, S. Shin, T. Tohyama, K. Tokiwa, and T. Kondo. "Observation of small Fermi pockets protected by clean CuO_2 subsheets of a high T_C superconductor". In: *Science* 369.6505 (2020), pp. 833–838. DOI: 10.1126/science.aay7311 (cit. on p. 36).

[107] M. Schüler, T. Pincelli, S. Dong, T. P. Devereaux, M. Wolf, L. Rettig, R. Ernstorfer, and S. Beaulieu. "Polarization-Modulated Angle-Resolved Photoemission Spectroscopy: Toward Circular Dichroism without Circular Photons and Bloch Wave-function Reconstruction". In: *Physical Review X* 12.1 (2022), p. 011019. DOI: 10.1103/physrevx.12.011019 (cit. on p. 36).

[108] D. Curcio, S. Pakdel, K. Volckaert, J. A. Miwa, S. Ulstrup, N. Lanatà, M. Bianchi, D. Kutnyakhov, F. Pressacco, G. Brenner, S. Dziarzhytski, H. Redlin, S. Y. Agustsson, K. Medjanik, D. Vasilyev, H.-J. Elmers, G. Schönhense, C. Tusche, Y.-J. Chen, F. Speck, T. Seyller, K. Bühlmann, R. Gort, F. Diekmann, K. Rossnagel, Y. Acremann, J. Demsar, W. Wurth, D. Lizzit, L. Bignardi, P. Lacovig, S. Lizzit, C. E. Sanders, and P. Hofmann. "Ultrafast electronic linewidth broadening in the C 1s core level of graphene". In: *Physical Review B* 104.16 (2021), p. l161104. DOI: 10.1103/physrevb.104.l161104 (cit. on pp. 36, 83).

[109] M. Dendzik, R. P. Xian, E. Perfetto, D. Sangalli, D. Kutnyakhov, S. Dong, S. Beaulieu, T. Pincelli, F. Pressacco, D. Curcio, S. Y. Agustsson, M. Heber, J. Hauer, W. Wurth, G. Brenner, Y. Acremann, P. Hofmann, M. Wolf, A. Marini, G. Stefanucci, L. Rettig, and R. Ernstorfer. "Observation of an Excitonic Mott Transition Through Ultrafast Core-*cum*-Conduction Photoemission Spectroscopy". In: *Physical Review Letters* 125.9 (2020), p. 096401. DOI: 10.1103/physrevlett.125.096401 (cit. on pp. 36, 83).

[110] W. Ackermann, G. Asova, V. Ayvazyan, A. Azima, N. Baboi, J. Bähr, V. Balandin, B. Beutner, A. Brandt, A. Bolzmann, R. Brinkmann, O. I. Brovko, M. Castellano, P. Castro, L. Catani, E. Chiadroni, S. Choroba, A. Cianchi, J. T. Costello, D. Cubaynes, J. Dardis, W. Decking, H. Delsim-Hashemi, A. Delserieys, G. D. Pirro, M. Dohlus, S. Düterer, A. Eckhardt, H. T. Edwards, B. Faatz, J. Feldhaus, K. Flötmann, J. Frisch, L. Fröhlich, T. Garvey, U. Gensch, C. Gerth, M. Görler, N. Golubeva, H.-J. Grabosch, M. Grecki, O. Grimm, K. Hacker, U. Hahn, J. H. Han, K. Honkavaara, T. Hott, M. Hüing, Y. Ivanisenko, E. Jaeschke, W. Jalmuzna, T. Jezynski, R. Kammering, V. Katalev, K. Kavanagh, E. T. Kennedy, S. Khodyachykh, K. Klose, V. Kocharyan, M. Köfer, M. Kollewe, W. Koprek, S. Korepanov, D. Kostin, M. Krassilnikov, G. Kube, M. Kuhlmann, C. L. S. Lewis, L. Lilje, T. Limberg, D. Lipka, F. Löhl, H. Luna, M. Luong, M. Martins, M. Meyer, P. Michelato, V. Miltchev, W. D. Möller, L. Monaco, W. F. O. Müller, O. Napieralski, O. Napoly, P. Nicolosi, D. Nölle, T. Nuñez, A. Oppelt, C. Pagani, R. Paparella, N. Pchalek, J. Pedregosa-Gutierrez, B. Petersen, B. Petrosyan, G. Petrosyan, L. Petrosyan, J. Pflüger, E. Plöjes, L. Poletto, K. Pozniak, E. Prat, D. Proch, P. Pucyk, P. Radcliffe, H. Redlin, K. Rehlich, M. Richter, M. Roehrs, J. Roensch, R. Romaniuk, M. Ross, J. Rossbach, V. Rybnikov, M. Sachwitz, E. L. Saldin, W. Sandner, H. Schlarb, B. Schmidt, M. Schmitz, P. Schmüser, J. R. Schneider, E. A. Schneidmiller, S. Schnepp, S. Schreiber, M. Seidel, D. Sertore, A. V. Shabunov, C. Simon, S. Simrock, E. Sombrowski, A. A. Sorokin, P. Spanknebel, R. Spesyvtsev, L. Staykov, B. Steffen, F. Stephan, F. Stulle, H. Thom, K. Tiedtke, M. Tischer, S. Toleikis, R. Treusch, D. Trines, I. Tsakov, E. Vogel, T. Weiland, H. Weise, M. Wellhöfer, M. Wendt, I. Will, A. Winter, K. Wittenburg, W. Wurth, P. Yeates, M. V. Yurkov,

I. Zagorodnov, and K. Zapfe. "Operation of a free-electron laser from the extreme ultraviolet to the water window". In: *Nature Photonics* 1.6 (2007), pp. 336–342. DOI: 10.1038/nphoton.2007.76 (cit. on p. 36).

[111] M. Seidel, F. Pressacco, O. Akcaalan, T. Binhammer, J. Darvill, N. Ekanayake, M. Frede, U. Grosse-Wortmann, M. Heber, C. M. Heyl, D. Kutnyakhov, C. Li, C. Mohr, J. Müller, O. Puncken, H. Redlin, N. Schirmel, S. Schulz, A. Swiderski, H. Tavakol, H. Tünnermann, C. Vidoli, L. Wenthaus, N. Wind, L. Winkelmann, B. Manschwetus, and I. Hartl. "Ultrafast MHz-Rate Burst-Mode Pump–Probe Laser for the FLASH FEL Facility Based on Nonlinear Compression of ps-Level Pulses from an Yb-Amplifier Chain". In: *Laser and Photonics Reviews* 16.3 (2022), p. 2100268. DOI: 10.1002/lpor.202100268. arXiv: 2105.05882 (cit. on p. 37).

[112] S. Schulz, I. Grguraš, C. Behrens, H. Bromberger, J. T. Costello, M. K. Czwalinna, M. Felber, M. C. Hoffmann, M. Ilchen, H. Y. Liu, T. Mazza, M. Meyer, S. Pfeiffer, P. Prędki, S. Schefer, C. Schmidt, U. Wegner, H. Schlarb, and A. L. Cavalieri. "Femtosecond all-optical synchronization of an X-ray free-electron laser". In: *Nature Communications* 6.1 (2015). DOI: 10.1038/ncomms6938 (cit. on p. 37).

[113] K. Baumgärtner, M. Reuner, C. Metzger, D. Kutnyakhov, M. Heber, F. Pressacco, C.-H. Min, T. R. F. Peixoto, M. Reiser, C. Kim, W. Lu, R. Shayduk, M. Izquierdo, G. Brenner, F. Roth, A. Schöll, S. Molodtsov, W. Wurth, F. Reinert, A. Madsen, D. Popova-Gorelova, and M. Scholz. "Ultrafast orbital tomography of a pentacene film using time-resolved momentum microscopy at a FEL". In: *Nature Communications* 13.1 (2022). DOI: 10.1038/s41467-022-30404-6 (cit. on p. 37).

[114] R. P. Xian, Y. Acremann, S. Y. Agustsson, M. Dendzik, K. Bühlmann, D. Curcio, D. Kutnyakhov, F. Pressacco, M. Heber, S. Dong, T. Pincelli, J. Demsar, W. Wurth, P. Hofmann, M. Wolf, M. Scheidgen, L. Rettig, and R. Ernstorfer. "An open-source, end-to-end workflow for multidimensional photoemission spectroscopy". In: *Scientific Data* 7.1 (2020). DOI: 10.1038/s41597-020-00769-8 (cit. on pp. 37, 83).

[115] C. Lee, T. Rohwer, E. J. Sie, A. Zong, E. Baldini, J. Straquadine, P. Walmsley, D. Gardner, Y. S. Lee, I. R. Fisher, and N. Gedik. "High resolution time- and angle-resolved photoemission spectroscopy with 11 eV laser pulses". In: *Review of Scientific Instruments* 91.4 (2020), p. 043102. DOI: 10.1063/1.5139556 (cit. on pp. 38, 95).

[116] X.-G. Wen. "Topological orders and edge excitations in fractional quantum Hall states". In: *Advances in Physics* 44.5 (1995), pp. 405–473. DOI: 10.1080/00018739500101566 (cit. on p. 39).

[117] M. Nakahara. *Geometry, topology and physics*. 2003. ISBN: ISBN 9780750306065 (cit. on p. 39).

[118] M. V. Berry. "Quantal phase factors accompanying adiabatic changes". In: *Proceedings of the Royal Society of London. A. Mathematical and Physical Sciences* 392.1802 (1984), pp. 45–57. DOI: 10.1098/rspa.1984.0023 (cit. on p. 40).

[119] D. Xiao, M.-C. Chang, and Q. Niu. "Berry phase effects on electronic properties". In: *Reviews of Modern Physics* 82.3 (2010), pp. 1959–2007. DOI: 10.1103/revmodphys.82.1959 (cit. on p. 40).

[120] C. L. Kane and E. J. Mele. "A New Spin on the Insulating State". In: *Science* 314.5806 (2006), pp. 1692–1693. DOI: 10.1126/science.1136573 (cit. on p. 40).

[121] A. Bansil, H. Lin, and T. Das. "*Colloquium*: Topological band theory". In: *Reviews of Modern Physics* 88.2 (2016), p. 021004. DOI: 10.1103/revmodphys.88.021004 (cit. on pp. 40–41).

[122] C. L. Kane and E. J. Mele. "Z_2 tpological order and the quantum spin Hall effect". In: *Physical Review Letters* 95.14 (2005), p. 146802. DOI: 10.1103/physrevlett.95.146802 (cit. on pp. 40–41).

[123] X.-L. Qi and S.-C. Zhang. "Topological insulators and superconductors". In: *Reviews of Modern Physics* 83.4 (2011), pp. 1057–1110. DOI: 10.1103/revmodphys.83.1057 (cit. on p. 40).

[124] D. P. DiVincenzo and E. J. Mele. "Self-consistent effective-mass theory for intralayer screening in graphite intercalation compounds". In: *Physical Review B* 29.4 (1984), pp. 1685–1694. DOI: 10.1103/physrevb.29.1685 (cit. on p. 41).

[125] L. Fu, C. L. Kane, and E. J. Mele. "Topological Insulators in Three Dimensions". In: *Physical Review Letters* 98.10 (2007), p. 106803. DOI: 10.1103/physrevlett.98.106803 (cit. on p. 41).

[126] C. L. Kane and E. J. Mele. "Quantum Spin Hall Effect in Graphene". In: *Physical Review Letters* 95.22 (2005), p. 226801. DOI: 10.1103/physrevlett.95.226801 (cit. on p. 41).

[127] M. König, S. Wiedmann, C. Bruüne, A. Roth, H. Buhmann, L. W. Molenkamp, X.-L. Qi, and S.-C. Zhang. "Quantum Spin Hall Insulator State in HgTe Quantum Wells". In: *Science* 318.5851 (2007), pp. 766–770. DOI: 10.1126/science.1148047 (cit. on p. 41).

[128] D. Hsieh, D. Qian, L. Wray, Y. Xia, Y. S. Hor, R. J. Cava, and M. Z. Hasan. "A topological Dirac insulator in a quantum spin Hall phase". In: *Nature* 452.7190 (2008), pp. 970–974. DOI: 10.1038/nature06843 (cit. on p. 41).

[129] Y. S. Hor, A. Richardella, P. Roushan, Y. Xia, J. G. Checkelsky, A. Yazdani, M. Z. Hasan, N. P. Ong, and R. J. Cava. "p-type Bi_2 Se_3 for topological insulator and low-temperature thermoelectric applications". In: *Physical Review B* 79.19 (2009), p. 195208. DOI: 10.1103/physrevb.79.195208 (cit. on p. 41).

[130] Y. L. Chen, J. G. Analytis, J.-H. Chu, Z. K. Liu, S.-K. Mo, X. L. Qi, H. J. Zhang, D. H. Lu, X. Dai, Z. Fang, S. C. Zhang, I. R. Fisher, Z. Hussain, and Z.-X. Shen. "Experimental Realization of a Three-Dimensional Topological Insulator, Bi_2Te_3". In: *Science* 325.5937 (2009), pp. 178–181. DOI: 10.1126/science.1173034 (cit. on pp. 41, 43).

[131] D. Hsieh, Y. Xia, D. Qian, L. Wray, F. Meier, J. H. Dil, J. Osterwalder, L. Patthey, A. V. Fedorov, H. Lin, A. Bansil, D. Grauer, Y. S. Hor, R. J. Cava, and M. Z. Hasan. "Observation of Time-Reversal-Protected Single-Dirac-Cone Topological-Insulator States in Bi_2Te_3 and Sb_2Te_3". In: *Physical Review Letters* 103.14 (2009), p. 146401. DOI: 10.1103/physrevlett.103.146401 (cit. on p. 41).

[132] H. Zhang, C.-X. Liu, X.-L. Qi, X. Dai, Z. Fang, and S.-C. Zhang. "Topological insulators in Bi2Se3, Bi2Te3 and Sb2Te3 with a single Dirac cone on the surface". In: *Nature Physics* 5.6 (2009), pp. 438–442. DOI: 10.1038/nphys1270 (cit. on p. 41).

[133] Y. Xia, D. Qian, D. Hsieh, L. Wray, A. Pal, H. Lin, A. Bansil, D. Grauer, Y. S. Hor, R. J. Cava, and M. Z. Hasan. "Observation of a large-gap topological-insulator class with a single Dirac cone on the surface". In: *Nature Physics* 5.6 (2009), pp. 398–402. DOI: 10.1038/nphys1274 (cit. on pp. 41, 45).

[134] T. Hanaguri, K. Igarashi, M. Kawamura, H. Takagi, and T. Sasagawa. "Momentum-resolved Landau-level spectroscopy of Dirac surface state inBi_2Se_3". In: *Physical Review B* 82.8 (2010), p. 081305. DOI: 10.1103/physrevb.82.081305 (cit. on p. 41).

[135] P. Cheng, C. Song, T. Zhang, Y. Zhang, Y. Wang, J.-F. Jia, J. Wang, Y. Wang, B.-F. Zhu, X. Chen, X. Ma, K. He, L. Wang, X. Dai, Z. Fang, X. Xie, X.-L. Qi, C.-X. Liu, S.-C. Zhang, and Q.-K. Xue. "Landau Quantization of Topological Surface States in Bi_2Se_3". In: *Physical Review Letters* 105.7 (2010), p. 076801. DOI: 10.1103/physrevlett.105.076801 (cit. on p. 41).

[136] C. Zhang, Y. Li, D. Pei, Z. Liu, and Y. Chen. "Angle-Resolved Photoemission Spectroscopy Study of Topological Quantum Materials". In: *Annual Review of Materials Research* 50.1 (2020), pp. 131–153. DOI: 10.1146/annurev-matsci-070218-121852 (cit. on p. 41).

[137] B. Lv, T. Qian, and H. Ding. "Angle-resolved photoemission spectroscopy and its application to topological materials". In: *Nature Reviews Physics* 1.10 (2019), pp. 609–626. DOI: 10.1038/s42254-019-0088-5 (cit. on p. 41).

[138] C. Chen, S. He, H. Weng, W. Zhang, L. Zhao, H. Liu, X. Jia, D. Mou, S. Liu, J. He, Y. Peng, Y. Feng, Z. Xie, G. Liu, X. Dong, J. Zhang, X. Wang, Q. Peng, Z. Wang, S. Zhang, F. Yang, C. Chen, Z. Xu, X. Dai, Z. Fang, and X. J. Zhou. "Robustness of topological order and formation of quantum well states in topological insulators exposed to ambient environment". In: *Proceedings of the National Academy of Sciences* 109.10 (2012), pp. 3694–3698. DOI: 10.1073/pnas.1115555109 (cit. on pp. 42–43).

[139] M. Bianchi, D. Guan, S. Bao, J. Mi, B. B. Iversen, P. D. King, and P. Hofmann. "Coexistence of the topological state and a two-dimensional electron gas on the surface of Bi_2Se_3". In: *Nature Communications* 1.1 (2010). DOI: 10.1038/ncomms1131 (cit. on pp. 42–43).

[140] K. Momma and F. Izumi. "*VESTA*: a three-dimensional visualization system for electronic and structural analysis". In: *Journal of Applied Crystallography* 41.3 (2008), pp. 653–658. DOI: 10.1107/s0021889808012016 (cit. on p. 42).

[141] A. A. Taskin and Y. Ando. "Berry phase of nonideal Dirac fermions in topological insulators". In: *Physical Review B* 84.3 (2011), p. 035301. DOI: 10.1103/physrevb.84.035301 (cit. on p. 42).

[142] M. Nomura, S. Souma, A. Takayama, T. Sato, T. Takahashi, K. Eto, K. Segawa, and Y. Ando. "Relationship between Fermi surface warping and out-of-plane spin polarization in topological insulators: A view from spin- and angle-resolved photoemission". In: *Physical Review B* 89.4 (2014), p. 045134. DOI: 10.1103/physrevb.89.045134 (cit. on pp. 43–44, 94, 96).

[143] J. Sánchez-Barriga, M. R. Scholz, E. Golias, E. Rienks, D. Marchenko, A. Varykhalov, L. V. Yashina, and O. Rader. "Anisotropic effect of warping on the lifetime broadening of topological surface states in angle-resolved photoemission from Bi_2Te_3". In: *Physical Review B* 90.19 (2014), p. 195413. DOI: 10.1103/physrevb.90.195413 (cit. on pp. 43–44, 57).

[144] T. Zhang, P. Cheng, X. Chen, J.-F. Jia, X. Ma, K. He, L. Wang, H. Zhang, X. Dai, Z. Fang, X. Xie, and Q.-K. Xue. "Experimental Demonstration of Topological Surface States Protected by Time-Reversal Symmetry". In: *Physical Review Letters* 103.26 (2009), p. 266803. DOI: 10.1103/physrevlett.103.266803 (cit. on p. 43).

[145] L. Fu. "Hexagonal Warping Effects in the Surface States of the Topological Insulator Bi_2Te_3". In: *Physical Review Letters* 103.26 (2009), p. 266801. DOI: 10.1103/physrevlett.103.266801 (cit. on pp. 43–44).

[146] S. Basak, H. Lin, L. A. Wray, S.-Y. Xu, L. Fu, M. Z. Hasan, and A. Bansil. "Spin texture on the warped Dirac-cone surface states in topological insulators". In: *Physical Review B* 84.12 (2011), p. 121401. DOI: 10.1103/physrevb.84.121401 (cit. on pp. 43–44).

[147] O. V. Yazyev, J. E. Moore, and S. G. Louie. "Spin Polarization and Transport of Surface States in the Topological Insulators Bi_2Se_3 and Bi_2Te_3 from First Principles". In: *Physical Review Letters* 105.26 (2010), p. 266806. DOI: 10.1103/physrevlett.105.266806 (cit. on p. 43).

[148] C. Jozwiak, J. A. Sobota, K. Gotlieb, A. F. Kemper, C. R. Rotundu, R. J. Birgeneau, Z. Hussain, D.-H. Lee, Z.-X. Shen, and A. Lanzara. "Spin-polarized surface resonances accompanying topological surface state formation". In: *Nature Communications* 7.1 (2016). DOI: 10.1038/ncomms13143 (cit. on pp. 43, 45, 52, 57).

[149] C. Seibel, H. Bentmann, J. Braun, J. Minár, H. Maaß, K. Sakamoto, M. Arita, K. Shimada, H. Ebert, and F. Reinert. "Connection of a Topological Surface State with the Bulk Continuum in Sb_2Te_3 (0001)". In: *Physical Review Letters* 114.6 (2015), p. 066802. DOI: 10.1103/physrevlett.114.066802 (cit. on pp. 43, 45).

[150] C. Cacho, A. Crepaldi, M. Battiato, J. Braun, F. Cilento, M. Zacchigna, M. Richter, O. Heckmann, E. Springate, Y. Liu, S. Dhesi, H. Berger, P. Bugnon, K. Held, M. Grioni, H. Ebert, K. Hricovini, J. Minár, and F. Parmigiani. "Momentum-Resolved Spin Dynamics of Bulk and Surface Excited States in the Topological Insulator Bi_2Se_3". In: *Physical Review Letters* 114.9 (2015), p. 097401. DOI: 10.1103/physrevlett.114.097401 (cit. on p. 43).

[151] J. Braun, J. Minár, and H. Ebert. "Correlation, temperature and disorder: Recent developments in the one-step description of angle-resolved photoemission". In: *Physics Reports* 740 (2018), pp. 1–34. DOI: 10.1016/j.physrep.2018.02.007 (cit. on pp. 43, 45–46).

[152] H. Krakauer, M. Posternak, and A. J. Freeman. "Origin of Surface Resonance States in Nearly-Free-Electron Metals: Al(001)". In: *Physical Review Letters* 41.15 (1978), pp. 1072–1075. DOI: 10.1103/physrevlett.41.1072 (cit. on p. 43).

[153] C.-X. Liu, X.-L. Qi, H. Zhang, X. Dai, Z. Fang, and S.-C. Zhang. "Model Hamiltonian for topological insulators". In: *Physical Review B* 82.4 (2010), p. 045122. DOI: 10.1103/physrevb.82.045122 (cit. on p. 44).

[154] K. Kuroda, M. Arita, K. Miyamoto, M. Ye, J. Jiang, A. Kimura, E. E. Krasovskii, E. V. Chulkov, H. Iwasawa, T. Okuda, K. Shimada, Y. Ueda, H. Namatame, and M. Taniguchi. "Hexagonally Deformed Fermi Surface of the 3D Topological Insulator Bi_2Se_3". In: *Physical Review Letters* 105.7 (2010), p. 076802. DOI: 10.1103/physrevlett.105.076802 (cit. on pp. 44, 47).

[155] M. Nurmamat, E. E. Krasovskii, Y. Ishida, K. Sumida, J. Chen, T. Yoshikawa, E. V. Chulkov, K. A. Kokh, O. E. Tereshchenko, S. Shin, and A. Kimura. "Ultrafast dynamics of an unoccupied surface resonance state in $BiTe_2Se_3$". In: *Physical Review B* 97.11 (2018), p. 115303. DOI: 10.1103/physrevb.97.115303 (cit. on pp. 44, 49, 52).

[156] C. Datzer, A. Zumbülte, J. Braun, T. Förster, A. B. Schmidt, J. Mi, B. Iversen, P. Hofmann, J. Minár, H. Ebert, P. Krüger, M. Rohlfing, and M. Donath. "Unraveling the spin structure of unoccupied states in Bi_2Se_3". In: *Physical Review B* 95.11 (2017), p. 115401. DOI: 10.1103/physrevb.95.115401 (cit. on pp. 44, 46, 49, 57).

[157] I. Aguilera, C. Friedrich, and S. Blügel. "Many-body corrected tight-binding Hamiltonians for an accurate quasiparticle description of topological insulators of the Bi_2Se_3 family". In: *Physical Review B* 100.15 (2019), p. 155147. DOI: 10.1103/physrevb.100.155147 (cit. on pp. 44, 51, 57).

[158] M. Jurczyszyn, M. Sikora, M. Chrobak, and L. Jurczyszyn. "Studies of surface states in Bi_2Se_3 induced by the Bi_{Se} substitution in the crystal subsurface structure". In: *Applied Surface Science* 528 (2020), p. 146978. DOI: 10.1016/j.apsusc.2020.146978 (cit. on p. 45).

[159] A. Nuber, J. Braun, F. Forster, J. Minár, F. Reinert, and H. Ebert. "Surface versus bulk contributions to the Rashba splitting in surface systems". In: *Physical Review B* 83.16 (2011), p. 165401. DOI: 10.1103/physrevb.83.165401 (cit. on pp. 45–46, 49, 51).

[160] A. Bendounan, K. Aït-Mansour, J. Braun, J. Minár, S. Bornemann, R. Fasel, O. Gröning, F. Sirotti, and H. Ebert. "Evolution of the Rashba spin-orbit-split Shockley state on Ag/Pt(111)". In: *Physical Review B* 83.19 (2011), p. 195427. DOI: 10.1103/physrevb.83.195427 (cit. on p. 45).

[161] C. Seibel, H. Maaß, H. Bentmann, J. Braun, K. Sakamoto, M. Arita, K. Shimada, J. Minár, H. Ebert, and F. Reinert. "The Rashba-split surface state of Sb_2Te_3 (0001) and its interaction with bulk states". In: *Journal of Electron Spectroscopy and Related Phenomena* 201 (2015), pp. 110–114. DOI: 10.1016/j.elspec.2014.12.003 (cit. on p. 45).

[162] J. P. Perdew, K. Burke, and M. Ernzerhof. "Generalized Gradient Approximation Made Simple". In: *Physical Review Letters* 77.18 (1996), pp. 3865–3868. DOI: 10.1103/physrevlett.77.3865 (cit. on p. 46).

[163] J. Braun, K. Miyamoto, A. Kimura, T. Okuda, M. Donath, H. Ebert, and J. Minár. "Exceptional behavior of d-like surface resonances on W(110): the one-step model in its density matrix formulation". In: *New Journal of Physics* 16.1 (2014), p. 015005. DOI: 10.1088/1367-2630/16/1/015005 (cit. on p. 46).

[164] H. Ebert. *et al.*, *The Munich SPR-KKR package, version 8.6*. Accessed: May 2023. URL: https://www.ebert.cup.uni-muenchen.de/en/software-en/13-sprkkr (cit. on p. 46).

[165] D. Hsieh, Y. Xia, D. Qian, L. Wray, J. H. Dil, F. Meier, J. Osterwalder, L. Patthey, J. G. Checkelsky, N. P. Ong, A. V. Fedorov, H. Lin, A. Bansil, D. Grauer, Y. S. Hor, R. J. Cava, and M. Z. Hasan. "A tunable topological insulator in the spin helical Dirac transport regime". In: *Nature* 460.7259 (2009), pp. 1101–1105. DOI: 10.1038/nature08234 (cit. on p. 52).

[166] J. A. Sobota, S.-L. Yang, A. F. Kemper, J. J. Lee, F. T. Schmitt, W. Li, R. G. Moore, J. G. Analytis, I. R. Fisher, P. S. Kirchmann, T. P. Devereaux, and Z.-X. Shen. "Direct Optical Coupling to an Unoccupied Dirac Surface State in the Topological Insulator Bi_2Se_3". In: *Physical Review Letters* 111.13 (2013), p. 136802. DOI: 10.1103/physrevlett.111.136802 (cit. on p. 52).

[167] A. Crepaldi, F. Cilento, B. Ressel, C. Cacho, J. C. Johannsen, M. Zacchigna, H. Berger, P. Bugnon, C. Grazioli, I. C. E. Turcu, E. Springate, K. Kern, M. Grioni, and F. Parmigiani. "Evidence of reduced surface electron-phonon scattering in the conduction band of Bi_2Se_3 by nonequilibrium ARPES". In: *Physical Review B* 88.12 (2013), p. 121404. DOI: 10.1103/physrevb.88.121404 (cit. on p. 52).

[168] M. Kang, L. Ye, S. Fang, J.-S. You, A. Levitan, M. Han, J. I. Facio, C. Jozwiak, A. Bostwick, E. Rotenberg, M. K. Chan, R. D. McDonald, D. Graf, K. Kaznatcheev, E. Vescovo, D. C. Bell, E. Kaxiras, J. van den Brink, M. Richter, M. P. Ghimire, J. G. Checkelsky, and R. Comin. "Dirac fermions and flat bands in the ideal kagome metal FeSn". In: *Nature Materials* 19.2 (2019), pp. 163–169. DOI: 10.1038/s41563-019-0531-0 (cit. on pp. 59, 61, 63).

[169] J.-X. Yin, S. S. Zhang, G. Chang, Q. Wang, S. S. Tsirkin, Z. Guguchia, B. Lian, H. Zhou, K. Jiang, I. Belopolski, N. Shumiya, D. Multer, M. Litskevich, T. A. Cochran, H. Lin, Z. Wang, T. Neupert, S. Jia, H. Lei, and M. Z. Hasan. "Negative flat band magnetism in a spin–orbit-coupled correlated kagome magnet". In: *Nature Physics* 15.5 (2019), pp. 443–448. DOI: 10.1038/s41567-019-0426-7 (cit. on pp. 59–60).

[170] Y. Hu, X. Wu, B. R. Ortiz, S. Ju, X. Han, J. Ma, N. C. Plumb, M. Radovic, R. Thomale, S. D. Wilson, A. P. Schnyder, and M. Shi. "Rich nature of Van Hove singularities in Kagome superconductor CsV_3Sb_5". In: *Nature Communications* 13.2220 (2022), p. 2220. DOI: 10.1038/s41467-022-29828-x (cit. on p. 59).

[171] I. I. Mazin, H. O. Jeschke, F. Lechermann, H. Lee, M. Fink, R. Thomale, and R. Valentí. "Theoretical prediction of a strongly correlated Dirac metal". In: *Nature Communications* 5 (2014), p. 4261. DOI: 10.1038/ncomms5261 (cit. on pp. 59–61).

[172] H.-D. Liu, Y.-H. Chen, H.-F. Lin, H.-S. Tao, and J.-H. Wu. "Interaction and spin-orbit effects on a kagome lattice at 1/3 filling". In: *Chinese Physics B* 23.7 (2014), p. 077101. DOI: 10.1088/1674-1056/23/7/077101 (cit. on p. 59).

[173] V. I. Iglovikov, F. Hébert, B. Grémaud, G. G. Batrouni, and R. T. Scalettar. "Superconducting transitions in flat-band systems". In: *Physical Review B* 90.9 (2014), p. 094506. DOI: 10.1103/physrevb.90.094506 (cit. on p. 59).

[174] W.-H. Ko, P. A. Lee, and X.-G. Wen. "Doped kagome system as exotic superconductor". In: *Physical Review B* 79.21 (2009), p. 214502. DOI: 10.1103/physrevb.79.214502 (cit. on p. 59).

[175] K. Jiang, T. Wu, J.-X. Yin, Z. Wang, M. Z. Hasan, S. D. Wilson, X. Chen, and J. Hu. "Kagome superconductors AV3Sb5 (A=K, Rb, Cs)". In: *National Science Review* (Sept. 2022), pp. 2095–5138. DOI: 10.1093/nsr/nwac199 (cit. on p. 59).

[176] T. Neupert, M. M. Denner, J.-X. Yin, R. Thomale, and M. Z. Hasan. "Charge order and superconductivity in kagome materials". In: *Nature Physics* 18.2 (2021), pp. 137–143. DOI: 10.1038/s41567-021-01404-y (cit. on p. 59).

[177] H. Tan, Y. Liu, Z. Wang, and B. Yan. "Charge Density Waves and Electronic Properties of Superconducting Kagome Metals". In: *Physical Review Letters* 127.4 (2021), p. 046401. DOI: 10.1103/physrevlett.127.046401 (cit. on p. 59).

[178] S. Han, C. S. Tang, L. Li, Y. Liu, H. Liu, J. Gou, J. Wu, D. Zhou, P. Yang, C. Diao, J. Ji, J. Bao, L. Zhang, M. Zhao, M. V. Milošević, Y. Guo, L. Tian, M. B. H. Breese, G. Cao, C. Cai, A. T. S. Wee, and X. Yin. "Orbital-Hybridization-Driven Charge Density Wave Transition in CsV_3Sb_5". In: *Advanced Materials* (2022), p. 2209010. DOI: 10.1002/adma.202209010 (cit. on p. 59).

[179] S. D. Huber and E. Altman. "Bose condensation in flat bands". In: *Physical Review B* 82.18 (2010), p. 184502. DOI: 10.1103/physrevb.82.184502 (cit. on p. 59).

[180] T. Neupert, L. Santos, C. Chamon, and C. Mudry. "Fractional quantum Hall sates at zero magnetic field". In: *Physical Review Letters* 106.23 (2011), p. 236804. DOI: 10.1103/physrevlett.106.236804 (cit. on p. 59).

[181] S.-Y. Xu, M. Neupane, I. Belopolski, C. Liu, N. Alidoust, G. Bian, S. Jia, G. Landolt, B. Slomski, J. H. Dil, P. P. Shibayev, S. Basak, T.-R. Chang, H.-T. Jeng, R. J. Cava, H. Lin, A. Bansil, and M. Z. Hasan. "Unconventional transformation of spin Dirac phase across a topological quantum phase transition". In: *Nature Communications* 6.1 (2015). DOI: 10.1038/ncomms7870 (cit. on p. 59).

[182] S. Nakatsuji, N. Kiyohara, and T. Higo. "Large anomalous Hall effect in a non-collinear antiferromagnet at room temperature". In: *Nature* 527.7577 (2015), pp. 212–215. DOI: 10.1038/nature15723 (cit. on p. 59).

[183] Z. Lin, J.-H. Choi, Q. Zhang, W. Qin, S. Yi, P. Wang, L. Li, Y. Wang, H. Zhang, Z. Sun, L. Wei, S. Zhang, T. Guo, Q. Lu, J.-H. Cho, C. Zeng, and Z. Zhang. "Flatbands and Emergent Ferromagnetic Ordering in Fe_3Sn_2 Kagome Lattices". In: *Physical Review Letters* 121.9 (2018), p. 096401. DOI: 10.1103/physrevlett.121.096401 (cit. on pp. 59–60).

[184] K. Kuroda, T. Tomita, M.-T. Suzuki, C. Bareille, A. A. Nugroho, P. Goswami, M. Ochi, M. Ikhlas, M. Nakayama, S. Akebi, R. Noguchi, R. Ishii, N. Inami, K. Ono, H. Kumigashira, A. Varykhalov, T. Muro, T. Koretsune, R. Arita, S. Shin, T. Kondo, and S. Nakatsuji. "Evidence for magnetic Weyl fermions in a correlated metal". In: *Nature materials* 16.11 (2017), pp. 1090–1095. DOI: 10.1038/nmat4987 (cit. on pp. 59–60).

[185] A. Mielke. "Exact ground states for the Hubbard model on the Kagome lattice". In: *Journal of Physics A: Mathematical and General* 25.16 (1992), pp. 4335–4345. DOI: 10.1088/0305-4470/25/16/011 (cit. on p. 59).

[186] D. Leykam, A. Andreanov, and S. Flach. "Artificial flat band systems: from lattice models to experiments". In: *Advances in Physics: X* 3.1 (2018), p. 1473052. DOI: 10.1080/23746149.2018.1473052 (cit. on p. 59).

[187] B. C. Sales, W. R. Meier, A. F. May, J. Xing, J.-Q. Yan, S. Gao, Y. H. Liu, M. B. Stone, A. D. Christianson, Q. Zhang, and M. A. McGuire. "Tuning the flat bands of the kagome metal CoSn with Fe, In, or Ni doping". In: *Physical Review Materials* 5.4 (2021), p. 044202. DOI: 10.1103/physrevmaterials.5.044202 (cit. on p. 59).

[188] Y. Xie, L. Chen, T. Chen, Q. Wang, Q. Yin, J. R. Stewart, M. B. Stone, L. L. Daemen, E. Feng, H. Cao, H. Lei, Z. Yin, A. H. MacDonald, and P. Dai. "Spin excitations in metallic kagome lattice FeSn and CoSn". In: *Communications Physics* 4.1 (2021). DOI: 10.1038/s42005-021-00736-8 (cit. on pp. 59–61).

[189] B. Sutherland. "Localization of electronic wave functions due to local topology". In: *Physical Review B* 34.8 (1986), pp. 5208–5211. DOI: 10.1103/physrevb.34.5208 (cit. on p. 59).

[190] H.-M. Guo and M. Franz. "Topological insulator on the kagome lattice". In: *Physical Review B* 80.11 (2009), p. 113102. DOI: 10.1103/physrevb.80.113102 (cit. on p. 60).

[191] A. Bolens and N. Nagaosa. "Topological states on the breathing kagome lattice". In: *Physical Review B* 99.16 (2019), p. 165141. DOI: 10.1103/physrevb.99.165141 (cit. on p. 60).

[192] W. R. Meier, M.-H. Du, S. Okamoto, N. Mohanta, A. F. May, M. A. McGuire, C. A. Bridges, G. D. Samolyuk, and B. C. Sales. "Flat bands in the CoSn-type compounds". In: *Physical Review B* 102.7 (Aug. 31, 2020), p. 075148. DOI: 10.1103/physrevb.102.075148 (cit. on p. 60).

[193] L. Ye, M. Kang, J. Liu, F. von Cube, C. R. Wicker, T. Suzuki, C. Jozwiak, A. Bostwick, E. Rotenberg, D. C. Bell, L. Fu, R. Comin, and J. G. Checkelsky. "Massive Dirac fermions in a ferromagnetic kagome metal". In: *Nature* 555.7698 (2018), pp. 638–642. DOI: 10.1038/nature25987 (cit. on p. 60).

[194] J. Allred, S. Jia, M. Bremholm, B. Chan, and R. Cava. "Ordered CoSn-type ternary phases in Co3Sn3-xGex". In: *Journal of Alloys and Compounds* 539 (2012), pp. 137–143. DOI: 10.1016/j.jallcom.2012.04.045 (cit. on p. 61).

[195] S. Wan, H. Lu, and L. Huang. "Temperature dependence of correlated electronic states in the archetypal kagome metal CoSn". In: *Physical Review B* 105.15 (2022), p. 155131. DOI: 10.1103/physrevb.105.155131 (cit. on p. 61).

[196] Z. X. Wang, Q. Wu, Q. W. Yin, C. S. Gong, Z. J. Tu, T. Lin, Q. M. Liu, L. Y. Shi, S. J. Zhang, D. Wu, H. C. Lei, T. Dong, and N. L. Wang. "Unconventional charge density wave and photoinduced lattice symmetry change in the kagome metal CsV_3Sb_5 probed by time-resolved spectroscopy". In: *Physical Review B* 104.16 (2021), p. 165110. DOI: 10.1103/physrevb.104.165110 (cit. on p. 61).

[197] D. Azoury, A. von Hoegen, Y. Su, K. H. Oh, T. Holder, H. Tan, B. R. Ortiz, A. C. Salinas, S. D. Wilson, B. Yan, and N. Gedik. *Direct Observation of Collective Modes of the Charge Density Wave in the Kagome Metal CsV_3Sb_5*. 2023. arXiv: 2301.10299 [cond-mat.str-el] (cit. on pp. 61, 96).

[198] J. G. Bednorz and K. A. Müller. "Possible high T_C superconductivity in the Ba-La-Cu-O system". In: *Zeitschrift für Physik B Condensed Matter* 64.2 (1986), pp. 189–193. DOI: 10.1007/bf01303701 (cit. on p. 69).

[199] D. Rybicki, M. Jurkutat, S. Reichardt, C. Kapusta, and J. Haase. "Perspective on the phase diagram of cuprate high-temperature superconductors". In: *Nature Communications* 7.1 (2016). DOI: 10.1038/ncomms11413 (cit. on p. 69).

[200] Y. Noat, A. Mauger, M. Nohara, H. Eisaki, S. Ishida, and W. Sacks. "Cuprates phase diagram deduced from magnetic susceptibility: What is the "true" pseudogap line?" In: *Solid State Communications* 348-349 (2022), p. 114689. DOI: 10.1016/j.ssc.2022.114689 (cit. on p. 69).

[201] J. Osterwalder, P. Aebi, P. Schwaller, L. Schlapbach, M. Shimoda, T. Mochiku, and K. Kadowaki. "Angle-resolved photoemission experiments on $Bi_2Sr_2CaCu_2O_{8+\delta}(001)$". In: *Applied Physics A Materials Science Processing* 60.3 (1995), pp. 247–254. DOI: 10.1007/bf01538399 (cit. on pp. 70, 72).

[202] W. S. Lee, I. M. Vishik, K. Tanaka, D. H. Lu, T. Sasagawa, N. Nagaosa, T. P. Devereaux, Z. Hussain, and Z.-X. Shen. "Abrupt onset of a second energy gap at the superconducting transition of underdoped Bi2212". In: *Nature* 450.7166 (2007), pp. 81–84. DOI: 10.1038/nature06219 (cit. on pp. 70–71).

[203] J. M. Tarascon, W. R. McKinnon, P. Barboux, D. M. Hwang, B. G. Bagley, L. H. Greene, G. W. Hull, Y. LePage, N. Stoffel, and M. Giroud. "Preparation, structure, and properties of the superconducting compound series $Bi_2Sr_2Ca_{n-1}Cu_nO_y$ with $n = 1, 2$ and 3". In: *Physical Review B* 38.13 (1988), pp. 8885–8892. DOI: 10.1103/physrevb.38.8885 (cit. on p. 70).

[204] M. D. Kirk, C. B. Eom, B. Oh, S. R. Spielman, M. R. Beasley, A. Kapitulnik, T. H. Geballe, and C. F. Quate. "Scanning tunneling microscopy of the $Bi_2(Ca, Sr)_3Cu_2O_{8+\delta}$ single crystal and thin film". In: *Applied Physics Letters* 52.24 (1988), pp. 2071–2073. DOI: 10.1063/1.99750 (cit. on p. 70).

[205] P. A. P. Lindberg, I. Lindau, and W. E. Spicer. "Quantitative analysis of x-ray photoemission spectra applied to $Bi_2Sr_2CaCu_2O_8$ high-temperature superconductors". In: *Physical Review B* 40.10 (1989), pp. 6822–6827. DOI: 10.1103/physrevb.40.6822 (cit. on p. 70).

[206] W. E. Pickett. "Electronic structure of the high-temperature oxide superconductors". In: *Reviews of Modern Physics* 61.2 (1989), pp. 433–512. DOI: 10.1103/revmodphys.61.433 (cit. on p. 70).

[207] D. N. Basov and T. Timusk. "Electrodynamics of high-T_c superconductors". In: *Reviews of Modern Physics* 77.2 (2005), pp. 721–779. DOI: 10.1103/revmodphys.77.721 (cit. on pp. 70, 77).

[208] P. A. Lee, N. Nagaosa, and X.-G. Wen. "Doping a Mott insulator: Physics of high-temperature superconductivity". In: *Reviews of Modern Physics* 78.1 (2006), pp. 17–85. DOI: 10.1103/revmodphys.78.17 (cit. on pp. 70, 77).

[209] J. Bardeen, L. N. Cooper, and J. R. Schrieffer. "Theory of Superconductivity". In: *Physical Review* 108.5 (1957), pp. 1175–1204. DOI: 10.1103/physrev.108.1175 (cit. on p. 70).

[210] C. M. Varma. "Non-Fermi-liquid states and pairing instability of a general model of copper oxide metals". In: *Physical Review B* 55.21 (1997), pp. 14554–14580. DOI: 10.1103/physrevb.55.14554 (cit. on p. 71).

[211] D. Fournier, G. Levy, Y. Pennec, J. L. McChesney, A. Bostwick, E. Rotenberg, R. Liang, W. N. Hardy, D. A. Bonn, I. S. Elfimov, and A. Damascelli. "oss of nodal quasiparticle integrity in underdoped $YBa_2Cu_3O_{6+x}$". In: *Nature Physics* 6.11 (2010), pp. 905–911. DOI: 10.1038/nphys1763 (cit. on p. 71).

[212] S. I. Vedeneev. "Pseudogap problem in high-temperature superconductors". In: *Physics-Uspekhi* 64.9 (2021), pp. 890–922. DOI: 10.3367/ufne.2020.12.038896 (cit. on p. 71).

[213] I. M. Vishik, W. S. Lee, R.-H. He, M Hashimoto, Z Hussain, T. P. Devereaux, and Z.-X. Shen. "ARPES studies of cuprate Fermiology: superconductivity, pseudogap and quasiparticle dynamics". In: *New Journal of Physics* 12.10 (2010), p. 105008. DOI: 10.1088/1367-2630/12/10/105008 (cit. on p. 71).

[214] M. Civelli, M. Capone, A. Georges, K. Haule, O. Parcollet, T. D. Stanescu, and G. Kotliar. "Nodal-Antinodal Dichotomy and the Two Gaps of a Superconducting Doped Mott Insulator". In: *Physical Review Letters* 100.4 (2008), p. 046402. DOI: 10.1103/physrevlett.100.046402 (cit. on p. 71).

[215] M. Ferrero, P. S. Cornaglia, L. D. Leo, O. Parcollet, G. Kotliar, and A. Georges. "Pseudogap opening and formation of Fermi arcs as an orbital-selective Mott transition in momentum space". In: *Physical Review B* 80.6 (2009), p. 064501. DOI: 10.1103/physrevb.80.064501 (cit. on p. 71).

[216] N. F. Mott. "The Basis of the Electron Theory of Metals, with Special Reference to the Transition Metals". In: *Proceedings of the Physical Society. Section A* 62.7 (1949), pp. 416–422. DOI: 10.1088/0370-1298/62/7/303 (cit. on p. 71).

[217] E. Gull, M. Ferrero, O. Parcollet, A. Georges, and A. J. Millis. "Momentum-space anisotropy and pseudogaps: A comparative cluster dynamical mean-field analysis of the doping-driven metal-insulator transition in the two-dimensional Hubbard model". In: *Physical Review B* 82.15 (2010), p. 155101. DOI: 10.1103/physrevb.82.155101 (cit. on p. 71).

[218] R. Cortés, L. Rettig, Y. Yoshida, H. Eisaki, M. Wolf, and U. Bovensiepen. "Momentum-Resolved Ultrafast Electron Dynamics in Superconducting $Bi_2Sr_2CaCu_2O_{8+\delta}$". In: *Physical Review Letters* 107.9 (2011), p. 097002. DOI: 10.1103/physrevlett.107.097002 (cit. on p. 72).

[219] S. Parham, H. Li, T. Nummy, J. Waugh, X. Zhou, J. Griffith, J. Schneeloch, R. Zhong, G. Gu, and D. Dessau. "Ultrafast Gap Dynamics and Electronic Interactions in a Photoexcited Cuprate Superconductor". In: *Physical Review X* 7.4 (2017), p. 041013. DOI: 10.1103/physrevx.7.041013 (cit. on p. 72).

[220] G. L. Dakovski, T. Durakiewicz, J.-X. Zhu, P. S. Riseborough, G. Gu, S. M. Gilbertson, A. Taylor, and G. Rodriguez. "Quasiparticle dynamics across the full Brillouin zone of $Bi_2Sr_2CaCu_2O_{8+\delta}$ traced with ultrafast time and angle-resolved photoemission spectroscopy". In: *Structural Dynamics* 2.5 (2015), p. 054501. DOI: 10.1063/1.4933133 (cit. on p. 72).

[221] J. A. Rosen, R. Comin, G. Levy, D. Fournier, Z.-H. Zhu, B. Ludbrook, C. N. Veenstra, A. Nicolaou, D. Wong, P. Dosanjh, Y. Yoshida, H. Eisaki, G. R. Blake, F. White, T. T. M. Palstra, R. Sutarto, F. He, A. F. Pereira, Y. Lu, B. Keimer, G. Sawatzky, L. Petaccia, and A. Damascelli. "Surface-enhanced charge-density-wave instability in underdoped $Bi_2Sr_{2-x}La_xCuO_{6+\delta}$". In: *Nature Communications* 4.1 (2013). DOI: 10.1038/ncomms2977 (cit. on p. 72).

[222] D. L. Feng, N. P. Armitage, D. H. Lu, A. Damascelli, J. P. Hu, P. Bogdanov, A. Lanzara, F. Ronning, K. M. Shen, H. Eisaki, C. Kim, Z.-X. Shen, J. i. Shimoyama, and K. Kishio. "Bilayer Splitting in the Electronic Structure of Heavily Overdoped $Bi_2Sr_2CaCu_2O_{8+\delta}$". In: *Physical Review Letters* 86.24 (2001), pp. 5550–5553. DOI: 10.1103/physrevlett.86.5550 (cit. on p. 72).

[223] S. Peli, S. D. Conte, R. Comin, N. Nembrini, A. Ronchi, P. Abrami, F. Banfi, G. Ferrini, D. Brida, S. Lupi, M. Fabrizio, A. Damascelli, M. Capone, G. Cerullo, and C. Giannetti. "Mottness at finite doping and charge instabilities in cuprates". In: *Nature Physics* 13.8 (2017), pp. 806–811. DOI: 10.1038/nphys4112 (cit. on p. 77).

[224] J. Ghijsen, L. H. Tjeng, H. Eskes, G. A. Sawatzky, and R. L. Johnson. "Resonant photoemission study of the electronic structure of CuO and Cu_2O". In: *Physical Review B* 42.4 (1990), pp. 2268–2274. DOI: 10.1103/physrevb.42.2268 (cit. on pp. 77, 82).

[225] M. Qvarford, S. Söderholm, G. Chiaia, R. Nyholm, J. N. Andersen, I. Lindau, U. O. Karlsson, L. Leonyuk, A. Nilsson, and N. Mårtensson. "Doping dependence of the O 1*s* core-level photoemission in Bi-Sr-Ca-Cu-O superconductors". In: *Physical Review B* 53.22 (1996), R14753–R14756. DOI: 10.1103/physrevb.53.r14753 (cit. on pp. 77, 84).

[226] J. Zaanen, G. A. Sawatzky, and J. W. Allen. "Band gaps and electronic structure of transition-metal compounds". In: *Physical Review Letters* 55.4 (1985), pp. 418–421. DOI: 10.1103/physrevlett.55.418 (cit. on p. 77).

[227] F. Cilento, G. Manzoni, A. Sterzi, S. Peli, A. Ronchi, A. Crepaldi, F. Boschini, C. Cacho, R. Chapman, E. Springate, H. Eisaki, M. Greven, M. Berciu, A. F. Kemper, A. Damascelli, M. Capone, C. Giannetti, and F. Parmigiani. "Dynamics of correlation-frozen antinodal quasiparticles in superconducting cuprates". In: *Science Advances* 4.2 (2018). DOI: 10.1126/sciadv.aar1998 (cit. on pp. 78–81, 95).

[228] H. Romberg, M. Alexander, N. Nücker, P. Adelmann, and J. Fink. "Electronic structure of the system $La_{2-x}Sr_xCuO_{4+\delta}$". In: *Physical Review B* 42.13 (1990), pp. 8768–8771. DOI: 10.1103/physrevb.42.8768 (cit. on p. 77).

[229] Y. Ohta, K. Tsutsui, W. Koshibae, T. Shimozato, and S. Maekawa. "Evolution of the in-gap state in high-T_c cuprates". In: *Physical Review B* 46.21 (1992), pp. 14022–14033. DOI: 10.1103/physrevb.46.14022 (cit. on p. 77).

[230] B. Keimer, S. A. Kivelson, M. R. Norman, S. Uchida, and J. Zaanen. "From quantum matter to high-temperature superconductivity in copper oxides". In: *Nature* 518.7538 (2015), pp. 179–186. DOI: 10.1038/nature14165 (cit. on p. 77).

[231] Y. Kohsaka, C. Taylor, K. Fujita, A. Schmidt, C. Lupien, T. Hanaguri, M. Azuma, M. Takano, H. Eisaki, H. Takagi, S. Uchida, and J. C. Davis. "An Intrinsic Bond-Centered Electronic Glass with Unidirectional Domains in Underdoped Cuprates". In: *Science* 315.5817 (2007), pp. 1380–1385. DOI: 10.1126/science.1138584 (cit. on p. 77).

[232] P. Kuiper, G. Kruizinga, J. Ghijsen, G. A. Sawatzky, and H. Verweij. "Character of Holes in $Li_xNi_{1-x}O$ and Their Magnetic Behavior". In: *Physical Review Letters* 62.2 (1989), pp. 221–224. DOI: 10.1103/physrevlett.62.221 (cit. on p. 77).

[233] H. Eskes, M. B. J. Meinders, and G. A. Sawatzky. "Anomalous transfer of spectral weight in doped strongly correlated systems". In: *Physical Review Letters* 67.8 (1991), pp. 1035–1038. DOI: 10.1103/physrevlett.67.1035 (cit. on p. 77).

[234] M. B. J. Meinders, H. Eskes, and G. A. Sawatzky. "Spectral-weight transfer: Breakdown of low-energy-scale sum rules in correlated systems". In: *Physical Review B* 48.6 (1993), pp. 3916–3926. DOI: 10.1103/physrevb.48.3916 (cit. on p. 77).

[235] S. L. Cooper, G. A. Thomas, J. Orenstein, D. H. Rapkine, A. J. Millis, S.-W. Cheong, A. S. Cooper, and Z. Fisk. "Growth of the optical conductivity in the Cu-O planes". In: *Physical Review B* 41.16 (1990), pp. 11605–11608. DOI: 10.1103/physrevb.41.11605 (cit. on p. 77).

[236] C. T. Chen, F. Sette, Y. Ma, M. S. Hybertsen, E. B. Stechel, W. M. C. Foulkes, M. Schulter, S.-W. Cheong, A. S. Cooper, L. W. Rupp, B. Batlogg, Y. L. Soo, Z. H. Ming, A. Krol, and Y. H. Kao. "Electronic states in $La_{2-x}Sr_xCuO_{8+\delta}$ probed by soft-x-ray absorption". In: *Physical Review Letters* 66.1 (1991), pp. 104–107. DOI: 10.1103/physrevlett.66.104 (cit. on p. 77).

[237] M. S. Hybertsen, E. B. Stechel, W. M. C. Foulkes, and M. Schlüter. "Model for low-energy electronic states probed by x-ray absorption in high-T_c cuprates". In: *Physical Review B* 45.17 (1992), pp. 10032–10050. DOI: 10.1103/physrevb.45.10032 (cit. on p. 77).

[238] C. Giannetti, F. Cilento, S. D. Conte, G. Coslovich, G. Ferrini, H. Molegraaf, M. Raichle, R. Liang, H. Eisaki, M. Greven, A. Damascelli, D. van der Marel, and F. Parmigiani. "Revealing the high-energy electronic excitations underlying the onset of high-temperature superconductivity in cuprates". In: *Nature Communications* 2.1 (2011). DOI: 10.1038/ncomms1354 (cit. on p. 77).

[239] D. R. Baykusheva, H. Jang, A. A. Husain, S. Lee, S. F. TenHuisen, P. Zhou, S. Park, H. Kim, J.-K. Kim, H.-D. Kim, M. Kim, S.-Y. Park, P. Abbamonte, B. Kim, G. Gu, Y. Wang, and M. Mitrano. "Ultrafast Renormalization of the On-Site Coulomb Repulsion in a Cuprate Superconductor". In: *Physical Review X* 12.1 (2022), p. 011013. DOI: 10.1103/physrevx.12.011013 (cit. on p. 77).

[240] C.-T. Kuo, S.-C. Lin, G. Conti, S.-T. Pi, L. Moreschini, A. Bostwick, J. Meyer-Ilse, E. Gullikson, J. B. Kortright, S. Nemšák, J. E. Rault, P. L. Fèvre, F. Bertran, A. F. Santander-Syro, I. A. Vartanyants, W. E. Pickett, R. Saint-Martin, A. Taleb-Ibrahimi, and C. S. Fadley. "Atomic-layer-resolved composition and electronic structure of the cuprate $Bi_2Sr_2CaCu_2O_{8+\delta}$ from soft x-ray standing-wave photoemission". In: *Physical Review B* 98.15 (2018), p. 155133. DOI: 10.1103/physrevb.98.155133 (cit. on p. 82).

[241] M. Presland, J. Tallon, R. Buckley, R. Liu, and N. Flower. "General trends in oxygen stoichiometry effects on T_C in Bi and Tl superconductors". In: *Physica C: Superconductivity* 176.1-3 (1991), pp. 95–105. DOI: 10.1016/0921-4534(91)90700-9 (cit. on p. 82).

[242] E. Pavarini, I. Dasgupta, T. Saha-Dasgupta, O. Jepsen, and O. K. Andersen. "Band-Structure Trend in Hole-Doped Cuprates and Correlation with $T_{c\max}$". In: *Physical Review Letters* 87.4 (2001), p. 047003. DOI: 10.1103/physrevlett.87.047003 (cit. on p. 82).

[243] W. Hu, S. Kaiser, D. Nicoletti, C. R. Hunt, I. Gierz, M. C. Hoffmann, M. L. Tacon, T. Loew, B. Keimer, and A. Cavalleri. "Optically enhanced coherent transport in $YBa_2Cu_3O_{6.5}$ by ultrafast redistribution of interlayer coupling". In: *Nature Materials* 13.7 (2014), pp. 705–711. DOI: 10.1038/nmat3963 (cit. on p. 82).

[244] R. Mankowsky, A. Subedi, M. Först, S. O. Mariager, M. Chollet, H. T. Lemke, J. S. Robinson, J. M. Glownia, M. P. Minitti, A. Frano, M. Fechner, N. A. Spaldin, T. Loew, B. Keimer, A. Georges, and A. Cavalleri. "Nonlinear lattice dynamics as a basis for enhanced superconductivity in YBa2Cu3O6.5". In: *Nature* 516.7529 (2014), pp. 71–73. DOI: 10.1038/nature13875 (cit. on p. 82).

[245] B. Liu, M. Först, M. Fechner, D. Nicoletti, J. Porras, T. Loew, B. Keimer, and A. Cavalleri. "Pump Frequency Resonances for Light-Induced Incipient Superconductivity in $YBa_2Cu_3O_{6.5}$". In: *Physical Review X* 10.1 (2020), p. 011053. DOI: 10.1103/physrevx.10.011053 (cit. on p. 82).

[246] D. M. Hill, H. M. Meyer, J. H. Weaver, C. F. Gallo, and K. C. Goretta. "Cu adatom interactions with single- and polycrystalline $Bi_2Ca_{1+x}Sr_{2-x}Cu_2O_{8+y}$". In: *Physical Review B* 38.16 (1988), pp. 11331–11336. DOI: 10.1103/physrevb.38.11331 (cit. on p. 82).

[247] C. Hinnen, C. N. van Huong, and P. Marcus. "A comparative X-ray photoemission study of $Bi_2Sr_2CaCu_2O_{8+\delta}$ and $Bi_{1.6}Pb_{0.4}Sr_2CaCu_2O_{8+\delta'}$". In: *Journal of Electron Spectroscopy and Related Phenomena* 73.3 (1995), pp. 293–304. DOI: 10.1016/0368-2048(94)02288-7 (cit. on p. 82).

[248] S. Kohiki, T. Wada, S. Kawashima, H. Takagi, S. Uchida, and S. Tanaka. "Structure and bonding of Bi-Sr-Ca-Cu-O crystal by x-ray photoelectron spectroscopy". In: *Physical Review B* 38.13 (1988), pp. 8868–8872. DOI: 10.1103/physrevb.38.8868 (cit. on p. 82).

[249] S. Söderholm, M. Qvarford, H. Bernhoff, J. N. Andersen, E. Lundgren, R.Nyholm, U. O. Karlsson, I. Lindau, and S. A. Flodström. "A photoelectron spectroscopy and x-ray absorption study of single crystal with adsorbed Cs: on the origin of the states affected by electron doping and evidence for spatially resolved electron doping". In: *Journal of Physics: Condensed Matter* 8.9 (1996), pp. 1307–1320. DOI: 10.1088/0953-8984/8/9/021 (cit. on p. 82).

[250] H. M. Meyer, D. M. Hill, T. J. Wagener, Y. Gao, J. H. Weaver, D. W. Capone, and K. C. Goretta. "Electronic structures of the $YBa_2Cu_3O_{7-x}$ surface and its modification by sputtering and adatoms of Ti and Cu". In: *Physical Review B* 38.10 (1988), pp. 6500–6512. DOI: 10.1103/physrevb.38.6500 (cit. on pp. 82, 84).

[251] F. Parmigiani, Z. X. Shen, D. B. Mitzi, I. Lindau, W. E. Spicer, and A. Kapitulnik. "O 1*s* core levels in $Bi_2Sr_2CaCu_2O_{8+\delta}$ single crystals". In: *Physical Review B* 43.4 (1991), pp. 3085–3090. DOI: 10.1103/physrevb.43.3085 (cit. on pp. 82–84).

[252] M. Nagoshi, Y. Fukuda, N. Sanada, Y. Syono, A. Tokiwa-Yamamoto, and M. Tachiki. "O1s core levels of Bi-Sr-Ca-Cu-O superconductors studied by X-ray photoelectron spectroscopy". In: *Journal of Electron Spectroscopy and Related Phenomena* 61.3-4 (1993), pp. 309–322. DOI: 10.1016/0368-2048(93)80022-e (cit. on p. 82).

[253] M. Nagoshi, Y. Syono, M. Tachiki, and Y. Fukuda. "Core-level binding energies of Ba, Sr, Ca, and Y for high-T_C superconductors and related oxides: A measure of hole concentration". In: *Physical Review B* 51.14 (1995), pp. 9352–9355. DOI: 10.1103/physrevb.51.9352 (cit. on p. 82).

[254] J. A. Leiro, M. H. Heinonen, and K. Elboussiri. "XPS study of the O 1*s* spectra of $(Bi, Pb)_2Sr_2CaCu_2O_x$ and $Bi_2Sr_2CaCu_2O_x$". In: *Physical Review B* 52.1 (1995), pp. 82–84. DOI: 10.1103/physrevb.52.82 (cit. on p. 82).

[255] M. Qvarford, J. F. van Acker, J. N. Andersen, R. Nyholm, I. Lindau, G. Chiaia, E. Lundgren, S. Söderholm, U. O. Karlsson, S. A. Flodström, and L. Leonyuk. "Resonant valence-band and Cu 3*p* photoemission at the Cu L_3 treshold of $Bi_2Sr_2CuO_6$ and $Bi_2Sr_2CaCu_2O_8$". In: *Physical Review B* 51.1 (1995), pp. 410–416. DOI: 10.1103/physrevb.51.410 (cit. on p. 82).

[256] P. Lele and A. S. Nigavekar. "Interface mechanism of Co/BiSrCaCuO system studied by XPS and UPS techniques". In: *Physica C: Superconductivity* 266.3-4 (1996), pp. 278–284. DOI: 10.1016/0921-4534(96)00344-9 (cit. on p. 82).

[257] M. Drescher, M. Hentschel, R. Kienberger, M. Uiberacker, V. Yakovlev, A. Scrinzi, T. Westerwalbesloh, U. Kleineberg, U. Heinzmann, and F. Krausz. "Time-resolved atomic inner-shell spectroscopy". In: *Nature* 419.6909 (2002), pp. 803–807. DOI: 10.1038/nature01143 (cit. on p. 84).

[258] P. Finetti, H. Höppner, E. Allaria, C. Callegari, F. Capotondi, P. Cinquegrana, M. Coreno, R. Cucini, M. B. Danailov, A. Demidovich, G. D. Ninno, M. D. Fraia, R. Feifel, E. Ferrari, L. Fröhlich, D. Gauthier, T. Golz, C. Grazioli, Y. Kai, G. Kurdi, N. Mahne, M. Manfredda, N. Medvedev, I. P. Nikolov, E. Pedersoli, G. Penco, O. Plekan, M. J. Prandolini, K. C. Prince, L. Raimondi, P. Rebernik, R. Riedel, E. Roussel, P. Sigalotti, R. Squibb, N. Stojanovic, S. Stranges, C. Svetina, T. Tanikawa, U. Teubner, V. Tkachenko, S. Toleikis, M. Zangrando, B. Ziaja, F. Tavella, and L. Giannessi. "Pulse Duration of Seeded Free-Electron Lasers". In: *Physical Review X* 7.2 (2017), p. 021043. DOI: 10.1103/physrevx.7.021043 (cit. on p. 84).

[259] L. Miaja-Avila, C. Lei, M. Aeschlimann, J. L. Gland, M. M. Murnane, H. C. Kapteyn, and G. Saathoff. "Laser-Assisted Photoelectric Effect from Surfaces". In: *Physical Review Letters* 97.11 (2006), p. 113604. DOI: 10.1103/physrevlett.97.113604 (cit. on p. 84).

[260] G. Saathoff, L. Miaja-Avila, M. Aeschlimann, M. M. Murnane, and H. C. Kapteyn. "Laser-assisted photoemission from surfaces". In: *Physical Review A* 77.2 (2008), p. 022903. DOI: 10.1103/physreva.77.022903 (cit. on p. 84).

[261] S. Hellmann, M. Beye, C. Sohrt, T. Rohwer, F. Sorgenfrei, H. Redlin, M. Kalläne, M. Marczynski-Bühlow, F. Hennies, M. Bauer, A. Föhlisch, L. Kipp, W. Wurth, and K. Rossnagel. "Ultrafast Melting of a Charge-Density Wave in the Mott Insulator $1T - TaS_2$". In: *Physical Review Letters* 105.18 (2010), p. 187401. DOI: 10.1103/physrevlett.105.187401 (cit. on pp. 85, 87).

[262] S. Doniach and M. Sunjic. "Many-electron singularity in X-ray photoemission and X-ray line spectra from metals". In: *Journal of Physics C: Solid State Physics* 3.2 (1970), pp. 285–291. DOI: 10.1088/0022-3719/3/2/010 (cit. on p. 87).

[263] L. Jönsson. "Energy shifts due to the ponderomotive potential". In: *J. Opt. Soc. Am. B* 4.9 (1987), pp. 1422–1425. DOI: 10.1364/JOSAB.4.001422 (cit. on p. 89).

[264] D. Fausti, R. I. Tobey, N. Dean, S. Kaiser, A. Dienst, M. C. Hoffmann, S. Pyon, T. Takayama, H. Takagi, and A. Cavalleri. "Light-Induced Superconductivity in a Stripe-Ordered Cuprate". In: *Science* 331.6014 (2011), pp. 189–191. DOI: 10.1126/science.1197294 (cit. on p. 97).

[265] S. Ulstrup, J. C. Johannsen, M. Grioni, and P. Hofmann. "Extracting the temperature of hot carriers in time- and angle-resolved photoemission". In: *Review of Scientific Instruments* 85.1 (2014), p. 013907. DOI: 10.1063/1.4863322 (cit. on p. 99).

List of publications

- **Denny Puntel**, Wibke Bronsch, Manuel Tuniz, Mingu Kang, Paul Neves, Shiang Fang, Efthimios Kaxiras, Joseph G. Checkelsky, Riccardo Comin, Fulvio Parmigiani, and Federico Cilento, *Photoinduced dynamics of flat bands in the kagome metal CoSn*, preprint at arXiv:2305.09531, submitted to PRB

- **Denny Puntel**, Dymytro Kutnyakhov, Markus Scholz, Lukas Wenthaus, Nils Wind, Michael Heber, Günter Brenner, Wibke Bronsch, Federico Cilento, Fulvio Parmigiani, and Federico Pressacco, *Out-of-equilibrium charge redistribution in Bi2212 by TR-XPS*, preprint at arXiv:2306.12905, submitted to Scientific Reports

- **Denny Puntel**, Jürgen Braun, Hubert Ebert, Simone Peli, Wibke Bronsch, Federico Cilento, and Fulvio Parmigiani, *Unveiling the Spin-Orbit Coupling Strength in a Model Topological Insulator from Theory and Experiments*, in preparation

- Manuel Tuniz, Davide Soranzio, Davide Bidoggia, **Denny Puntel**, Wibke Bronsch, Steven L. Johnson, Maria Peressi, Fulvio Parmigiani, Federico Cilento, *Ultrafast all-optical manipulation of the charge-density-wave in VTe_2*, preprint at arXiv:2305.03528 (2023), under review in PRL

- Manuel Tuniz, Armando Consiglio, **Denny Puntel**, Chiara Bigi, Stefan Enzner, Ganesh Pokharel, Pasquale Orgiani, Wibke Bronsch, Fulvio Parmigiani, Vincent Polewczyk, Phil D. C. King, Justin W. Wells, Ilija Zeljkovic, Pietro Carrara, Giorgio Rossi, Jun Fujii, Ivana Vobornik, Stephen D. Wilson, Ronny Thomale, Tim Wehling, Giorgio Sangiovanni, Giancarlo Panaccione, Federico Cilento, Domenico Di Sante, and Federico Mazzola, *Dynamics and Resilience of the Charge Density Wave in a bilayer kagome metal*, preprint at arXiv:2302.10699 (2023), submitted to Nature Communications

- Mingu Kang, Sunje Kim, Yuting Qian, Paul M. Neves, Denny Puntel, Federico Mazzola, Shiang Fang, Chris Jozwiak, Aaron Bostwick, Eli Rotenberg, Jun Fuji, Ivana Vobornik, Jae-Hoon Park, Joseph G. Checkelsky, Bohm-Jung Yang, and Riccardo Comin, *Measurement of the quantum geometric tensor in solids*, submitted to Science

- Paulina Ewa Majchrzak, Yuntian Liu, Klara Volckaert, Deepnarayan Biswas, Chakradhar Sahoo, **Denny Puntel**, Wibke Bronsch, Manuel Tuniz, Federico Cilento, Xing-

Chen Pan, Qihang Liu, Yong P. Chen, and Søren Ulstrup, *Van der Waals Engineering of Ultrafast Carrier Dynamics in Magnetic Heterostructures*, Nano Lett. 23(2), 414–421 (2023)

- Klara Volckaert, Byoung Ki Choi, Hyuk Jin Kim, Deepnarayan Biswas, **Denny Puntel**, Simone Peli, Fulvio Parmigiani, Federico Cilento, Young Jun Chang, and Søren Ulstrup, *External screening and lifetime of exciton population in single-layer $ReSe_2$ probed by time- and angle-resolved photoemission spectroscopy*, preprint at arXiv:2301.03916 (2023), Phys. Rev. Materials 7, L041001 (2023)

- Wibke Bronsch, Manuel Tuniz, Giuseppe Crupi, Michela De Col, **Denny Puntel**, Davide Soranzio, Alessandro Giammarino, Michele Perlangeli, Helmuth Berger, Dario De Angelis, Danny Fainozzi, Ettore Paltanin, Jacopo Stefano Pelli Cresi, Gabor Kurdi, Laura Foglia, Riccardo Mincigrucci, Fulvio Parmigiani, Filippo Bencivenga, and Federico Cilento, *Ultrafast dynamics in $(TaSe_4)_2 2I$ triggered by valence and core level excitation*, Faraday Discussions 237, 40-57 (2022)

- Simone Peli, **Denny Puntel**, Damir Kopic, Benjamin Sockol, Fulvio Parmigiani, and Federico Cilento, *Time-Resolved VUV ARPES at 10.8 eV photon energy and MHz repetition rate*, Journal of Electron Spectroscopy and Related Phenomena 243, 146978 (2020)

- Michele Perlangeli, Simone Peli, Davide Soranzio, **Denny Puntel**, Fulvio Parmigiani, and Federico Cilento, *Polarization-resolved broadband time-resolved optical spectroscopy for complex materials: application to the case of MoTe2 polytypes*, Optics Express 28, 8819 (2020)

Scientific contributions

- Talk, *Out-of-equilibrium charge redistribution in Bi2212 by TR-XPS*, New Generations In Strongly Correlated Electron Systems (04- 09/09/2022), Iseo (Italy)
- Poster, *Out-of-equilibrium charge redistribution in Bi2212 by TR-XPS*, Science@FELs (19-22/09/2022) Hamburg (Germany)
- Poster, *Photoinduced flat band dynamics in kagome metal CoSn by TR-ARPES*, Nonequilibrium Quantum Workshop (12-15/12/2022) Krvavec (Slovenia)
- Talk, *Out-of-equilibrium charge redistribution in Bi2212 by TR-XPS*, DESY User Meeting - Satellite Workshop "Momentum Microscopy at FLASH and PETRA III" (24/01/2023) Hamburg (Germany)
- Talk, *Photoinduced flat band dynamics in kagome metal CoSn by TR-ARPES*, DPG Spring Meeting of the Condensed Matter Section (26- 31/03/2023) Dresden (Germany)

Acknowledgements

First of all I want to thank the collaborators from outside the group of T-ReX that have contributed to the scientific projects herein.

Thanks to Dr. Jürgen Braun (LMU) for providing an astounding amount of *ab initio* calculations for the comparison between theory and experiment in the investigation of Bi_2Se_3, and for the fruitful discussions.

Thanks to Prof. Riccardo Comin and Mingu Kang (MIT) for starting our collaboration on CoSn. Thanks also to Paul Neves and Prof. Joseph Checkelsky for providing the samples and to Dr. Shiang Fang and Prof. Efthimios Kaxiras for the DFT calculations of the band structure.

Thanks to the SPRINT team, in particular Dr. Gianmarco Pierantozzi and Dr. Riccardo Cucini for providing the expertise and the source to perform the HHG measurements on Bi2212.

Thanks to all the participants to the beamtime on Bi2212 at FLASH and in particular Dr. Federico Pressacco, Dr. Dmytro Kutnyakhov, and Dr. Lukas Wenthaus for fruitful discussion after the experiment.

Ringraziamenti

Questa tesi arriva come la conclusione dei miei anni di dottorato e, con esso, dei miei nove anni tergestini. Se ne sia una conclusione degna, non so; che non ne sia un riassunto esaustivo, sono certo. Anche questi ringraziamenti non possono esaurire la quantità di umanità che mi è stata donata nelle forme più disparate (e inaspettate) in questi quasi quattro anni di dottorato. Eppure, non posso tacere alcuni grazie che, nel vedere quest'opera compiuta, chiedono di essere detti.

Il primo va al professor Parmigiani, per il suo instancabile esempio nel mostrare che davvero il fuoco sacro può plasmare una vita, e per saperlo accendere anche in chi, ancora, non ce l'ha.

A Federico, instancabile virtuoso della tecnica e della sopravvivenza nello strano mondo in cui abbiamo scelto di cacciarci. Grazie per aver avuto pazienza e, le giuste volte, tenacia.

A Giancarlo, per la pazienza e la garbata schiettezza.

Alla dottoressa, Wibke, per aver sempre ricominciato, per non stancarsi mai di cercare cosa c'è davvero dietro al nostro teatrino di marionette, e per mostrare costantemente che ogni granello di realtà è pieno di significato.

Al mitico dottorando *junior*, Manuel, che prima di esserlo era già più sgaio dei dottorandi veri. Per i consigli sempre acuti, per le battute taglienti, e per aver condiviso molto più del lavoro. A entrambi voi, per aver provato, impresa disperata, a insegnarmi a saper ridere di me.

A quelli che hanno avuto il *granulum salis* di fare una tesi da noi, per la fiducia e la condivisione schietta di questo tratto di cammino insieme.

A Bona, Ettore e gli Sprinters per la compagnia preziosa, specialmente in questi ultimi mesi di ascesi scientifica.

Agli amici e colleghi già dottorati o quasi: i due Simoni, LateX e Pippo, Vanni, Armi, Chiara, Giulia, Fede, Manf, Daniele, per aver condiviso anche questi anni un po' balordi.

A tutti i viaggiatori della leggendaria 51(/), conosciuti e non, metafora della vita dove, semplicemente, è più bello essere insieme. Per dirla con Caproni, *Con voi sono stato lieto, / dalla partenza, e molto / vi sono grato, credetemi, / per l'ottima compagnia.*

Al generalissimo generale Giacomo Frassino Jarc, soprattutto perché c'è; come nei mesi di isolamento insieme, anche in questi anni di alti e bassi, la compagnia che ci siamo fatti è stata un punto sempre positivo e indubitabile, capace da solo di salvare intere giornate storte. Per aver condiviso e ascoltato più *highlight* di chiunque altro, per aver sempre sopportato la mia pignoleria e i frequenti delirî melomaniaci, di cui fin l'apertura di questa tesi è testimone, per non arrabbiarsi mai, e per una quantità di cose che solo chi condivide ogni giorno di quattro anni (e cinquantotto giorni di reclusione) può accumulare. Tutte le cordialità generale.

A Pietro "sì, tu?" Gorlini (... poi ti spiego ...) e Nicola "oh vecio" Spiletti, per aver supplito a troppe nostre mancanze, ma soprattutto per aver sempre offerto una boccata di vita concreta e semplice anche alle nostre giornate più allucinate. E la sventurata (rispose) Marta, per i limoncelli e le birre al limitare della follia.

A Fra' Bozio del caro ordine dei Giulî, per le innumerevoli cene tirate su all'ultimo, per essersi sempre occupato e preoccupato, e mai spazientito dalla mia evasività scientifica. A Mitch, Dorifire, Giulietto ed Elena, al pari eterni baluardi della Pastorale.

All'insostituibile Scuola di Comunità di san Giacomo, dove la vita è più vita. A Rudy per la sua umanità ancora travolgente e sempre liberante, dopo anni di conoscenza. A Petrus per il suo sguardo sempre candido e stupito. A Pari, a Erika, alle due Dame di san Giacomo, Valentina e Samantha, al Domenico di tutte le fortune, per l'affetto insostituibile; e a tutti, uno per uno, per esserci oltre ogni dubbio.

A quelli che sono un po' o molto più lontano, ma mi sono in realtà sempre vicinissimi. A Margherita e Valerio per l'instancabile profondità, e per riuscire a vedere in me molto più addentro di quel che riesco a vedere io. Al dr. Truccolo, Agnul, Tommaso, Marco, Anna, Paolo, segno lampante e consolante di una confidenza che non si scalfisce nonostante tutto. Fra chescj, a Giulia e Simona grazie encje pas balades e pas babades, a Simone pa fiduce e pas sunades. A Colza per saperci essere sempre.

A none Enie, none bis, e zio Attilio.

A nonna Rosi e zia Tania per i caffè sempre rassicuranti nelle mie troppo rare visite. A mio fratello che la sa molto più lunga di me e che sa stemperare con una parola le fissazioni più incalcate. Infine, primo meraviglioso dono che mi è stato fatto in questo mondo, ai miei genitori, che sono e saranno sempre la prima radice della mia identità.